Perspective

Opportunities for gas-phase science at short-wavelength free-electron lasers with undulator-based polarization control

Markus Ilchen,[1,2,3,4,*] Enrico Allaria,[5] Primož Rebernik Ribič,[5] Heinz-Dieter Nuhn,[6] Alberto Lutman,[6] Evgeny Schneidmiller,[2] Markus Tischer,[2] Mikail Yurkov,[2] Marco Calvi,[7] Eduard Prat,[7] Sven Reiche,[7] Thomas Schmidt,[7] Gianluca Aldo Geloni,[4] Suren Karabekyan,[4] Jiawei Yan,[4] Svitozar Serkez,[4] Zhangfeng Gao,[8] Bangjie Deng,[9,10] Chao Feng,[8,10] Haixiao Deng,[8,10] Wolfram Helml,[11] Lars Funke,[11] Mats Larsson,[12] Vitali Zhaunerchyk,[13] Michael Meyer,[4] Tommaso Mazza,[4] Till Jahnke,[4,14] Reinhard Dörner,[15] Francesca Calegari,[1,3] Olga Smirnova,[16,17,18] Caterina Vozzi,[19] Giovanni De Ninno,[5,20] Jonas Wätzel,[21] Jamal Berakdar,[21] Sadia Bari,[2,22] Lucas Schwob,[2] Jérémy R. Rouxel,[23] Shaul Mukamel,[24] Klaus Bartschat,[25] Kathryn Hamilton,[26] Luca Argenti,[27] Nicolas Douguet,[27] Nikolay M. Novikovskiy,[28] Philipp V. Demekhin,[28] and Peter Walter[1,6,29,†]

[1]*Institut für Experimentalphysik, Universität Hamburg, Luruper Chaussee 149, 22761 Hamburg, Germany*
[2]*Deutsches Elektronen-Synchrotron DESY, Notkestrasse 85, 22607 Hamburg, Germany*
[3]*Center for Free-Electron Laser Science CFEL, Deutsches Elektronen-Synchrotron DESY, Notkestrasse 85, 22607 Hamburg, Germany*
[4]*European XFEL, Holzkoppel 4, 22869 Schenefeld, Germany*
[5]*Elettra Sincrotrone Trieste, Strada Statale 14 km 163.5, 34149 Trieste, Italy*
[6]*SLAC National Accelerator Laboratory, 2575 Sand Hill Road, Menlo Park, California 94025, USA*
[7]*Paul Scherrer Institut, Forschungsstrasse 111, 5232 Villigen PSI, Switzerland*
[8]*Shanghai Advanced Research Institute, Chinese Academy of Sciences, China*
[9]*School of Nuclear Science and Technology, Xi'an Jiaotong University, China*
[10]*Shanghai Institute of Applied Physics, Chinese Academy of Sciences, China*
[11]*Technical University of Dortmund, Maria-Goeppert-Mayer-Straße 2, 44227 Dortmund, Germany*
[12]*Stockholm University, AlbaNova University Center, 114 21 Stockholm, Sweden*
[13]*University of Gothenburg, 405 30 Gothenburg, Sweden*
[14]*Max-Planck-Institut für Kernphysik, 69117 Heidelberg, Germany*
[15]*Institut für Kernphysik, Goethe-Universität, Max-von-Laue-Straße 1, 60438 Frankfurt am Main, Germany*
[16]*Max-Born-Institut, Max-Born-Straße 2A, 12489, Germany*
[17]*Technische Universität Berlin, Straße des 17. Juni 135, 10623 Berlin, Germany*
[18]*Solid State Institute and Physics Department, Technion–Israel Institute of Technology, Haifa 3200003, Israel*
[19]*Istituto di Fotonica e Nanotecnologie–CNR, Piazza Leonardo da Vinci 32, 20133 Milano, Italy*
[20]*Laboratory of Quantum Optics, University of Nova Gorica, 5001 Nova Gorica, Slovenia*
[21]*Institute of Physics, Martin-Luther University Halle-Wittenberg, D-06099 Halle, Germany*
[22]*Zernike Institute for Advanced Materials, University of Groningen, Nijenborgh 4, 9747 AG Groningen, Netherlands*
[23]*Chemical Sciences and Engineering Division, Argonne National Laboratory, Lemont, Illinois 60439, USA*
[24]*Department of Chemistry and Department of Physics and Astronomy, University of California, Irvine, Irvine, California 92697, USA*
[25]*Department of Physics and Astronomy, Drake University, Des Moines, Iowa 50311, USA*
[26]*Department of Physics, University of Colorado Denver, Denver, Colorado 80204, USA*
[27]*Department of Physics & CREOL, University of Central Florida, Orlando, Florida 32816, USA*
[28]*Institut für Physik und CINSaT, Universität Kassel, Heinrich-Plett-Straße 40, 34132 Kassel, Germany*
[29]*TAU Systems, 201 W 5th Street, Austin, Texas 78701, USA*

(Received 4 June 2024; published 27 January 2025)

Free-electron lasers (FELs) are the world's most brilliant light sources with rapidly evolving technological capabilities in terms of ultrabright and ultrashort pulses over a large range of photon energies. Their revolutionary and innovative developments have opened new fields of science regarding nonlinear light-matter interaction, the investigation of ultrafast processes from specific observer sites, and approaches to imaging matter with atomic resolution. A core aspect of FEL science is the study of isolated and prototypical systems in the gas phase with the possibility of addressing well-defined electronic transitions or particular atomic sites in molecules. Notably for polarization-controlled short-wavelength FELs, the gas phase offers new avenues for investigations of nonlinear and ultrafast phenomena in spin-orientated systems, for decoding the function of the chiral building

*Contact author: markus.ilchen@desy.de
†Contact author: pwalter@slac.stanford.edu

blocks of life as well as steering reactions and particle emission dynamics in otherwise inaccessible ways. This roadmap comprises descriptions of technological capabilities of facilities worldwide, innovative diagnostics and instrumentation, as well as recent scientific highlights, novel methodology, and mathematical modeling. The experimental and theoretical landscape of using polarization controllable FELs for dichroic light-matter interaction in the gas phase will be discussed and comprehensively outlined to stimulate and strengthen global collaborative efforts of all disciplines.

DOI: 10.1103/PhysRevResearch.7.011001

I. INTRODUCTION

Free-electron lasers (FELs) with their ultrashort and ultraintense light pulses are covering a broad photon-energy range from the vacuum ultraviolet (VUV) to the x-ray regime. They have been offering and rapidly developing their unique technical capabilities with large applicability for practically all disciplines of science.

Demanding goals for studying individual atomic and molecular structures, complex systems, as well as ultrafast and nonlinear light-matter interaction have been identified and successfully pursued, with a variety of groundbreaking achievements in the hard and soft x-ray regime. As one of the core promises of FELs, their unique pulses allow for taking snapshots of noncrystallizable molecules and clusters via the technique of coherent diffraction imaging. This method allows to take such snapshots of a system before substantial deformation can destroy the contrast of the picture. In synergy to this application, FELs have been enabling access to selectively ionizing electrons up to binding energies of currently about 25 keV. They can hence individually target a large variety of elements at their core-shell electrons. Already in the soft x-ray regime, key constituents of life's building blocks, such as hydrogen, carbon, nitrogen, oxygen, phosphorous, and sulfur can be fully covered. With the uniquely short and bright FEL pulses, elements in complex systems can thus be interrogated in detail for their view on ultrafast phenomena [1–4], meanwhile with a temporal resolution down to currently hundreds of attoseconds [5–7]. In particular due to their high brilliance, FELs have furthermore been shown to be able to efficiently create and investigate ionic matter up to very high charge states [8–13], transient core excited states [14], and phenomena such as stimulated x-ray Raman scattering [15,16], therefore enabling new perspectives for nonlinear x-ray physics and its applications.

For a variety of complementary light sources, such as optical lasers, HHG sources, and synchrotrons, it has been demonstrated that circularly polarized photons add a unique tool for studying states and characteristics of matter that are otherwise inaccessible. A prominent example are magnetization studies due to the spin-sensitivity of circularly polarized light [17,18]. Here, the different response of a magnetic target to opposing light helicities, i.e., its dichroic behavior, provides otherwise elusive insights about the system. Dichroism studies in general are one particularly powerful method for studying chiral systems and molecular structures. They form all known life and have profound relevance for understanding the very fabric of our universe (see illustration in Fig. 1).

In contrast to the condensed phase, gas-phase studies offer access to isolated systems without their environmental interaction and can thus reduce the complexity of a variety of processes to a level where theoretical calculations become feasible and more robust. In fact, as a first step to get access to the complex characteristics of FEL pulses, the gas phase allows for their noninvasive metrology, thus enabling subsequent experiments to benefit from the precise knowledge about each individual pulse. Due to the rapid technological evolution of FELs, metrology of ultrashort pulses in the few femtosecond to attosecond regime, with unprecedented brilliance and versatility in terms of single- and multicolor pump-probe and pulse-shaping schemes can be more robustly harnessed in the gas phase.

Pioneering FEL projects such as FERMI in Italy, LCLS (II) in the USA, European XFEL and FLASH (1 and 2) in Germany, SwissFEL in Switzerland, and SHINE and SXFEL in China have recognized the high importance of undulator-based ultrashort, ultrabright, and fully polarization-controllable light pulses. They have initiated or even finalized the effort to providing the technological basis for a new chapter of polarization-dependent FEL-science. These novel approaches with polarization-controlled FEL pulses will originate new scientific endeavors in, e.g., physics, chemistry, and structural biology with broad applicability in the gas phase.

The temporal profile of the x-ray wave field generated by free-electron lasers is fundamentally different from that of optical lasers, largely due to the self-amplified spontaneous emission (SASE) process that governs most (nonseeded)

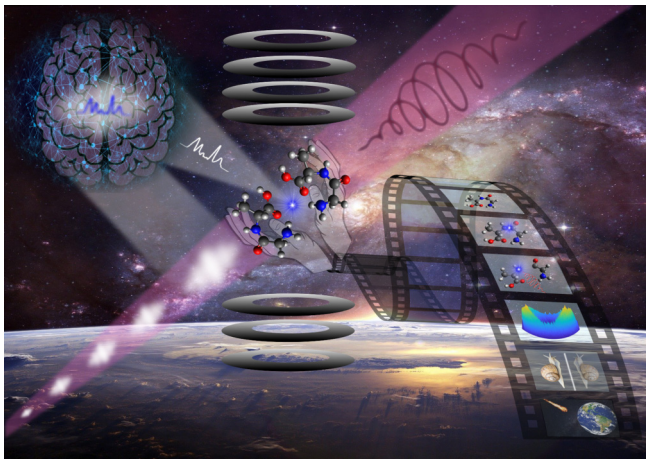

FIG. 1. Artistic illustration of chirality science with a SASE free-electron laser. AI-based analysis reveals the time-energy and polarization structure of every ultrashort pulse. The acquired in-depth knowledge allows for site-specific observations in chiral systems and molecules (here: Glycyl-l-alanine).

FELs. This process produces short pulses typically on the femtosecond to attosecond scale. Their temporal profile often consists of stochastic intensity spikes in time, which limits the overall coherence since the phase between the intrinsically coherent "spikes" is random and cannot be predicted. However, advancements such as external seeding techniques, which are employed at facilities like FERMI, enable the production of XUV and x-ray pulses with improved temporal and spatial coherence. Seeded FELs can generate wave fields that more closely resemble the coherent states produced by optical lasers, with enhanced control over the phase and amplitude of the wavefront. While complete temporal coherence, akin to continuous-wave optical lasers, remains a challenge due to the complex dynamics of electron beams and the nature of x-ray generation, ongoing innovations in electron beam quality and pulse shaping techniques are bringing FEL sources closer to this goal. Hence, while current FELs exhibit partial coherence far beyond other x-ray sources such as synchrotrons, future developments promise even greater control over the temporal characteristics of the x-ray wave field, enabling applications that demand higher degrees of coherence.

As FEL technology continues to evolve, several advancements are expected to enhance the available intensities and capabilities of facilities worldwide that currently reach up to about $10^{20}\,\mathrm{Wcm}^{-2}$. The development of new electron-beam manipulation and -compression techniques will allow for higher peak currents, thereby shortening pulse durations and boosting peak intensities. Advanced undulator designs, such as cryogenic and superconducting undulators, will increase the efficiency of x-ray generation, pushing both the peak and average intensities further. Additionally, high-repetition-rate operation, as available at the European XFEL and upcoming at facilities like LCLS-II and SHINE, will enable high intensities with up to MHz repetition rates, improving the average flux and opening up new experimental possibilities. Furthermore, new x-ray beam focusing methods, such as the use of diffractive optics or nanofocusing techniques, are being developed to focus beams at certain photon energy ranges to submicron spots, thus increasing the available fluence. Next-generation FELs are expected to offer both unprecedentedly high intensities and ultrashort pulses in the attosecond regime with full polarization control, which will push the boundaries of nonlinear x-ray science and allow researchers to explore previously inaccessible regimes.

The required undulators for generating the high-intensity pulses at FELs are much longer compared to the systems commonly employed at storage rings since the microbunching and the saturation of the subsequent lasing process requires longer time to evolve (more details are given in the machine-operation sections). The undulator sections at FELs can exceed 100 m in length and are the key to the exponential gain of the pulses' exceptional intensity and their ultrashort duration. This is distinctly different for FELs in comparison to storage-ring-based light sources and sometimes this exponential gain is referred to as fourth-generation of light generation whereas synchrotron undulators can be referred to as third generation. In fact, undulators do not only play a key role in the FEL pulse generation but also for shaping the polarization properties of the x-ray beam at FELs, in particular for generating high-intensity pulses. Standard planar undulators generate linearly polarized radiation, with the electric field oscillating in a single plane. However, to achieve polarization control, more advanced undulator designs are required. The advanced planar polarized light emitter (APPLE) undulator is a widely used device that enables variable polarization states, including linear, circular, and elliptical polarization, by shifting segments of permanent magnets to modify the magnetic field orientation [19]. Recent developments, such as APPLE-III and APPLE-X undulators, provide enhanced polarization control, allowing for faster switching between polarization states and improved radiation performance, making them suitable for high-demand experiments involving magnetic or chiral properties [20–25].

The DELTA undulator, set to be installed at LCLS [26,27], features a compact, helical design that allows for precise control over the polarization state in "afterburner" configuration, including the generation of circular polarization. The upcoming DELTA II undulator at LCLS-II will build on this capability with improved magnetic field configurations, offering a broader tuning range for photon energies while maintaining high polarization purity. Once operational, these undulators will enable cutting-edge experiments on phenomena such as magnetic circular dichroism and ultrafast chiral dynamics, significantly enhancing the capabilities of FEL-based research at these facilities.

In the following, we will sketch the technological landscape of free-electron laser facilities worldwide and their capabilities for undulator-based polarization control. Based on this technological background, we will give a comprehensive overview over photon-based diagnostic strategies and instrumentation opportunities as well as current and future perspectives for experimenting with undulator-based polarization-controlled FEL pulses. Subsequently, we will sketch the scientific milestones and visions of gas-phase science with such pulses, and the imminent and long-term prospects of the emerging technological era from the perspective of experiment and theory.

II. MACHINE OPERATION—FACILITIES WORLDWIDE

A. FERMI@Elettra, Italy

Enrico Allaria and Primož Rebernik Ribič.

1. Layout of the FERMI facility

The electron beam produced by the FERMI linear accelerator can be used to emit light in two FEL lines: FEL-1 and FEL-2; see Fig. 2. Both use APPLE-2 undulators [28–30], allowing to tune the wavelength and the polarization of the emitted radiation.

With an electron-beam energy ranging from 0.9 to 1.5 GeV, the two FEL lines cover the full spectral range from 100 nm down to 4 nm [31]. FEL-1 [32] is designed to emit at long wavelengths (∼100–20 nm) and relies on a single-stage high-gain harmonic-generation scheme (HGHG) [33]. One planar undulator is used to facilitate the interaction between the electron beam and an external coherent laser, whose wavelength is set according to the required FEL output. FEL radiation with tunable polarization is produced in the long radiator composed of 6 APPLE-2 undulators (see Table I).

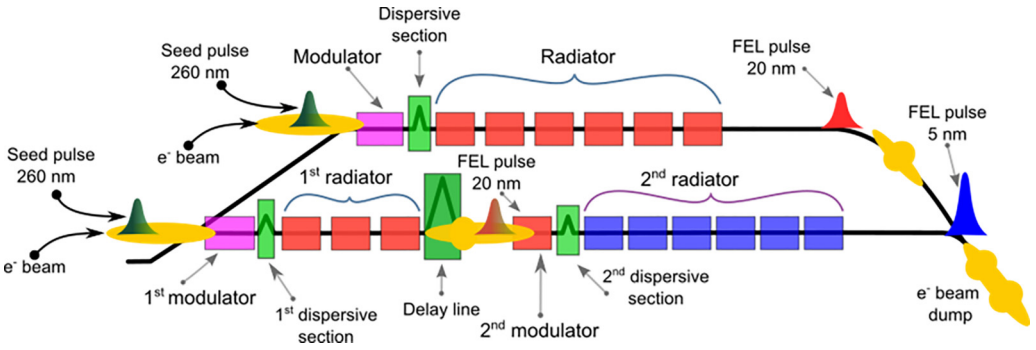

FIG. 2. Layout of the FERMI FELs. FEL-1 (top) uses a single HGHG stage with one modulator and 6 radiators. FEL-2 (bottom) relies on two stages to reach shorter wavelengths.

The FEL-2 layout was optimized to allow generation of highly coherent pulses with wavelengths down to 4 nm [34]. The nominal operation mode is based on a two stage HGHG scheme. Running FEL-2 using a more efficient seeding scheme called echo-enabled harmonic generation (EEHG) was demonstrated with minimal changes to the layout [35]. Operating FEL-2 in the SASE mode, characterized by a large bandwidth and partial coherence, is also possible and done when requested by users [36]. Two undulator sets are available at FEL-2. During normal operations, the first set (with the same parameters as the FEL-1 radiator) generates an FEL pulse with an intermediate wavelength (60–20 nm), which then seeds the second stage. The second stage radiator uses undulators with a smaller period (see Table I) to reach shorter FEL wavelengths with the same electron beam energy. Both stages have the possibility of controlling the polarization state of the emitted radiation. The FERMI FEL takes full advantage of external seeding that allows producing powerful (GW level), short (<100 fs) pulses with a narrow relative bandwidth ($\sim 10^{-4}$) and a high degree of coherence (more details on photon properties are available in Ref. [31] and at FERMI). The two FELs cannot be operated simultaneously and time is shared between users that require long or short wavelengths.

2. Polarization control

The use of APPLE-2 undulators for all FERMI radiators allows full control of the output polarization of the final FEL pulse [37]. For experiments not requiring a specific polarization state, circular polarization is usually chosen to take advantage of the stronger FEL amplification [38], allowing typically to increase the energy per pulse by a factor of 2 or more with respect to linear polarization.

Both FEL-1 and FEL-2 lines are mostly operated in linear horizontal (LH) or circular clockwise (C+) polarizations (about 45% of uptime for each configuration). Circular anticlockwise (C−) and linear vertical (LV) polarizations are chosen only when explicitly required by the user (higher transmission and/or dichroic experiments) and account for about 5% (each) of the total uptime. As a result of different magnet configurations, undulators have a different maximum (normalized) undulator parameter aw0 for each polarization (see Table I), with a lower value for LV polarization. Adjustments of the electron beam energy are necessary if a broad tuning range is required, especially when the FEL is operated in vertical polarization.

At ∼GeV electron beam energies used at FERMI, changes of the undulator gap (to adjust the wavelength) and phase (to set the polarization) can have a significant effect on the electron beam focusing. These effects need to be properly compensated for by adjusting the strength of the focusing and defocusing quadrupoles placed between undulators. Both circular polarizations have the same undulator focusing, allowing very fast switching between the two orthogonal polarization states. Typical circular dichroic experiments are performed by switching the polarization every 5–10 min and the change of the polarization state takes only a few tens of seconds. Due to the required changes of the electron-beam optics, the switching from LH to LV or from LH to circular polarization takes a few minutes.

TABLE I. Parameters of the FERMI radiators.

FEL parameter	FEL-1	FEL-2
Period (mm)	55	35
Number of periods	42	66
Undulator length (m)	2.31	2.31
Number of undulators	6	6
Minimum gap (mm)	10.5	10.5
Maximum aw0 (LH)	5.3	2.4
Maximum aw0 (LV)	4.3	1.7
Maximum aw0 (CR, CL)	5.0	2.0

3. Advanced polarization schemes

a. Crossed-polarized undulator scheme. The possibility to set the polarization of each undulator separately makes FERMI an ideal layout for advanced polarization schemes. One interesting method relies on the superposition of two orthogonally polarized fields with a controlled relative phase [39,40]. The scheme, originally proposed for synchrotrons, benefits from the higher degree of coherence of FELs and has been demonstrated both at FEL-1 and FEL-2 [41,42]. The possibility to control the polarization state by adjusting only a phase shifter (small magnetic chicane) can be exploited in measurements with continuous or high frequency polarization switching; with the current setup, adjustments of the phase shifter can be done within seconds and with minimal impact

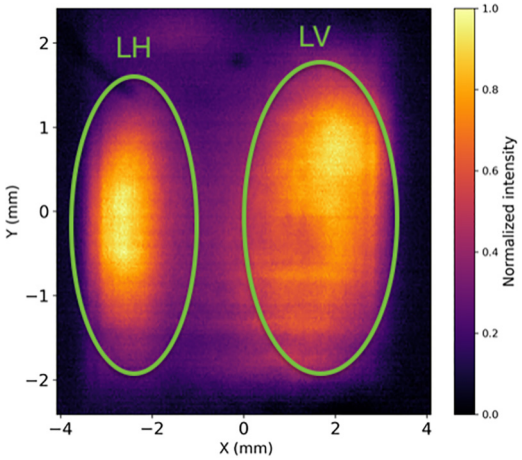

FIG. 3. Spatial profile of the two pulses produced by the cross-polarized undulator scheme with a kick in the electron-beam trajectory. Data refer to FERMI FEL-1 operated at 20.8 nm (manuscript in preparation).

on the electron beam dynamic. The cross-polarized undulator scheme enables, e.g., a continuous rotation of the direction of linear polarization [41] and rapid switching between LH and LV states. A much higher frequency of the polarization switching would be possible using an electromagnetic phase shifter that could potentially change the polarization of each FEL shot (50 Hz).

b. Femtosecond polarization shaping of FEL pulses. Recently, a method to produce FEL pulses with time-dependent polarization has been proposed [43,44]. During a recent experiment at FERMI, it was demonstrated that such pulses can indeed be generated using an FEL (manuscript under review). At the FEL-1 as well as the FEL-2 line, we produced two subpulses with orthogonal polarizations (i.e., C+ and C−) and tunable time delay, which was controlled with either a magnetic chicane or a few undulators tuned to a long wavelength (and not to a harmonic of the seed laser). Such a configuration generates an FEL pulse whose polarization varies from C+ to linear (whose direction can be controlled by varying the phase between the subpulses as in the cross-polarized undulator scheme; see above) and then to C− on a timescale of tens of fs. Our preliminary results suggest that it might be possible to extend the applications of such polarization-shaped pulses, originally developed for the visible spectral region (see, e.g., Ref. [45]), into the extreme-ultraviolet regime.

c. Low harmonic emission. FELs with planar or APPLE-2 undulators tuned to linear polarization are known to produce nonnegligible on-axis radiation at odd harmonics, with a power typically on the order of a few 10^{-3} of the fundamental emission. This harmonic emission can be used to extend the tuning range of FERMI [46] but may also be unwanted in some experiments. A low on-axis content of harmonic emission is easily achieved when the undulators are tuned to circular polarization due to the off-axis character of harmonics [47]. The use of circularly polarized undulators in the cross-polarized configuration was shown to be the optimal solution for having a low on-axis harmonic content while producing linearly polarized FEL light.

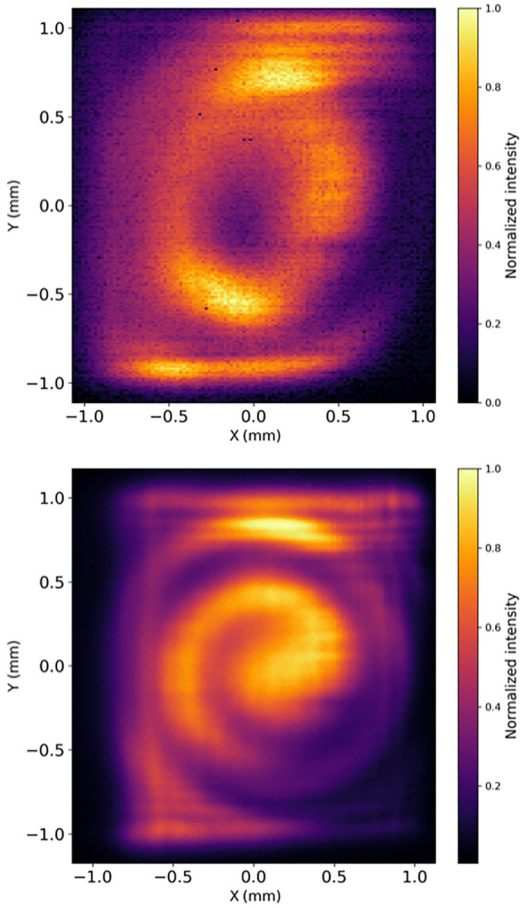

FIG. 4. FEL intensity distribution corresponding to an OAM optical mode from second harmonic emission (top) and the characteristic spiral interference pattern between the second harmonic OAM mode and the fundamental on-axis emission (bottom).

d. Different pointing. The cross-polarized undulator scheme in combination with a controlled tilt of the electron-beam trajectory through the radiator [48] is used to produce two orthogonally polarized FEL pulses with different pointing. The two FEL pulses, which are spatially completely separated in the downstream optics (Fig. 3), can be used for FEL pump—FEL probe experiments with orthogonal polarizations.

e. Orbital angular momentum. Besides having full control over the polarization state or equivalently the spin angular momentum of emitted photons, FERMI also allows generating light that carries orbital angular momentum (OAM) [49]. These so-called optical vortex beams are characterized by a doughnut-shaped intensity profile and a helical phase dependence; see Fig. 4. Two approaches are used to generate OAM at FERMI [50]: (i) vortex beams with a topological charge of $l = 1/-1$ are naturally generated at the second harmonic when the FERMI radiator is set to CR/CL polarization (Fig. 4) and (ii) high-intensity vortex beams with tunable (and independent of polarization) topological charge can be generated at the fundamental wavelength by inserting a spiral zone plate into the beam downstream of the radiator. The latter approach is now routinely used in experiments at FERMI; see Sec. III G for details.

B. LCLS@SLAC, USA

Heinz-Dieter Nuhn and Alberto Lutman.

The LCLS facility has been in operation to produce x-ray free-electron pulses from 2009 [51] producing x-rays for scientific applications between 270 eV and 12.8 keV. The original layout included a normal conducting (NC) linac, accelerating electron bunches up to 17 GeV, with a repetition rate up to 120 Hz. Horizontally polarized x-rays were produced in an undulator line equipped with fixed gap undulators. An adjustment of K for each undulator segment was allowed, within a small range, by the canted pole design. Operating the NC Linac in nominal conditions, a 250 pC electron bunch is extracted at the cathode, in a first bunch compressor, the bunch charge is reduced to 180 pC [52] and the bunch is compressed to a current of about $\approx$ 220 A. A second bunch compressor, operating either at 3 or 5 GeV compresses the bunch to the final current of few kA, with a typical bunch duration of 35 fs. Several schemes have been introduced to further control the pulse duration: reducing the bunch charge, using a slotted foil emittance spoiler [53,54], and fresh-slice schemes [55–58] can reach few femtoseconds duration, while non linear compression and eSASE were able to reach the hundreds of attosecond regime [5,59].

1. Polarization control

A variable polarization DELTA Undulator [27] was installed as afterburner as last segment of the original LCLS undulator line. The DELTA design presented four parallel longitudinal rows of $Nd_2Fe_{14}B$ magnetic blocks, effectively forming two crossed planar undulators. The polarization was controlled by adjusting the relative longitudinal position of the rows. The mechanical movement required for a full switch of left circular to right circular polarization, can be accomplished in about half a minute. To produce FEL radiation, the electron bunch needs to be microbunched, at the wavelength of interest, in the upstream segments. The number of upstream segments used is chosen to maximize the microbunching and the output of polarized controllable x-rays emitted by the electrons in the DELTA afterburner.

a. Beam diverting. The upstream undulator segments used to microbunch the electron beam produce linearly polarized x-rays. The overlap between these unwanted x-rays and the ones produced by the DELTA afterburner compromise the polarization purity of the delivered x-rays. Such x-ray pulses present also a variable and stochastic polarization along the beam, due to the slippage between upstream produced x-rays and the microbunched beam. To improve the polarization purity, the power ratio between the x-rays produced by the afterburner and the ones produced by the upstream undulator segments needs to be maximized. A typical ratio of 5 was achieved using a regular taper configuration. With reverse taper [60], the ratio was experimentally increased to $\approx$15. To further increase it, the beam diverting configuration has been developed [55], where the combined effect of a dipole kicker and of a defocusing quadrupole, located between the last linearly polarized segment and the DELTA afterburner, allows to produce the polarized x-ray at an angle with respect to the upstream linearly polarized x-rays. Spatial separation allowed collimating out the unwanted x-rays, increasing the desired power ratio to a factor exceeding 200, and yielding a degree of circularly polarized x-rays close to 100%, in pulses of about 10 GW of power. Further studies on the physics of microbunching rotation [61], enabling the beam diverting scheme, could further improve its performance and ease the setup of the configuration.

TABLE II. Parameters of the new LCLS-II facility at SLAC.

Undulator line	HXR		SXR	
Segment type	HXU		SXU	
Undulator period, λ_u (mm)	26		39	
Undulator minimum gap (mm)	7.2		7.2	
Number of segments	32		21	
Segment length (m)	3.4		3.4	
Periods per segment	130		87	
Direction of linear polarization	vertical		horizontal	
Electron source	NC	SC	NC	SC
Max electron energy (GeV)	15	4.0	8.0	4.0
Max repetition rate (Hz)	120	929 000	120	929 000
Max beam power (kW)	0.45	120	0.24	120
Min photon energy (keV)	1.0	1.0	0.2	0.2
Max photon energy (keV)	25	5.0	5.0	1.5

b. Two-color two-polarization. Split undulator schemes [62], particularly when combined with the fresh-slice technique [55], have proven capable of producing pairs of high power x-ray pulses, where the relative delay can be controlled up to 1 ps, and allowing to scan the delay across time coincidence. Since each x-ray pulse is produced in a different undulator section, properties as wavelength, polarization and pointing can be independently controlled. At the LCLS, a pair of pulses with energy separation of 15 eV, one linearly polarized and one circularly polarized have been produced and characterized in spectrum and polarization with a time of flight (TOF) polarimeter [63] (also see Sec. III A).

2. LCLS-II—Upgrading the LCLS FEL facility

The SLAC National Accelerator Laboratory (SLAC) is currently commissioning the upgrade project LCLS-II, which has replaced the original LCLS undulator line with two new

TABLE III. Parameters of the future LCLS-II-HE facility at SLAC.

Undulator line	HXR		SXR	
Segment type	HXU		HE-SXU	
Undulator period, λ_u (mm)	26		56	
Undulator minimum gap (mm)	7.2		7.2	
Number of segments	32		30	
Segment length (m)	3.4		3.4	
Periods per segment	130		60	
Direction of linear polarization	vertical		horizontal	
Electron source	NC	SC	NC	SC
Max electron energy (GeV)	15	8.0	10.0	8.0
Max repetition rate (Hz)	120	929 000	120	929 000
Max beam power (kW)	0.45	120	0.24	120
Min photon energy (keV)	1.0	1.0	0.2	0.2
Max photon energy (keV)	25	15.0	5.0	5.0

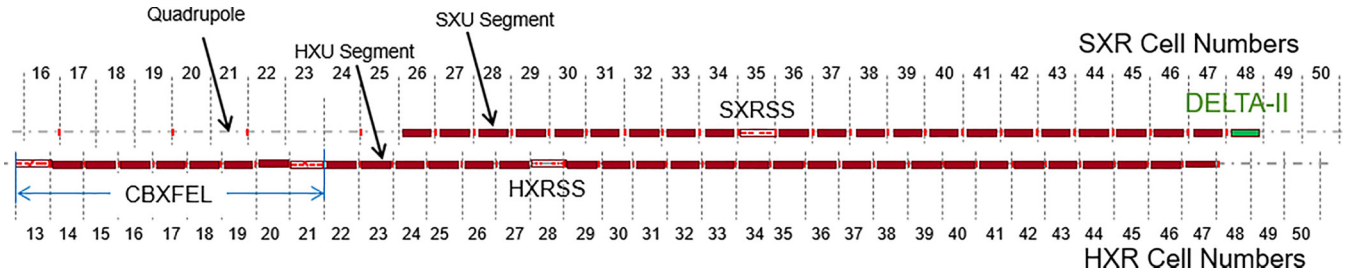

FIG. 5. LCLS-II main undulator line components layout with the first DELTA-II magnet location indicated in SXR cell 48.

undulator lines for providing hard x-ray (HXR) and soft x-ray (SXR) pulses, respectively, and added a new source of electrons, based on a new superconduction (SC) linac, in addition to the NC linac (the last third of the original SLAC linac), which was already used for the originally LCLS facility. Table II provides a parameter overview for the new facility.

While the LCLS-II project is being completed, another upgrade project, LCLS-II-HE, is already underway, which will raise the electron beam energy, that is delivered by the superconducting linac, from 4 to 8 GeV, add 9 undulator segments to the SXR line and increase the undulator period of the SXR line undulator segments from $\lambda_{u,SXU} = 39$ mm to $\lambda_{u,HE-SXU} = 56$ mm. Operations parameters for the upgraded undulator lines with the LCLS-II-HE linac are summarized in Table III.

In addition to the operation with the SC linac, operation with the NC linac will continue to be provided for both beamlines.

In parallel to upgrading the LCLS facility, SLAC is also developing a new, compact variable gap polarization control undulator, which is called DELTA-II [64]. Its performance is expected to be comparable to that of the DELTA undulator that was successfully operated with the original LCLS undulator system [18,27,48,65]. The development of this new polarizing undulator started in 2015 and it is scheduled to be available to operation in 2024. The DELTA-II magnet arrangement is similar to that of the APPLE X undulators [24] recently developed at PSI and, at closed gap, it is similar to the DELTA undulator. Table IV contains a summary of the DELTA-II parameters.

The DELTA-II undulator will be operated at the downstream end of the SXR line (SXR line cell 48, see Fig. 5) in afterburner mode, i.e., it will operate on an electron beam that has been microbunched by a moderate number (≈ 6) of regular SXR undulator segments. The change from the DELTA undulator to the DELTA-II undulator is necessary because of the change of the microbunching undulators from the original shorter-(30 mm)-period fixed gap LCLS-type undulator segments to the new longer-(39 mm)-period, variable gap LCLS-II SXR type undulator segments. The 39 mm period length of the SXR undulator segments (SXUs) had been chosen to optimized the SXR line performance for operating at the highest electron energy (4 GeV) of the LCLS-II superconducting linac. As mentioned above, the LCLS-II-HE project will increase the highest electron energy to 8 GeV. This requires to increase the period length of the SXR undulator segments to 56 mm (HE-SXUs). The period length of the DELTA-II undulator has been chosen to work with both period lengths. After the DELTA-II undulator has been developed and is operational, SLAC will try to secure funding for two additional DELTA-II undulators to be installed right after the first DELTA-II undulator in SXR line cells 49 an 50 (see Fig. 6).

TABLE IV. Parameters of the DELTA-II operating in afterburner mode with the LCLS-II and LCLS-II-HE beamlines.

Parameter	DELTA-II			
Undulator period, λ_u (mm)	49.333			
Maximum gap (mm)	22.6			
Minimum gap (mm)	6.6			
Maximum $K_{DELTA-II,linear}$	6.718			
Minimum $K_{DELTA-II,linear}$	1.727			
Segment core length (m)	3.26			
Core Periods per segment	66			
Polarization	various			
Undulator line	LCLS-II		LCLS-II-HE	
Electron source	NC	SC	NC	SC
Minimum electron energy (GeV)	3.7	3.7	4.9	4.9
Maximum electron energy (GeV)	8.0	4.0	8.0	8.0
$\lambda_{u,SXU/SXU-HE}$ (mm)	39	39	56	56
Maximum used $K_{SXU/SXU-HE}$	5.560	5.560	6.287	6.287
Minimum used $K_{SXU/SXU-HE}$	2.075	2.075	1.546	1.546
Minimum used $K_{DELTA-II,linear}$	1.727	1.727	1.727	1.727
Maximum used $K_{DELTA-II,linear}$	4.901	4.901	6.718	6.718
Minimum photon energy (eV)	0.200	0.200	0.200	0.200
Maximum photon energy (eV)	4.945	1.500	4.945	4.945

C. FLASH@DESY, Germany

Evgeny Schneidmiller, Markus Tischer, and Mikail Yurkov.

In the first XUV and soft x-ray FEL user facility FLASH [66,67], located at the Deutsches Elektronen-Synchrotron in Hamburg, the electron bunches with maximum energy of 1.25 GeV are distributed between the two undulator lines, FLASH1 and FLASH2 (see Fig. 7). The facility operates in the wavelength range 4–60 nm with long pulse trains (several hundred pulses) following with 10 Hz repetition rate. After the current upgrade, the electron energy will reach 1.35 GeV. A part of the upgrade is the installaton of a helical afterburner at FLASH2. Below we briefly describe the afterburner as well as a method to obtain high purity of circularly polarized radiation.

The helical afterburner at FLASH2 will be an APPLE-III undulator [23] which is presently developed and constructed

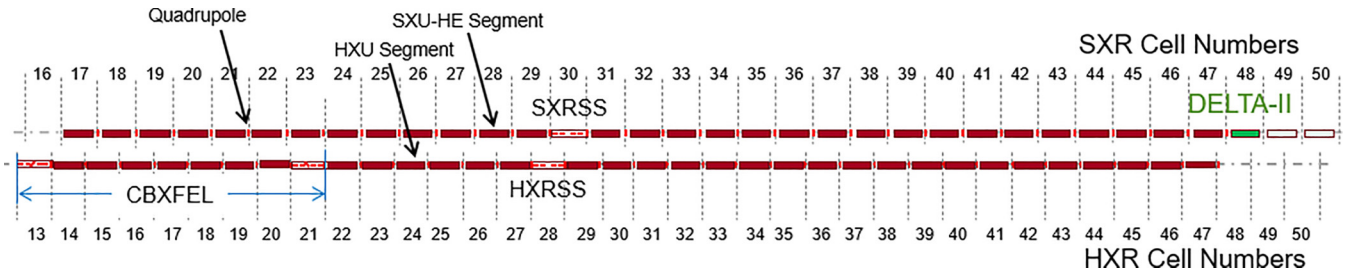

FIG. 6. LCLS-II-HE main undulator line components layout with the DELTA-II magnets indicated in SXR cells 48–50.

at DESY. The APPLE-III configuration will be a very efficient magnetic concept for circular beam apertures and well suited to reach the L-edges of the 3d transition metals Fe, Co, Ni despite the only moderate beam energy of 1.35 GeV. Although proposed for already many years, an APPLE-III undulator has not been realized up to now. Like in the well-known APPLE-II device, the pure permanent-magnet arrays are split longitudinally to create an elliptical magnetic field depending on the relative shift to each other. However, the vertically magnetized magnets of this Halbach structure are tilted by 45° pointing directly toward the beam. We combine this idea with a force compensation scheme to get a compact magnet structure which can be used together with gap mechanics like the already existing at FLASH2. This also allows for full opening of the gap which will result in a better radiation protection during machine commissioning.

The APPLE-III magnet structure will have a period length of 17.5 mm with a minimum magnet gap of 8 mm providing a maximum K-value of 0.92. At closed gap, the circular vacuum chamber (7 mm outer diameter) is mostly surrounded by the magnets leaving a small slit at the sides for its support. The total length will be 2.5 m. A short test structure had been built initially to investigate the force compensation scheme, mechanical performance, the tuning concept, and had also been characterized magnetically. Due the small size and period length, glued pairs of magnets corresponding to half a period will be used which simplifies the keeper design significantly. Meanwhile all parts of the magnet structure are in the fabrication process.

A method for suppression of the linearly polarized background from the main undulator was proposed in Ref. [60]: an application of the reverse undulator taper. It was shown that in some range of the taper strength the bunching factor at saturation is practically the same as in the reference case of the nontapered undulator, the saturation length increases moderately while the saturation power is suppressed by orders of magnitude. Therefore, the proposed scheme is conceptually very simple: in a tapered main (planar) undulator the saturation is achieved with a strong microbunching and a suppressed radiation power, then the modulated beam radiates at full power in a helical afterburner, tuned to the resonance. This method (in combination with the spatial separation) was used at LCLS to obtain a high degree of circular polarization [27,65] and is routinely used now in user operation. Obviously, the afterburner (helical or planar) can be tuned to a harmonic of the main undulator. In this case, the harmonics can be efficiently generated with a low background at the fundamental.

The reverse tapering concept was successfully tested at FLASH. The gap-tunable undulator of FLASH2 consists of 12 2.5 m long sections with the undulator period of 3.14 cm and the maximum root-mean-square (rms) K value about 1.9.

In the experiment in 2016 [68], we used the first ten undulator sections as a main undulator with reverse tapering, and the last two sections played the role of the afterburner, i.e., they could be tuned to a resonance with the incoming microbunched beam. The electron energy during the measurements was 715 MeV, and the FEL wavelength was 17 nm. We did a K-scan of the afterburner, showing the resonance, and also measured the FEL gain curve in this configuration, as shown in Fig. 8. One can see again that the high contrast (in excess of 200) between the radiation intensity from the afterburner and from the reverse-tapered undulator is measured.

We also demonstrated an efficient generation of the 2nd and the 3rd harmonics in the afterburner [68]. The electron energy was 852 MeV, and the wavelength for the untapered case was set to 25.5 nm. with the rms K parameter of 1.9. The first nine undulator sections were reverse-tapered, and the

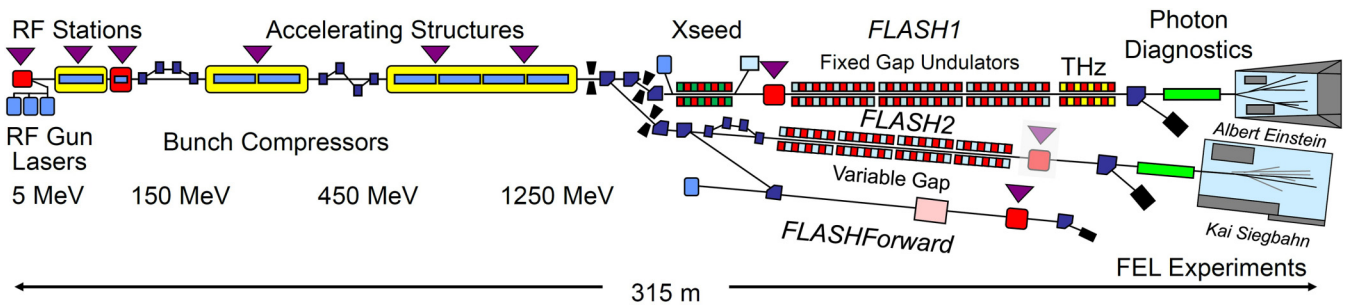

FIG. 7. Layout of the FLASH facility.

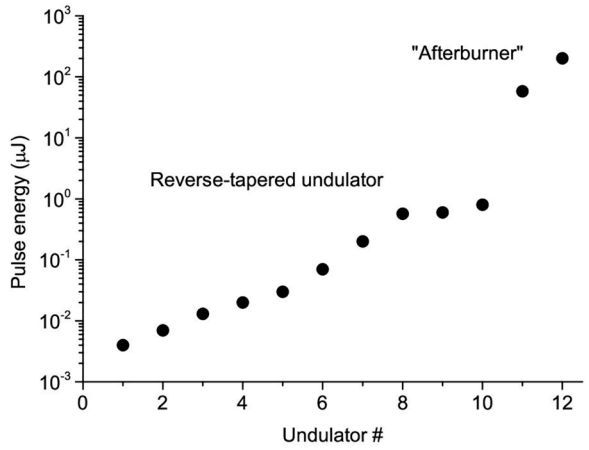

FIG. 8. FEL pulse energy versus undulator number. First ten undulators are reverse-tapered, and last two sections are tuned to the resonance with the incoming microbunched beam.

following two sections played the role of the afterburner. When the afterburner sections were completely opened, the background from the reverse-tapered main undulator was measured at the level of 0.9 μJ. When we tuned the afterburner sections to 26.2 nm, the pulse energy was 132 μJ, i.e., the contrast above 100 was measured. Then we tuned the afterburner to the second and the third harmonics of the main undulator and did the wavelength scan (or, K-scan) of the undulator around the corresponding resonances. The pulse energy reached 41 μJ when the afterburner was tuned to 13.2 nm, and 10 μJ for the 8.8 nm tune. Thus, we have demonstrated that the reverse tapering in the main undulator can be used for an efficient, background-free generation of harmonics in the afterburner.

This method will be used for production of high purity circular polarization at FLASH as soon as the APLLE-III afterburner will be installed, as anticipated to be done in mid 2023. To further improve the purity, we also consider using the beam diverting technique in the same way as it was done at LCLS [27].

D. SwissFEL@PSI, Switzerland

Marco Calvi, Thomas Schmidt, Sven Reiche, and Eduard Prat.

The FEL presently in user operation at the Paul Scherrer Institute in Switzerland, SwissFEL, is dedicated both to hard x ray and soft x ray. The layout of the facility is shown

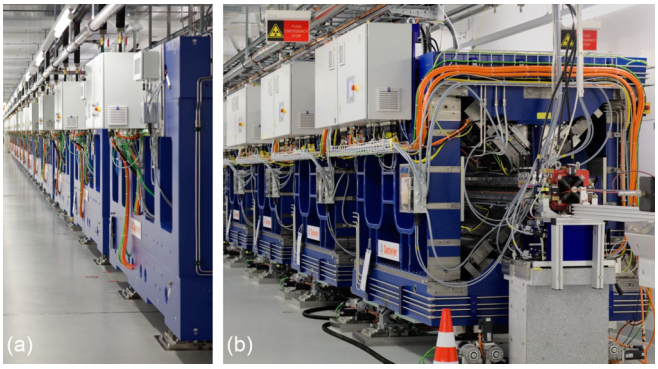

FIG. 10. On the left (a), the hard x-ray beamline of SwissFEL, Aramis, with its 13 in-vacuum permanent magnet undulators; on the right (b), the soft x-ray beamline Athos with its 16 Apple X undulators (in the picture only the last four are visible).

in Fig. 9 where the injector, the three linacs and the two stages of compression are schematically presented together with two beamlines. The first beamline commissioned in 2017 was Aramis [Fig. 10(a)], the SwissFEL hard x-ray branch, equipped with 13 planar in-vacuum undulators, each 4 m long and with a period length of 15 mm. With an electron beam energy up to 6.0 GeV, Aramis delivers photon pulses from 0.7 nm down to 0.08 nm in linear horizontal polarization. A second hard x-ray line called Porthos is planned for 2028 were a variable control of the polarization will be possible either with in-vacuum cryogenics APPLE devices [25] or with SCAPE [69], based on superconducting coils made of NbTi. The soft x-ray beamline is called Athos [Fig. 10(b)] and operates between 7 and 0.7 nm with Apple X undulators [24] (Fig. 11) to deliver polarized photon both in elliptical and linear polarization with arbitrary angle. Within a percentage changes (due to the residual susceptibility of the permanent magnets, geometrical tolerance of the frame and the variation of the forces) the deflection parameter, K, does not vary in an Apple X while operated in elliptical mode, which allows to reach the same photon energies both in LV and LH and in C+ and C−. The other advantage of the Apple X is the larger degrees of freedom with respect to the previous APPLE devices, which allow to move radially and independently the four magnetic rows. This enables to generate transverse gradients (TGs) in a controlled way and in any polarization while in an APPLE with four independently longitudinally movable rows it is only possible for elliptical and the relation between K and $\partial K/\partial x(y)$ is fixed [20].

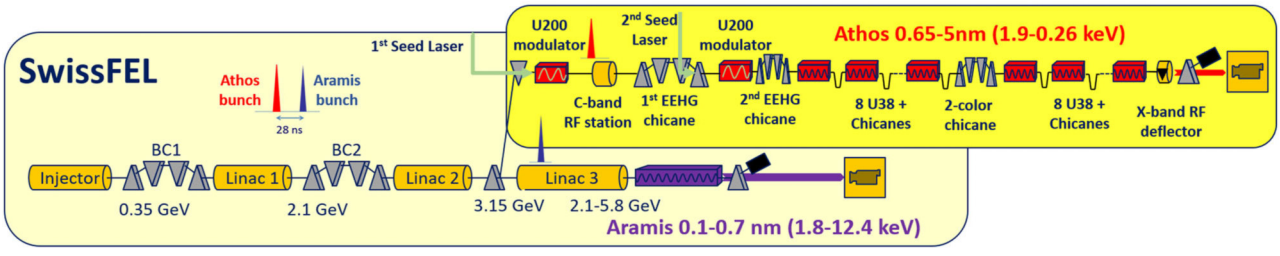

FIG. 9. SwissFEL layout, where the injector and the three linacs are schematically represented together with the details of the two beamlines, Aramis and Athos.

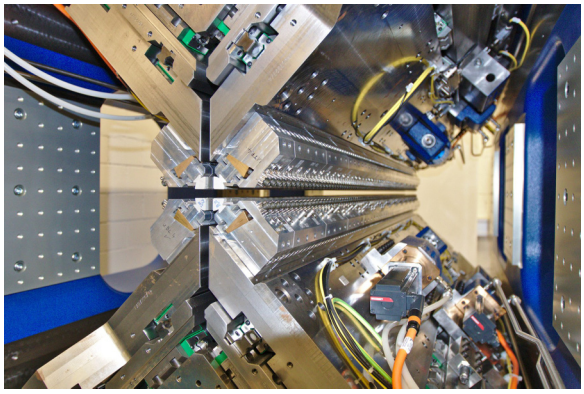

FIG. 11. The magnetic structure of an Apple X undulator. The four Halbach rows are visible as well as the stages and motors used both for their radial and longitudinal displacement, to tune the strength and the polarization respectively.

TGs can be used to control the FEL bandwidth [70] and to increase it above 10%. This has straight forward applications for instance in absorption spectroscopy which could be executed in single-shot mode, without the need of scanning the K. TGs could be used as well to minimize the impact of the slice energy spread if properly associated with the required dispersion as proposed in Ref. [71] for storage ring FEL oscillators. The Athos beamline was designed with compact chicanes (later on referred as CHICs) in between each 2 m long Apple X module. This length was the result of the optimization of this novel layout based on the compact chicanes as presented in Ref. [72]. With the help of the CHICs, a series of new operation modes is possible: starting from the optical Klystron which makes the saturation length shorter [73] and pave the way for more compact FEL sources; the high brightness SASE which reduces the bandwidth (enhancing the longitudinal coherence) of the SASE-FEL pulses by delaying the electrons with respect to the photons between undulator modules, thus increasing the cooperation length between electrons and photons [74–78]; and the short and high power FEL pulses based on superradiance [79,80] and implemented with a horizontally tilted beam [81,82] where only the on axis slice contribute to the lasing process and is replaced with a fresh one any time by means of the CHICs (which are designed to introduce offsets up to ± 0.3 mm if required).

Upstream the Athos beamline, two modulators separated by two magnetic chicanes have been recently (2022) installed to couple in two external lasers, ranging from 260–1600 nm wavelengths. This equipment is designed for multiple purposes and several options will be tested in the coming years. Nevertheless, the main application will be to seed Athos using the EEHG technique [83], today available for photon energies up to about 400 eV. The 0.2 m period length modulators are designed with high flexibility to fulfill novel requirements. The possibility to individually tune the strength of each of the 18 poles allow for extreme taper configurations, tune a subset of poles to a different wavelength and even to triple the period, reaching 0.6 m.

The first lasing results of Athos have been recently reported in Ref. [84]. In particular, the Athos team has demonstrated the capacity of the Athos beamline to reduce the saturation length by about 35% when using the optical klystron and helical undulator configuration (in comparison to the standard planar undulators and no optical klystron), the production of short pulses with higher power than in standard configurations following the superradiance regime, and the generation of variable polarization FEL radiation using the APPLE-X devices for photon energies at the keV level.

E. European XFEL, Germany

Gianluca Aldo Geloni, Suren Karabekyan, Jiawei Yan, and Svitozar Serkez.

1. Implementing polarization control capabilities at the SASE3 FEL line

At the European XFEL, two undulator systems for hard x-rays–SASE1 and SASE2, and one for soft x-rays—SASE3 have been successfully in operation since 2018 [85]. All systems were designed and equipped with variable gap planar undulators that could generate linearly polarized radiation. The SASE3 undulator system consists, in particular, of 21 planar U68 variable-gap undulators, each 5 m long with a period of 68 mm. Depending on the energy of the electron beam (8.5–17.5 GeV), it can generate radiation in the range from 0.24 to 4.6 keV. Due to high demand from users, a project to generate soft x-ray radiation with variable polarization was initiated in 2019 that consists in equipping SASE3 with an afterburner based on the APPLE-X undulator design developed at PSI [22,24,86] (see also Sec. II D). The idea is to use a micro bunched electron beam after a system of planar undulators and direct it into a system of helical undulators tuned to the resonant frequency, where it emits powerful coherent radiation with controlled polarization. To achieve a high degree of, for instance, circular polarization, it is necessary to suppress or cut off the linear polarization generated by the planar undulators. For this purpose, the SASE3 planar undulators are used in reverse tapering mode [60], where the bunching factor is approximately the same as for nontapered undulators, but the radiation power decreases by orders of magnitude. The results of a numerical 3D simulation using the FAST code [87] show that, for example, at a wavelength of 1.5 nm (0.83 keV), using the last 11 planar undulator cells with a total length of 55 m, in the 2.1% reverse taper mode, the linearly polarized power reaches a value of 0.4 GW, while the bunching factor increases continuously. The power of circularly polarized radiation generated by a 10 m long helical undulator, located directly behind the system of linear undulators, increases very rapidly and reaches up to 155 GW. Hence, the degree of circular polarization reaches a value of 99.9%. Similar results were obtained using a numerical three-dimensional SIMPLEX simulation [88]. Table V shows the simulation results for four wavelengths considering a helical afterburner of 8 or 12 m composition length [89]. These studies were the basis for calculating the electron beam optics in the installation area of the helical afterburner system. An APPLE X-type of a helical undulator was chosen to create a system of helical undulators for SASE3 [90]. The magnetic structure of helical undulators was designed to overlap the working range of planar undulator U68. The full length of the UE-90 magnet structure is 1.98 m, the undulator period

TABLE V. XFEL parameter.

Polarizationmode K-Range	LH/LV/C+C− 9.40–3.37	Linear 45°/125° 6.62–2.36
Photon energy range (keV)		
@8.5 GeV	0.169–1.141	0.33–2.012
@11.5 GeV	0.309–2.088	0.608–3.684
@14 GeV	0.457–3.095	0.902–5.459
@16.5 GeV	0.635–4.299	1.252–7.583
@17.5 GeV	0.715–4.835	1.409–8.530

length is 90 mm, the gap variation range is 12.5–31.6 mm, the longitudinal shift range of each magnet array is ±45 mm, and the permanent magnets material is NdFeB with the nominal remanent field of 1.26 T. The frame length of this undulator is slightly over 2 m. It was decided to use the existing design of the intersection and its components, with the afterburner section starts after the last SASE3 undulator cell.

The distinct advantage of the APPLE X undulator is the ability to change the radiation energy by adjusting the gap. This results in a significantly higher field uniformity compared to a fixed-gap delta undulator, where the field can only be controlled by shifting the magnetic structures relative to each other, resulting in large field gradients. This requires extremely small tolerances for the alignment of the fixed-gap undulator system and makes an alignment of extended systems almost impossible. Figure 12 shows a schematic of the project and the evolution of the radiation power from regular taper and reverse taper plus the afterburner. The table annexed to the figure presents the photon energy ranges generated by the UE-90 undulator by varying only the gap. The magnetic field simulations for LH, LV, C+, C−, and 45° linear polarizations have been performed using the Radia program [92]. The actual length of the installed afterburner is 8 m (four undulators)

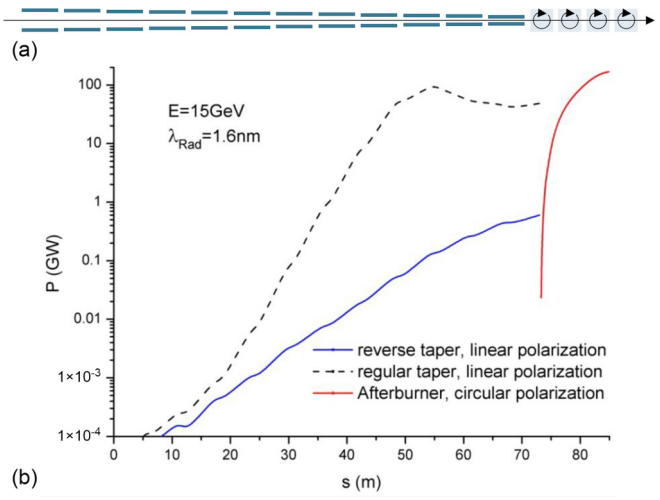

FIG. 12. Schematic of the project and the evolution of the radiation power from regular taper and reverse taper and afterburner [90], with (annexed table) the photon energy ranges generated by the UE-90 undulator by varying only the gap [91].

2. Current status of the project

At the time of writing, the project is at the stage of its completion and commissioning. During the winter shutdown 2021/2022, all four APPLE-X undulators were installed in the tunnel. The helical undulator system was connected to the control system and made operational together with all related components. During commissioning, calibration measurements were made to compensate for the magnetic fields to minimize the deflection of the electron beam from the optimized orbit. Measurements were also made to optimize the values of the phase shifters located between the helical undulators. After alignment of the electron beam and setting up SASE3 in reverse taper configuration, lasing was immediately obtained when all four Apple-X undulators were brought into resonance. This was achieved at a beam energy of 900 eV and a clockwise circular polarization mode (C+). Optimization of the phase shifter gap resulted in a 30-fold gain of the circularly polarized radiation over the linearly polarized radiation of the planar undulators. Later, lasing was also obtained for counterclockwise circular (C−), linear 45° (45°), linear vertical (LV), and linear horizontal (LH) modes. The photon beam energy was changed to 700 eV where lasing was obtained in LH, C+, and C− polarization modes. The availability of the APPLE-X afterburner will allow for further development of advanced polarization schemes, which will be based on flexible control of the electron bunching by means of the SASE3 undulator. Here we will discuss, in particular, two possible future options.

3. Possible future developments I: FEL radiation with orbital angular momentum

Undulator radiation pulses produced by a helical undulator at the hth harmonic of the fundamental carry OAM with topological charge $\pm(h-1)$ [93]. In Ref. [94], it was proposed to exploit this fact by preparing an electron beam bunched at the hth harmonic of the fundamental of a short helical radiator using the FEL process in a longer undulator preceding the radiator. Minimization of the background emission is obtained by reverse tapering. Due to the availability of the APPLE-X afterburner, this kind of setup is readily available at the SASE3 FEL, where tests will be carried out following the finalization of the afterburner commissioning. For further perspectives, see also Sec. II A.

Schematically, the setup looks like Fig. 13, with the possible addition of an electron pulse kick between SASE3 and the helical afterburner to decrease the radiation background from SASE3 even more [95]. However, now SASE3 and the afterburner are tuned at different frequencies, for example, 1000 and 500 eV, respectively. In this way, the beam entering the afterburner is bunched at 1000 eV and thus emits strongly at the second harmonic of the APPLE-X, producing radiation with OAM. Estimations of the output can be carried out semi-analytically by computing the bunching at 1000 eV via FEL simulations and subsequently calculating analytically the coherent emission in a short afterburner (assuming no gain). The energy (power) generated strongly depends on the electron beam transverse size.

This means that a magnetic optics solution with small betatron functions at the afterburner location is to be preferred.

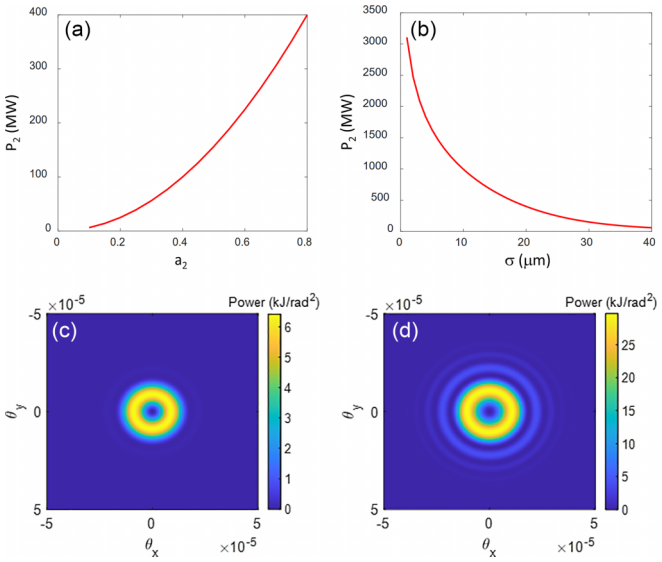

FIG. 13. Left. Emitted power from a 14 GeV electron beam entering the U-90 Apple-X afterburner after having been bunched in the main SASE3 undulator for a fixed transverse rms size of 20 μm (a) or a fixed bunching factor of 0.8 (b). Right. Output comparison for the beam with a bunching factor of 0.5 and a transverse size of 20 μm (c) and the beam with a bunching factor of 0.8 and a transverse size of 10 μm (d).

Figure 13 shows the dependence on the bunching factor at fixed transverse rms size and the dependence of the transverse rms size for a fixed bunching factor in the case of a normalized emittance of 0.5 μm and an electron energy of 14 GeV, assuming a flat-top, 20 fs-long profile with 5 kA peak current. The figure also shows two output profiles for two different bunching levels. This method is expected to produce GW-level pulses carrying OAM.

4. Possible future developments II: Polarization shaping

A second possible development concerns polarization-shaping technique, proposed in Ref. [96]. Consider two overlapping, longitudinally coherent pulses of radiation emitted in two separate parts of the APPLE-X radiators with orthogonal polarization states. If the two pulses have the same frequency, their superposition results in a different polarization state, which depends on the relative phase between the initial two. The resulting polarization state will be located somewhere on the large circle of the Poincaré sphere between the original polarization states. For example, if the two initial pulses are circular left- and right-polarized, by overlapping them one obtains a linearly polarized pulse, with the polarization plane depending on the phase difference. When the difference between the intensities and phases changes along the direction of propagation or across the transverse coordinates (or both), the degree of polarization, averaged over time or across the transverse direction, degrades. One can, however, control and maximize this effect so that the resulting polarization depends on the location on the sample and/or on the arrival time of the radiation within the pulse.

To obtain radiation pulses with shaped polarization one may prepare a background-free-electron beam with a temporally coherent bunching by combining soft x-ray self-seeding [97] and inverse tapering schemes [98]. This electron beam may then sequentially radiate in two of four consequent radiators—APPLE-X undulators, set to orthogonal polarizations.

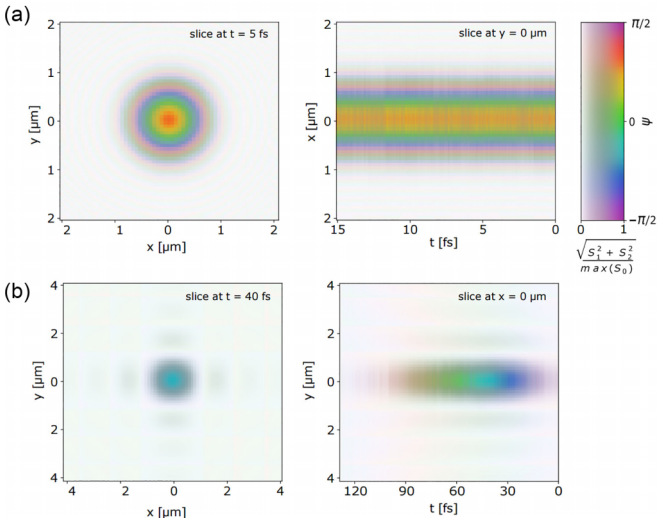

FIG. 14. Adapted from Figs. 9 and 10 of Ref. [96]: Radiation polarization properties calculated for the SASE3 beamline of the European XFEL. Subplots depict radiation intensity and orientation of the polarization plane in false colors as a function of transverse coordinates and time using setup geometry, optimized for *spatial*, row (a) and *temporal* polarization shaping, row (b).

To maximize transverse polarization shaping effect, one should maximize the distance between the active radiators. Once the sample is located between the waists of the radiator images, difference of wavefront curvatures of both polarizations would result in phase difference (hence the resulting polarization) depending on the transverse coordinate, see Fig. 14, row (a). With this method polarization may be shaped on down to sub-μm scale.

To maximize temporal polarization shaping (similar to that discussed in Sec. II A 3 b), one can make use of an electron beam with a linear energy chirp. The passage through the radiators results in a stretching of the beam, which affects its bunching frequency. Thus, the consequent raidators would emit pulses with slightly different frequencies. In other words, phase difference between the emitted polarized pulses will change over time. As a result, the resulting combined pulse would be polarized, but its polarization state would change as a function of time. The rate of this polarization shaping may be controlled with electron beam chirp and may reach frequency of THz scale, as illustrated on Fig. 14, row (b).

F. SHINE and SXFEL

Zhangfeng Gao, Bangjie Deng, Chao Feng, and Haixiao Deng.

The Shanghai Deep-Ultraviolet Free-Electron Laser (SDUV-FEL) [99] served as an integrated multipurpose test facility for FEL principles, laying a solid foundation for the Shanghai Soft X-ray Free-Electron Laser (SXFEL) [100] and Shanghai High-Repetition-Rate XFEL and Extreme Light

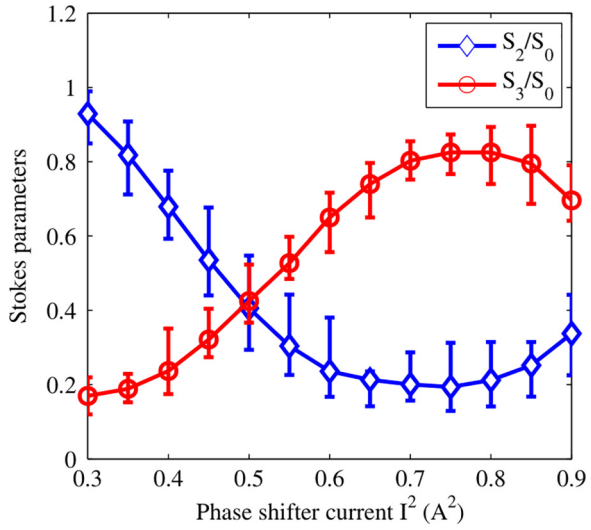

FIG. 15. Normalized Stokes parameters of coherent 523 nm radiation measured at SDUV-FEL.

Facility (SHINE) [101]. Among those FEL experiments carried out at SDUV-FEL, the FEL polarization switching demonstration was successfully performed in 2013, by means of the crossed-planar undulators technique [102]. The first practical success of this technique at a seeded FEL stands a good chance of fast polarization switching of short-wavelength FEL radiation. The principle is based on the superposition of the horizontally and vertically polarized radiation generated from two different types of planar undulators (the afterburner), which are perpendicular to each other. A pulse phase shifter is installed between the crossed planar undulators to delay the electron beam in the vertical planar undulator, thus controlling the phase difference between the horizontally and vertically polarized FEL radiation, which will directly lead to different final polarization states.

The 1047 nm seed laser was used in the modulator, and the 523 nm radiation (second harmonic) was generated from the afterburner. The EMU consisted of 10 periods with a period length of 65 mm, while the PMU-H and PMU-V both consisted of 10 periods with the period length of 50 mm. A division-of-amplitude photopolarimeter (DOAP), containing one optical lens, three beam splitters, four polarizers, one quarter-wave plate, and four photodetectors, was constructed to characterize the polarization degree of the FEL radiation. By dividing the incident laser into four separate beams, all the Stokes parameters can be measured at the same time, thus determining the final polarization degree in a single shot [103]. The Stokes parameters varies with the magnetic field intensity of the phase shifter, just as represented in Fig. 15, and the maximum polarization degree approaches 90% as long as the two FEL pulses are perfectly superimposed. The spatial overlap is also highly significant for the final polarization, which is mainly determined by the beam orbit and envelope in the afterburner, as well as the propagation of the FEL pulses between the last undulator and the detector.

SXFEL is the first soft x-ray FEL facility in China, and the project proceeds in two stages, the test facility (SXFEL-TF) and the user facility (SXFEL-UF). SXFEL-UF consists of two FEL lines, one SASE line and one seeding line, both of which are supposed to generate polarization controllable FEL radiation. Numerous simulations and several experiments on polarization have been performed at the seeding line (under SASE mode). Figure 16 shows the schematic of the polarization control scheme at SXFEL-UF. The upstream planar undulators with a step-gap reverse taper provide well-bunched electron beams with relatively low energy spread, as well as linearly polarized radiation with much lower pulse energy. The kicker serves as a switch to determine the orbit of the electron beams bunch by bunch, which makes it possible to control the position and intensity of the elliptically polarized undulator (EPU) radiation.

Due to lack of time for experiments, so far they are carried out with all the undulators tuned to generate 6.75 nm radiation. Eight planar undulators (length of 3 m, period length of 23.5 mm) and 2 EPUs (length of 3 m, period length of 30 mm) are used in the experiments, with a beam energy of 930 MeV. Figure 17 shows the normalized simulated faculae of linearly and circularly polarized radiation with proper reverse taper. The pulse energy of circularly polarized laser is over one order of magnitude higher than the upstream linearly polarized laser, which means the theoretical polarization degree reaches as high as 95%. In addition, by adjusting the reverse taper intensity, both linearly and circularly polarized radiation with similar pulse energy can be obtained in simulation at the same time as long as the kicker is working, as shown in Fig. 17. The experimental results match well with the simulated ones apart from the radiation intensity, which needs more time and attempts to improve. The pulse energy of circularly polarized radiation is around 15 μJ, seven times higher than the linearly polarized one. Besides, the experimental transverse profiles of radiation is also similar to the simulations when the kicker is on. Moreover, one EPU (length of 4 m, period length of 20 mm) is also going to be installed at the end of the SASE line, providing circularly polarized radiation at a shorter wavelength (2 nm). It is supposed to provide 70 μJ circularly polarized radiation with over 90% polarization degree.

SHINE is the first hard x-ray FEL facility in China, and it is still under construction. So far SHINE consists of 3 FEL lines, in which FEL-II covers the lowest photon energy (down to soft x-ray region) and contains 4 EPUs for polarization control. Numerous simulations have been done on the performance of the polarization control scheme, in which the 1 nm radiation case will be taken as an example. With a beam energy of 8 GeV, the period length of planar undulators is supposed to be 55 mm, the same as that of the EPUs. Figure 18 shows the pulse energy of the linearly polarized radiation, depending on whether a reverse taper is used, and nearly two orders of magnitude difference in radiation intensity can be observed. Since the pulse energy of circularly polarized radiation is as high as 700 μJ, the theoretical polarization degree is calculated to be over 99%. Moreover, FEL-III is expected to generate linearly polarized laser with different polarization directions, which still needs more theoretic and simulation supports.

Currently, inspired by the "CookieBox" instrument developed at DESY [6,63], a series of angularly resolving

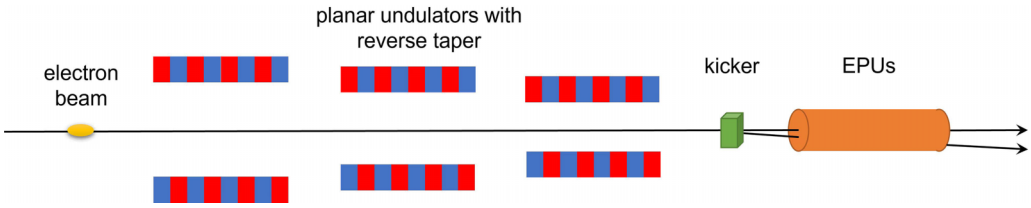

FIG. 16. Schematic of the polarization control experiment at SXFEL-UF. The kicker serves to bend the prebunched electron beam from the reverse tapered undulators to separate the circularly polarized radiation from the linearly polarized radiation.

polarimeters (called "ARPolar" instruments) based on measuring photoelectron angular distributionsare proposed, constructed or being offline tested at SXFEL and SHINE. The ARPolar instrument contains 16 μ-metal-shielded detection assemblies equipped with a electrostatic optical system and fast MCP detectors for both FELs' energy-spectrum monitoring and the polarity degree and angle measurement. The former is based on photoionized electrons' time-of-flight and the latter by means of measuring their angular distribution. All ARPolar instruments are designed to achieve a linear polarity resolution better than 2% for fully polarized XFELs. For soft x-ray FEL polarization diagnosis, two machines (ARPolar-CORE and ARPolar-SXFEL) are scheduled for the SXFEL facility. The prototype (ARPolar-CORE) is manufactured firstly for offline experimental validation of mechanics, vacuum and electronics system [104], and it is featured by the capability of high-resolution multichannel charge measurement with MHz repetition rates based on the nongated charge-to-time conversion principles using low-cost time-to-amplitude converters (TDCs) [104]. The ARPolar-CORE instrument will be installed at the seeding line of SXFEL facility. Meanwhile, the ARPolar-SXFEL instrument is supposed to be the successor of the ARPolar-CORE and featured by its design of error compensation because of FEL pulses' transverse positions for polarization diagnosis [105]. It is currently installed at the SASE line of SXFEL facility. For hard x-ray FEL pulses, the ARPolar-SHINE instrument is designed for the commission of polarization diagnosis on

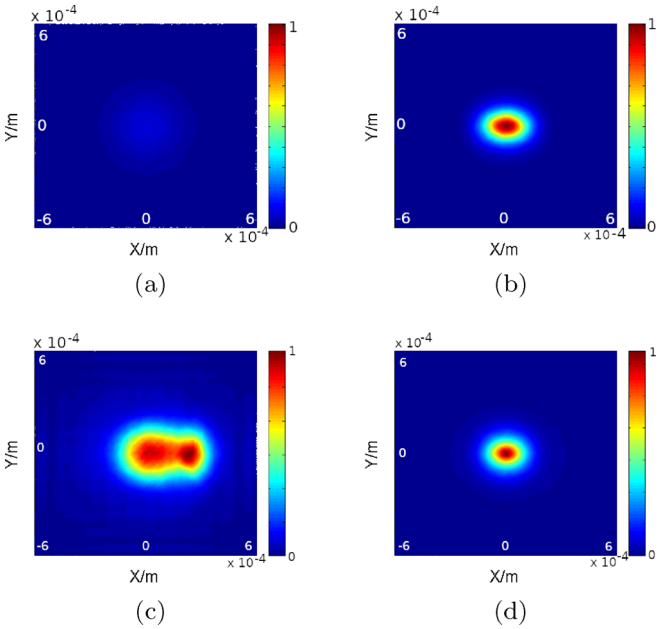

FIG. 17. The normalized simulated transverse profiles of linearly (a) and circularly (b) polarized radiation, and the simulated transverse profiles of radiation when the kicker is working (c) or not (d).

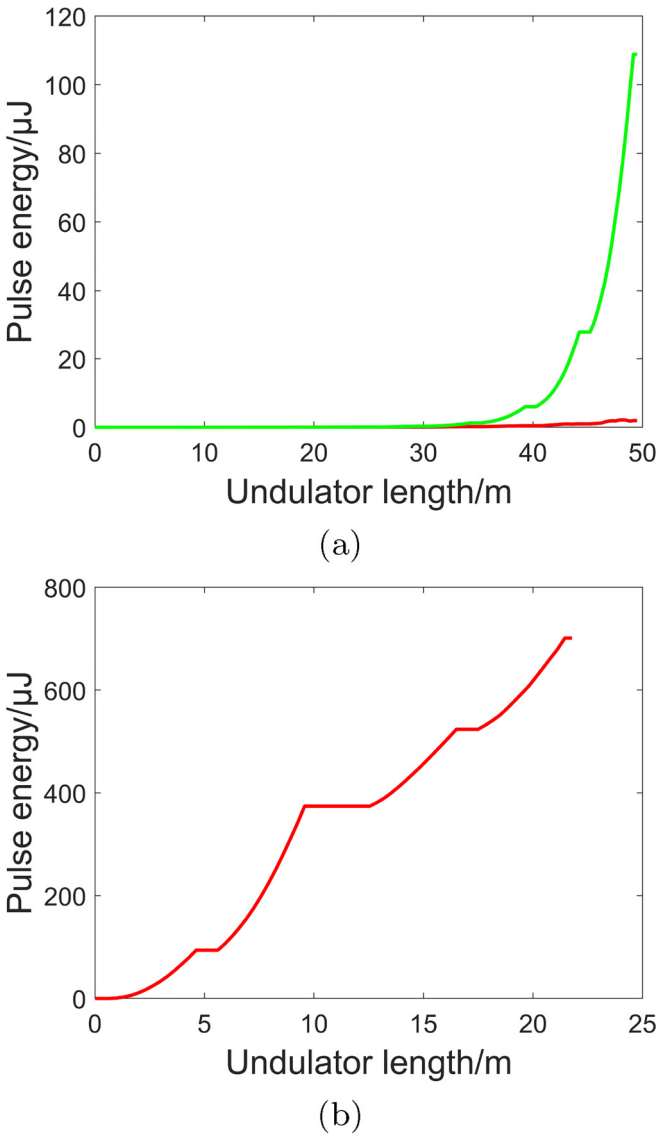

FIG. 18. The pulse energy of the linearly polarized radiation with (red) or without (green) reverse taper (a), and the pulse energy of circularly polarized radiation (b).

the FEL-II undulator line at the SHINE facility, covering an energy range from 0.4 to 3 keV.

III. EXPERIMENTAL PERSPECTIVES FOR POLARIZATION-CONTROLLED FELs

A. Instrumentation

Markus Ilchen, Wolfram Helml, and Peter Walter.

Free-electron laser facilities provide a unique variety of instrumentation for covering the interdisciplinary demands from diverse user communities. They typically offer a versatile and well-established instrument portfolio for users that is optimized and calibrated for the specific experimental endstations. The advantage for new users can be that, typically, an expert team of scientists and technical staff aids them in all steps of planning, experiment conduction, and even data analysis. Thus, externally provided equipment by users is not the common case but can also be adapted for specific experiments. In this section, we will sketch a selection of relevant instrumentation for investigations of stereochemistry and dichroic light-matter interaction at FELs. This selection aims to give an orientation for planning of new experimental campaigns within the roadmap's topic, stimulate collaborations and attract users to join the effort of gas-phase-based studies with polarization-controlled FELs.

For the initial demonstration of a stereochemically sensitive experimental scheme at an XFEL as a step toward time-resolved and nonlinear investigations of building blocks of life, the method of monitoring the forward-backward asymmetry of photoelectrons (PECD) [106,107] has been identified to yield large potential [108–111] (see also Secs. III C and III F). Photoelectron yields and their angular distributions have furthermore been used to investigate nonlinearly dichroic effects in atoms and molecules, as outlined in Sec. III D. Another recently emerged perspective is realized via exploiting the interplay of photonic spin and orbital angular momentum as indicated in Sec. II A and further detailed in Sec. III G. With the aim to derive highly differential information about specific structures and processes, schemes like (partial) covariance analysis [112] and coincidence spectroscopy [113,114] have been demonstrated to yield promising potential, also and in particular for investigations with polarization control (see Sec. III E). The latter technique is even offering complementary access to absolute configurations of molecular structures via Coulomb explosion imaging [115]. Currently, it is under development to complement or even combine these techniques with fluorescence spectroscopy [116], coherent-diffraction imaging [117,118], and x-ray scattering spectroscopy [119]. Some of the commonly employed instruments for gas-phase studies with polarization-controlled FELs are:

1. Velocity map imaging (VMI)

The VMI technique images a two-dimensional projection of the full three-dimensional velocity distribution of charged particles, here originated via photoionization, which provides both angular and velocity information over a 4π collection angle. It is based on the technique of ion imaging, introduced by Chandler and Huston [120], with the addition of the 2D imaging capability of a standard time-of-flight spectrometer with homogeneous fields, initially reported by Eppink and Parker [121]. Crucially, the latter authors have introduced an Einzel lens into the setup. Such a lens focuses charged particles with similar velocities to a distinct location on a position-sensitive detector such as a microchannel-plate assembly. The inherent "blurring" due to large interaction regions can be mitigated via a finite molecular source and/or ionizing beam [122,123]. The readout of the MCPs can be used for time-of-flight spectroscopy, or realized via phosphor screens that convert the charge-avalanche of the MCPs to visible light dots or via delay-line anodes [124–126]. In the first case, cameras can then record images of either accumulated "hits" or in the case of FELs, record single-shot spectra, even in a time-resolved fashion [127] using fast-decaying phosphor screens. A substantial limitation is the readout speed of the camera which poses a challenge to high-repetition-rate single-shot operation, which is an important development at FELs as discussed in Sec. II. In general, VMIs have enabled new approaches to ion- and photoelectron spectroscopy for molecular photodissociation, collision and reaction-dynamics investigations [123], attosecond spectroscopy and stereochemistry, to name a few topically relevant fields of interest. While historically, charged particle imaging has been applied separately for the detection of positive ions and electrons, another important extension is to image the ions and electrons in coincidence or covariance to isolate particles from specific ionization channels. Nowadays, such double-sided VMIs are state-of-the-art setups at XFELs [128–130]. It is notable that a so called coaxial VMI, where the beam passes through the detector to enable a perpendicular projection axis to the standard case, has been used at LCLS for retrieving temporal x-ray pulse characteristics via angular streaking [131].

2. COLTRIMS/REMI

A conceptually similar instrumental setup to VMIs can be used as cold target recoil ion momentum spectrometer or COLTRIMS [113,114,132] as will be discussed in detail in Sec. III E of Dörner and Jahnke. To give a peek into this powerful technique, we briefly introduce the technique here. One of the decisive differences between a VMI and the COLTRIMS approach is its capability of imaging the full three-dimensional momentum space instead of only a two-dimensional projection. In addition, COLTRIMS is intrinsically a coincidence measurement scheme. These advantages of full coincidence come at the price that single-molecule conditions must be met during the measurement, i.e., only one atom or molecule may interact with the ionizing projectile beam inside the interaction volume at a time. This implies that one of the most significant challenges lies in maintaining stringent vacuum conditions and employing a highly dilute molecular jet as the method for sample delivery. The COLTRIMS technique has been developed to give access to kinematically complete experiments on atomic and molecular-fragmentation processes by coincident and momentum-resolved detection of recoiling target ions and emitted electrons, and has been shown at XFELs [133,134]. Through the momentum vectors of all emitted electrons and ionic fragments in the same event the

entangled many-particle dynamics in the molecular system can be explored via Coulomb-explosion imaging, which, at FELs, allows to image single molecules in the gas phase [135,136]. Where it recently has been shown at European XFEL that a molecule size limitation can be advanced to larger systems via the absorption of many photons before substantial molecular restructuring can occur [13].

3. Time-of-flight (TOF) spectroscopy

Time-of-flight (ToF) spectroscopy converts "flight" times of charged particles from an ionization event in the interaction region between the investigated target and the photon pulse, to kinetic energies via their simple physical relation. For the common case of using microchannel plates (MCPs) as fast-response detectors, the electron and ion-mass spectra can be generated in two ways, either by counting the events and accumulating a histogram over many pulses or by recording the current through the MCPs. The latter is a prerequisite for some diagnostic methods at FELs, as outlined below, and also decisively extends the methodology for FEL applications. Notably, such detector operation poses a variety of new challenges that are under development but also yields large potential due to the unique capability of accommodating single-shot spectroscopy up to high repetition rates from kHz to MHz, meeting the full range of currently available machine operation modes [137]. ToF-spectrometers can be tailored in a way that charged-particle optics, i.e., electrostatic sections with independently adjustable potentials, decelerate the particles for retrieving maximum energy resolution also for high kinetic energies. These lenses can also be used for acceleration and shaping of the trajectories for increasing the collection efficiency. Electron ToF-spectroscopy can provide relatively high-energy resolution, moderate collection efficiency and/or angle-resolved spectroscopic insights into a broad variety of scientific questions at pulsed sources like FELs, also in different sample environments [27,63,137–139]. Collection efficiency and energy resolution are in a trade-off balance and can be adapted to specific experimental needs. It is noteworthy that angle-resolving time-of-flight spectrometer setups have expanded their application toward FEL-based investigations and diagnostics [37,65,137,139,140] even in nondipole geometry for retrieving asymmetric angular distribution patterns which are manifested through forward-backward asymmetries and thus potentially causing differentiation issues with PECD signatures [138]. For experiments requiring high collection efficiency, magnetic-bottle spectrometers can be employed for ions as well as electrons at the cost of angular resolution [141,142]. In the light of stereochemistry, such spectrometers can be used for tracking small changes in photoionization yields due to swapping the helicity of polarization.

4. Hemispherical analyzers

Another type of electron detector is the so-called hemispherical electron energy analyzer or hemispherical deflection analyzer. It is usually used where very high-energy resolution is needed and was also the instrumental choice for the first discovery of a PECD from the liquid phase [143]. The analyzer maps kinetic energies to positions on a detector by two concentric conductive hemispheres that serve as electrodes which bend the trajectories of the electrons. This bending separates the different kinetic energies electrons in space. Selecting specific trajectory radii via a narrow slit at one end enables energy resolutions down to fractions of meV. The resulting disadvantage is a directly correlated energy window as well as reduced collection efficiency. Performing two independent measurements with left- and right-handed polarized light while keeping the angular orientation, one can for example measure the forward-backward asymmetry of chiral molecules site-specifically with very high resolution [143,144]. The superior energy resolution can furthermore be important for investigations of energetically similar resonances and -fine structures in chiral and also transient matter.

B. Diagnostics

Markus Ilchen, Lars Funke, Wolfram Helml, and Peter Walter.

Accurate and robust diagnostics at FELs need to give immediate feedback in real time for advanced experimental schemes and methodology. Ideally, they provide online, noninvasive characterization of every incoming FEL pulse and cover a broad variety of machine operation parameters. Knowledge about all relevant x-ray parameters including the intensity, spectrum and chirp, and ideally the full time-energy structure of the pulses, in combination with their arrival time, wavefront, and focus size and shape, as well as state and degree of polarization thus enables access to a variety of new scientific areas and otherwise inaccessible states of matter. The available diagnostic details may even crucially influence the choice and optimization of instrumentation for experimental FEL studies.

In a very contemporary effort, machine-learning approaches have been identified and initially demonstrated to add new perspectives to the growing toolbox of photon metrology [145]. They thrive toward enabling active experimentation, i.e., actively steering the interplay between diagnostics for photon characterization, instrumentation and machine operation, launching an endeavor that has been gaining increasing attention by the FEL community [146].

To date, several of these diagnostic challenges have already been met, providing detailed information about the ultrashort and ultrabright photon pulses of free-electron lasers. Successful operation of beam-position [67,100,147–151], spectral [100,152,153], and intensity [154] diagnostics as well as wavefront [155–158] and focal-spot characterization have been important pillars for machine, beamline, and experiment commissioning at (X)FELs.

Furthermore, correlation of photon- to electron-beam-based diagnostics has been a vital asset and important cross-check, as many derivable properties of the electron bunch are imprinted on the photon pulses as well [159–161].

In the light of the topical orientation of this roadmap, it is noteworthy that the commissioning of undulator-based polarization control for ultrabright and ultrashort pulses was pioneered at FERMI and has spear-headed the effort toward polarization diagnostics at short-wavelength FELs [37,162]. Here, a multiexperiment approach was used that combined electron-bunch diagnostics, photoionization of simple atomic

targets in the gas phase for noninvasive polarization diagnostics at the experimental endstation and a VUV optical polarimeter in simultaneous operation. In addition, a fluorescence polarimeter at a neighboring beamline was employed for sequential diagnostic validation [37].

Since the approach of noninvasively measuring the dipole patterns of electron emission from direct photoionization yields information about the degree of linear polarization, it was thus possible to obtain an estimation for the degree of circular polarization under the assumption that the amount of randomly or unpolarized light is negligible. This assumption of absent unpolarized light requires validation via an experimental scheme that can directly access the actual amount of circular polarization. As first demonstration, we have chosen to pursue this validation via measuring the circular dichroism in the formation of sidebands [163]. Here, gaseous helium was ionized with circularly polarized XUV photons and the ionization region was spatially overlapped with a temporally synchronized optical laser of either corotating or counterrotating field vectors. The ionized helium can absorb or emit these quanta of energy that correspond to the energy of an optical laser photon. The yield of the individual sideband's formation crucially depends on the degree of polarization and provides the required information of an absolute degree of circular polarization that in turn can validate the assumption of absent randomly polarized light. The sketched experiment of Mazza *et al.* did not only demonstrate the first FEL-based CD in the gas phase, it also gave access to a more complex nonlinear CD formation in an oriented atomic system [164] as will be discussed in more detail in the dedicated section below (see Sec. III D).

The first FEL entering the x-ray regime, i.e., the LCLS at SLAC in the Unites States, capitalized on another approach to provide undulator-based polarization control as sketched in Sec. II B. The Delta afterburner undulator was a pioneering approach in several regards. Using an afterburner scheme to produce highly intense pulses of several hundreds of μJ requires a prebunched electron beam that has not significantly lased before entering the quadrupole Delta undulator of 3.4 m length. The residual amount of linear polarization that was produced upstream of the Delta undulator was blocked by adjustable jaws, thus only propagating the off-axis circular-polarization beam. As discussed in Sec. II B and by Lutman *et al.* [27] in detail, the upstream-produced linear polarization can also be used for a variety of pump–probe schemes, which ultimately enabled the very first stereochemically sensitive experiment with a chiral molecule at a short-wavelength FEL [110] (see Fig. 19 and also Sec. III C). The polarization diagnostics for the commissioning of the Delta undulator, in this case provided in almost real time, were again realized via angle-resolving photoelectron spectroscopy in noninvasive operation. However, in this scheme, it was even more crucial to validate the methodological approach of dipole-based electron spectroscopy since the approximation of negligible randomly polarized light was less substantiated compared to FERMI, where all undulators are quadrupole-magnet structures. We thus performed the first sideband-based CD experiment with an FEL on a molecule, in this case oxygen, to determine the absolute degree of circular polarization [65]. It is noteworthy that the observed indications of very

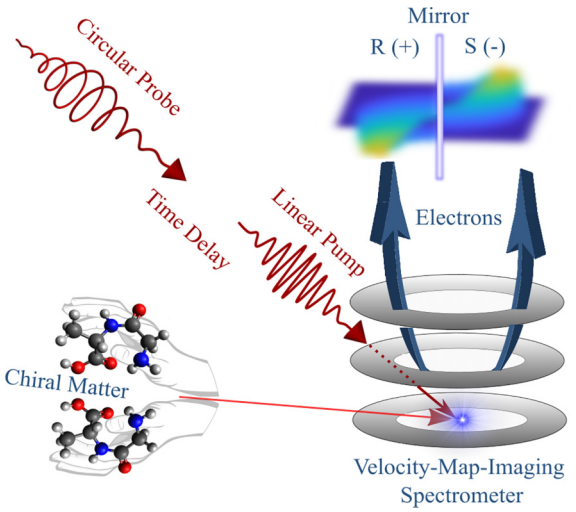

FIG. 19. Adapted figure from Ref. [110] illustrating a possible experimental scheme for pump-probe investigations of chiral systems (here glycyl-l-alanine) by VMI spectroscopy.

high degrees of circular polarization from the dipole-geometry diagnostic campaign were supported by the first CD measurement, which, for the LCLS, unexpectedly revealed an achievable degree of polarization close to unity. This joint effort of machine scientists and photon diagnostics uniquely enabled first access of an XFEL to studying nonlinear and transient processes in a chiral molecule with full site specificity [110], as indicated above.

To accommodate noninvasive diagnostics, typically a gaseous target of limited complexity is employed, i.e., atoms or small molecules. More recently, the challenge has risen to not only provide online polarimetry but the whole pulse structure including its time–energy distribution, i.e., the substructure in time together with the FEL pulse spectrum, in addition to the degree of polarization and the pulse energy. For FELs based on the principle of SASE, the pulse intensity substructure is given by a sequence of very short spikes, whose number, temporal widths, amplitudes, and phases start from shot noise and change stochastically from shot to shot [165]. With these demanding requirements in mind the need for advanced diagnostics and instrumentation becomes obvious.

The baseline hardware for uniting all of these functions in a single apparatus was again provided by the already described angle-resolving photoelectron spectroscopy device mentioned above [37]. However, for the inclusion of time–energy structure characterization at a SASE FEL with online feedback capabilities, a polarization controllable optical laser with specifically chosen wavelength adapted to the pulse duration window of interest is required for the implementation of angle-resolved photoelectron streaking [6,166–168].

Furthermore, a promising perspective for online data analysis in this regard is artificial-intelligence processing for keeping up with the high repetition rates of state-of-the-art FELs in real time [146]. In the light of the globally emerging high-repetition rate FELs, not only the associated data load and the demanding reconstruction of SASE pulse substructures pose challenges to noninvasive online diagnostics. A crucial factor is the choice of the employed experimental

setup since single-shot spectroscopy at high-repetition rates is still an elusive development. MCP-based electron ToF-spectroscopy has shown promising potential to comfortably enter the kHz regime. However, burst-mode schemes with 10 Hz bunch trains and intra-train spacings down to the order of 200 ns like at European XFEL and FLASH as well as the planned continuous MHz operation at LCLS II in the USA and SHINE in China require new developments to meet the correspondingly high replenishing rates for the MCP detectors as well as accommodating available readout schemes.

For the currently evolving XFEL-based measurements with attosecond resolution, not only the relative arrival time between the pump and the probe pulse but also the temporal structure of the pulses becomes important, especially for the stochastic SASE pulses, which are strongly modulated on the (sub)femtosecond timescale, depending on a variety of parameters such as the photon energy. Importantly, the full reconstruction of FEL pulses is crucial for a variety of experimental schemes and scientific investigations.

In the angular streaking scheme, a similar detection geometry can be used as for the measurement of the polarization state described in Refs. [6,37,163]. The x-rays ionize a gaseous target and promote photoelectrons from the bound state to the continuum with a given excess kinetic energy. In our previous efforts [6], the photoelectrons were measured by 16 dipole-encircling ToF-spectrometers, but complementary schemes have been developed as well at LCLS [169]. In the case of angular streaking experiments, the copropagating IR laser is circularly polarized, in contrast to standard attosecond-streaking setups with linear streaking laser polarization. The effect of the IR laser interacting with the emitted electrons can be understood classically as a driving force exerted by its instantaneous electric field, thus changing the electrons' momenta dependent on the moment when the electrons are set free. This momentum change translates to an angularly varying electron kinetic energy in the presence of a circularly polarized streaking field. The direction of the IR polarization vector determines the coordinates along which electrons, ionized at this specific time, are losing or gaining energy on their way to the detector. Thus, the complete distribution of electron energies in the dipole plane over the whole FEL pulse mimics the duration of the pulse shape, while the relative electron count rates per energy bin of the measured traces correspond to the intensity structure of the pulse.

We have successfully shown at the LCLS [6] that with this scheme it is possible to measure the full time–energy structure of SASE FEL pulses in a single shot down to, currently, the few-hundred-attosecond level. Following this, we implemented the angular streaking technique at the European XFEL and combined the measurement with an online analysis, built on pretrained machine-learning networks for characterizing various important FEL pulse parameters on the fly [146]. The employed algorithms demonstrated the promising potential of ML methods to cope with complex pulse characterization schemes at (noncontinuous) MHz rate.

We are currently developing a dual-interaction plane chamber called "spectrometer with angular resolution" (SpeAR), in which the angular-streaking measurement for FEL pulse characterization can be conducted in line with a second dedicated experiment on a separate target (see Fig. 20). The sketched technological advances are not only the key to approaching site-specific electron dynamics in chiral molecules and studying their interplay with nuclear dynamics, they also open the door for combining gas- and liquid-phase experiments.

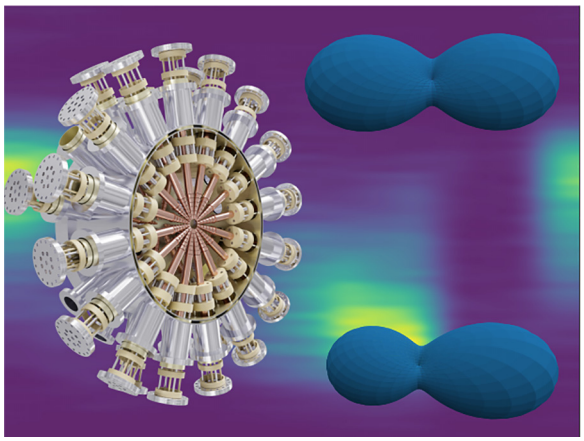

FIG. 20. Illustration of polarization characterization from streaked electron spectra. Left: CAD drawing of a new dual-interaction-plane time-of-flight apparatus for atto-streaking. The background shows angle-resolved data from the first angular streaking campaign at European XFEL from June 2022. The insets on the right illustrate the three-dimensional angular distribution patterns for (top) linear FEL polarization of unstreaked electrons versus (bottom) electrons streaked by a circularly polarized laser.

For the successful integration of ultrafast time-resolved and polarization-dependent measurements at the attosecond frontier, we here demonstrate how to simultaneously characterize the FEL polarization via the angular electron intensity distribution in the presence of a circularly polarized streaking field. The insets on the right of Fig. 20 show a clearly observable signature of the x-ray polarization imprinted on the measured PAD in the streaked angle-dependent electron intensity distribution. In this case, we compare the effect for linear FEL polarization and circular streaking field with zero (upper right) and relatively strong streaking field (bottom right) and photoelectrons with an maximum anisotropy parameter, i.e., $\beta = 2$. When the photoelectrons are subject to the additional field of the circularly polarized streaking laser these angular distributions are changed. The deformed electron distributions can be mathematically reproduced, clearly showing that the deformation in the electron distribution pattern from the original one produced by the linear FEL polarization is the more pronounced the higher the streaking effect is chosen. Thus, the effect of streaking can be disentangled from the original PAD by calculating the absolute square of the momentum probability amplitude in the strong-field approximation [170]

$$b(\mathbf{p}) = i \int_{-\infty}^{\infty} \mathbf{E}(t')\mathbf{d}[\mathbf{p} - \mathbf{A}(t')] \times \exp\left(-i \int_{t'}^{\infty} \frac{1}{2}[\mathbf{p} - \mathbf{A}(t'')dt''] + iI_p t'\right) dt'. \quad (1)$$

Here, $\mathbf{E}$ is the x-ray electric field, $\mathbf{d}$ the transition dipole moment, $\mathbf{p}$ the photoelectron momentum, $\mathbf{A}$ the streaking laser vector potential and I_p the ponderomotive potential.

A variety of additional promising developments in terms of single-photon-counting and time-resolving cameras, as well as x-ray and fluorescence spectrometers in combination with a variety of methodological and diagnostic novelties (see also below) are set to enable new experimental pathways for a new user community around chirality and dichroism science at FELs.

A sketch of the relevant instrumentation and diagnostics in the accelerator tunnels can be found in the respective sections above and references therein.

Furthermore, it shall be emphasized that advanced sample-delivery methods (see, e.g., Sec. III H) for gas-phase applications are an important prerequisite for the here focused kind of FEL experiments, and that gas-phase applications will be synergistically complemented by liquid-and solid-phase experiments. A detailed description is, however, not within the scope of this paper.

C. Opportunities for exploring ultrafast and nonlinear stereochemistry

Mats Larsson and Vitali Zhaunerchyk.

Ammonia is the textbook example of a molecule that oscillates between two different structures. The nitrogen atom can either be located above the three hydrogen atoms located in a plane, or below the same plane at an equal distance from the plane as when the nitrogen atom is above. From a quantum mechanical point of view all other degrees of freedom (rotation, vibration) can be neglected, and the system can be treated as a two-state system. The two forms correspond to different structural forms, and the barrier for interconversion between them is sufficiently low so that the nitrogen can tunnel between the two structures at a high rate (about 10^{10} s^{-1}).

When the molecules get more complicated they can no longer invert themselves either by quantum mechanical tunneling or thermal agitation. As expressed by Anderson in his famous article "*More is Different*" [171]: "*At this point we must forget about the possibility of inversion and ignore the parity symmetry: the symmetry laws have been, not repealed, but broken.*" In fact, chirality was the first example of spontaneous symmetry breaking, later followed by other type of symmetry breaking in both chemistry and physics. Thus, we have been used in thinking about the molecules of life having only one of the two enantiomeric forms; amino acids are L-chiral whereas sugars are D-chiral. However, if we synthesize sugar by chemical reaction, then a racemic mixture with equal amounts of the two enantiomers is obtained. Nature's maintenance of homochirality is surprising since it requires energy. The entropy is lower in a chiral system than in racemic mixtures.

A traditional spectroscopic method to detect chirality is based on circular dichroism (CD). In this method an investigated sample is irradiated with circularly polarized light (CPL) with photons from infrared to the near-ultraviolet regions and chirality is inferred from differences in absorptions of right- and left-handed CPL. It has been suggested that CD can be enhanced by using azimuthally and radially polarized vector beams or by using light with orbital angular momentum [172,173]. CD in the x-ray regime allows, in particular, selecting a molecular site being core-excited or -ionized. For example, as was shown in Ref. [174] for core-resonant CD, the magnitude of the latter depends on the location of the initially excited site and chiral center, i.e., the site-specificity capability inherent to x rays enables manipulating the strength of CD. The main disadvantage of the CD method is that CD signals are rather weak. Photoelectron circular dichroism (PECD) is another approach to sensing chirality and it is usually few orders of magnitude more sensitive to chiral configurations than the conventional CD (see also Sec. IV D).

Ever since Pasteur discovered molecular chirality in the 19th Century, and it was realized that the origin of chirality is the tetrahedral asymmetric carbon atom, chirality has been viewed to a large extent as a static phenomenon. A molecule is either achiral, and if it is chiral it can occur in only two possible enantiomeric forms. The development of free-electron lasers has opened new perspectives for time-resolved PECD (TR-PECD): apart from providing access to the femtosecond time-window, the x-ray FELs offer the element- and site-specificity.

A new generation of experiments to probe ultrafast chiral dynamics is still in its infancy. One of the envisioned experiments investigates the so-called transient chirality. It requires an amplified, ultrashort optical laser to photoinduce some change in the molecule, and an x-ray probe with circularly polarized light. The optical pulse can for example induce a transition in a molecule from an achiral ground state to a chiral excited state where the molecules switches from one enantiomeric form to the other on a short timescale. The x-ray can then probe this oscillatory motion as a function of time. For a simple molecule with only a single carbon atom this situation is very similar to the ammonia case, with the exception that the evolving chirality takes place in an excited state and not the ground state. For more complex molecules, one can expect the signals from different cores to be different, with complex dynamics on different timescales. Feasibility of such experiments has theoretically been demonstrated in Ref. [175]. The case of formamide was considered as the molecule has a planar achiral structure in the ground state but upon electronic excitation becomes chiral with a low inversion barrier between two enantiomers. The authors showed that if CPL is used as a pump with a pulse duration of tens of fs, an enantiomeric excess is created that bounces back and forth between two enantiomers on a hundred fs-timescale. Such an oscillatory behavior can be probed by fs-short x-ray pulses from FELs with photon energies at and exceeding the C, N, and O K-edges.

Another interesting research topic related to ultrafast chiral dynamics is fragmentation of chiral molecules into achiral fragments or, vice versa, fragmentation of achiral molecules into chiral fragments. Such experimental studies will bring insight into the question whether transition from chirality to achirality is similar to a "quantum jump" in quantum mechanics (i.e., a process that can only be described as "before" or "after") or it is a continuous process for which the degree of chirality can be quantified as a function of time (see also Sec. IV D). In these envisioned experiments photolysis can be initiated by an ultrafast optical or x-ray pulse, products of which are probed with circularly polarized x-ray photons (Fig. 21). Such experiments have been initiated [110] and will benefit from future FEL upgrades, such

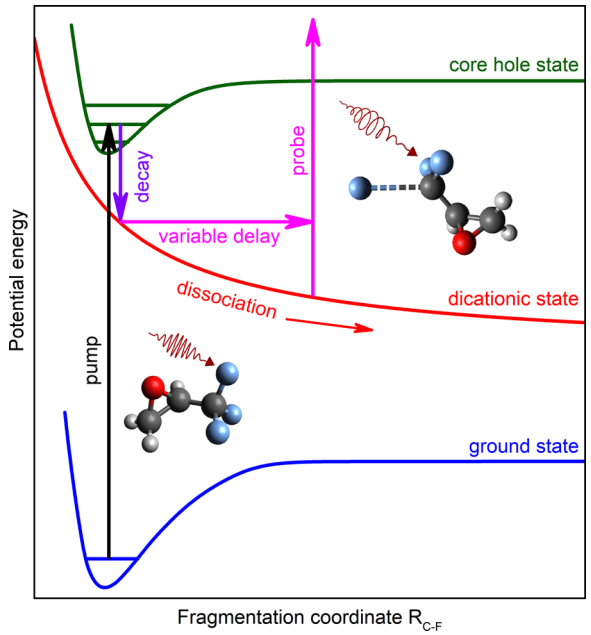

FIG. 21. A possible pump-probe experiment to investigate ultrafast chiral dynamics. The pump pulse core-excites or -ionizes a specific molecular site leaving the molecule unstable toward dissociation. Chirality of the dissociating molecule is probed with CPL via PECD. The figure has been adapted from Ref. [110].

as repetition rate, pulse duration, seeding, and polarization control.

The access to XFEL pulses of the intrinsic atomic units of time (i.e., attoseconds) will make it possible for the first time to study how the electron dynamics control the nuclear motion. In femtochemistry pump-probe techniques were developed to directly probe the nuclear motion, while the electron dynamics was inaccessible. With isolated x-ray pulses with a duration in the attoscond regime, one can perform pump-probe experiment where the pump laser is in the UV/VIS part of the spectrum and with a duration of a few femtoseconds, whereas the probe pulse is an x-ray attosecond pulse. The x-ray pulse will ionize the molecule, with the electrons carrying information about what happened during the pump phase. FELs generating circularly polarized attosecond x-ray pulses will open the door to locally sensing electron dynamics in chiral molecules on the attosecond timescale. It can in particular be applied to study whether the electron dynamics in the L- and D-forms of chiral molecules is the same, or whether there are differences owing to the handedness. It can in particular be applied to study how the electronic structure and its dynamics in the L- and D-forms of chiral molecules differ owing to the structural handedness and how this stereochemically relates to the role of the Coulomb potential.

D. Nonlinear circular dichroism studies

Michael Meyer and Tommaso Mazza.

CD in photoionization is defined as the difference in electron emission probability after the interaction with right and left circularly polarized light. In one-photon processes, a nonzero CD is given, if the target itself has nonzero chiral properties, since unpolarized atoms or nonchiral molecules will show a CD equal to zero. However, in two-color pump-probe experiments it was demonstrated that polarized target states can be prepared by the first color photon, so that a nonzero CD can be measured using the second color photon [176–178]. These studies were performed in the linear intensity regime using synchrotron radiation in combination with optical lasers and the intermediate polarized state was prepared in general by resonant excitation to increase the efficiency of the two-photon process.

Similarly, the CD from nonoriented targets is generally also zero in the nonlinear regime, when the ionization is driven by several identical photons [179]. Nonzero CD is only observed by realizing a two-color multiphoton ionization [180]. Here, a circularly polarized photon of one color orients the systems via single- or multiphoton interaction and causes thereby a different response to the photon of different color for right-and left-handed circular polarization [181].

The prototypical two-color nonlinear photoemission (ionization) process is laser assisted photoemission or two-color above-threshold ionization (ATI) [182]. Experimentally this process is observed by the appearance of so-called "sidebands," which show up in the photoelectron spectrum on both sides of the main photoemission line and which can be interpreted as additional absorption or emission of one or more optical photons. This interaction scheme allows accessing detailed information on the electron dynamics of small quantum systems on the femtosecond timescale, exploiting the modification of the x-ray-induced ionization, specifically of the kinetic energy and the angular momentum of the outgoing electron, within a strong optical dressing field [183,184]. Performing the investigations with well-defined, but changeable linear polarization for the photon sources has demonstrated to provide unique information of the photoionization process [184,185]. The intensities of the two-color ATI lines, which are determined by the relative strengths of the partial electron yields at a given photon energy, change in a characteristic way as a function of the relative orientation between the two linear polarization vectors and show strong modulations as a function of the intensity of the optical laser field.

The availability of intense, circularly polarized short-wavelength radiation provided by free-electron lasers such as FERMI [32], LCLS [27], or, in the near future, the European XFEL [21] has opened recently the possibility to extend these nonlinear studies also to the observation of CD in photoionization [184]. For the two-color ATI process, measurements of the CD enable much deeper insight into the photoionization dynamics, in particular by recording the photoelectron angular distributions (Fig. 22). The anisotropy parameters, which are characterizing the angular distribution change strongly for the different sidebands as a function of the laser intensity [186]. Oscillations between $+1.5$ and -1.5 were predicted, e.g., for the β_2 parameter of the first sideband for laser intensities in the range of $1 \times 10^{12}\,\mathrm{W/cm^2}$ to $1 \times 10^{13}\,\mathrm{W/cm^2}$. The experimental verification of these strong oscillations has been a major challenge, since effect of volume integration, and therefore the influence of a large range of intensities, has to be considered in the modeling of the observation [184]. In general, measurements of the CD in the electron angular dis-

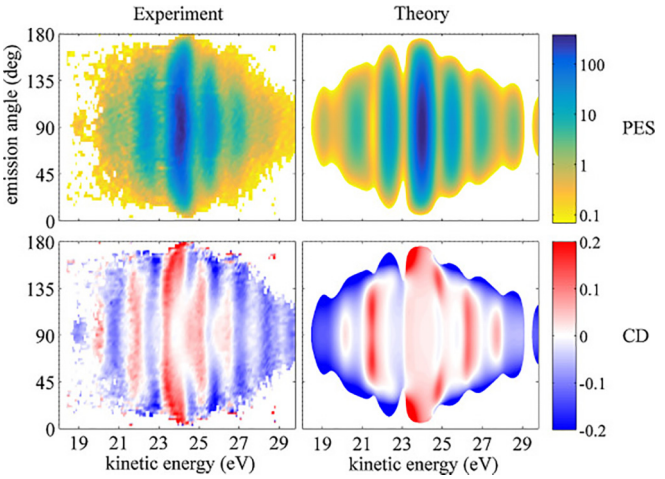

FIG. 22. Experimental (left) and theoretical (right) angle-resolved photoelectron spectra of atomic helium recorded at an XUV wavelength of 25.6 nm and a peak NIR intensity of $7.2 \times 10^{12}\,\mathrm{W/cm^2}$ (top) and the corresponding patterns for the angle-resolved CD (bottom). The theoretical spectra are calculated accounting for the spatial distribution of the NIR intensity, volume integrating the different values contributing to the two-color ionization process. The figure has been adapted from Ref. [184].

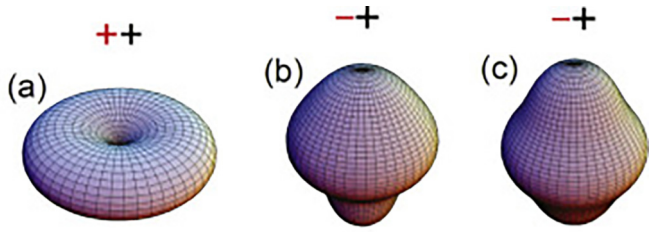

FIG. 23. PADs of the ATI of the inner 1s shell of neon for a XUV photon energy of 2 Â keV and an optical (NIR) photon energy of 1.5 eV. The helicity of the beams is indicated on top of each representation. Panels (a) and (b) include the first-order nondipole corrections, whereas panel (c) shows the PAD under the dipole approximation. The figure has been adapted from Ref. [184].

tribution have been very important, since they were identified as a possible route for the realization of a so-called "complete" experiment, i.e., the determination of the photoionization amplitudes and their phases [186]. Moreover, CD in two-color ATI has been successfully employed as a metrology tool to determine the circular polarization of XUV light [65,163], allowing to quantify the contribution of unpolarized radiation in a circularly polarized beam.

In a pump-probe approach, circularly polarized XUV FEL radiation is also used to resonantly excite the sample. For example, helium ions prepared in the He+(3p, m = +1)-oriented state by a sequence of ionization and resonant excitation were probed by nonresonant multiphoton ionization by IR photons corotating or counterrotating respect to the XUV [109]. In this study, and in the experimental work that followed it [187], a strong CD was observed in the nonlinear ionization of the oriented resonance. In addition, a strong dependence of the CD on the probing IR intensity was reported. A CD close to unity, i.e., a dominating ionization pathway for corotating pulses, was measured at low intensities. This strong CD was explained by destructive interferences between different ionization pathways in case of counterpropagating pulses, compared to corotating pulses where the ionization proceeds dominantly by only one pathway. This interpretation was corroborated by the angular distributions measured for the outgoing electron, which were in perfect agreement to the theoretical simulation of the process. At higher intensities, a strong change leading to the inversion of the sign is observed. This is interpreted including strong-field effects such as the polarization dependent AC stark shift as well as the role of resonant excitation processes [188]. Moreover, Freeman resonances [189] are shown to dominate the evolution of the intensity dependent CD for this multiphoton process and lead to strong differences in the electron angular distribution for different combinations of left- and right-handed circular polarization [187]. The observed CD in these experiments performed at laser intensities up to $10^{13}\,\mathrm{W/cm^2}$, i.e., within the perturbative regime, is in general positive as the consequence of a higher ionization yield for corotating pulses. This is different from what was measured at higher intensities ($> 10^{14}\,\mathrm{W/cm^2}$), where the electron emission in the regime of tunnel ionization [190] was dominating for counterrotating pulses.

XUV radiation brings wavelength selectivity as a most relevant feature, which can and was exploited in the mentioned experiments to prepare a well-defined oriented system either in a bound (autoionization) or a free (continuum) state. In perspective, the extension of this scheme to even shorter wavelengths will open the path to new classes of experiments, namely the investigation of CD in the excitation of core resonances and the study of nondipole effects in the photoemission. These perspectives are briefly addressed in the following. An elliptical dichroism has been predicted for the two-photon ionization of the 1s electron in atomic Neon [191]. The observable is the electron angular distribution, which also shows a strong photon energy dependence. In addition, using intense circularly polarized photons for the pump process, strongly oriented intermediate states of high angular momenta can be populated by multiphoton excitation. As a consequence, a strong CD is expected, but to date not observed, in the excitation of different multiplet states of the core hole, especially considering that the excitation of states with smaller angular momenta than the intermediate state is only possible for counterrotating, but forbidden for corotating pulses. Finally, observing the angular distribution of a two-color ATI signal at high photon energies will reveal the to date unexplored sensitivity of this nonlinear two-photon process to nondipole effects (Fig. 23), which become more and more relevant for increasing momentum of the outgoing photoelectron.

With different partial electron waves involved in the ionization process, their relative amplitude will also determine the influence of nondipole contributions. The theoretical treatment of this particular aspect has already been developed [192], but experimental verification is still lacking, due to the challenging requirement of the simultaneous need for high-intensity and high-energy resolution at short

wavelengths. To this respect, double core hole ionization on atoms has been recently observed at the European XFEL using monochromatized beam with a resolution E/DE > 2000 [193] demonstrating that the fast technological advances will make feasible the realization of these above discussed theoretical predictions.

E. Ultrafast dichroic phenomena explored with COLTRIMS reaction microscopes

Till Jahnke and Reinhard Dörner.

Employing x-ray-driven photoionization for the determination of structural properties of atoms or molecules has a longstanding history. Initially, these studies targeted mainly the electronic structure, for example, through photoelectron spectroscopy. It was later realized, that in case of molecules the emitted photoelectron contains information on the geometrical structure, as well. This information is encoded in the angular emission distribution of the photoelectron. The photoelectron wave is scattered by the molecular potential yielding distinct interference patterns that are directly connected to the shape of the molecule. This approach was first applied to molecules being absorbed on surfaces in the 1970s (see, e.g., Refs. [194,195] for a early reviews). It took until the late 1990s until single, isolated molecules in the gas phase were addressed in pioneering works [196,197]. Since then, in particular (coincident) imaging methods have proven to be able to measure these electron interference patterns of molecules in the gas phase and in the following we will focus on so-called COLTRIMS reaction microscopes [113,114,132] as devices for such studies.

In reaction microscopy, a well-localized, typically internally cold supersonic gas jet is crossed at right angle with an ionizing beam of photons (or other projectiles). As a reaction occurs, the charged reaction-fragments (electrons and ions) are then guided by weak electric and magnetic fields toward two time- and position-sensitive detectors. By measuring the flight time and the position of impact of each fragment in coincidences, the initial momentum vector of the detected particle can be reconstructed in an offline analysis. As momenta are measured, all derived quantities as kinetic energies and (laboratory-frame) emission angles are obtained, as well, and the coincidence measurement allows to explore relative quantities of several fragments (e.g., relative emission angles) in addition.

If (soft) x-rays are employed for a photoelectron diffraction measurement, the photoelectron wave is typically launched at a well localized site inside the molecule and the molecule is "illuminated from within" [198]. As the diffraction occurs in the body-fixed frame of the molecule, the random orientation of molecules in the gas phase poses a first experimental challenge. Accordingly, the molecules can either be actively aligned using IR-laser pulses [199], or the molecular orientation at the instant of ionization is deduced from a coincident measurement of ionic fragments that are ejected. The latter approach works if this fragmentation is rapid [200], which is often the case, if it is triggered, e.g., due to secondary ionization processes such as Auger decay or Auger cascades following the inner-shell photoionization. The momentum

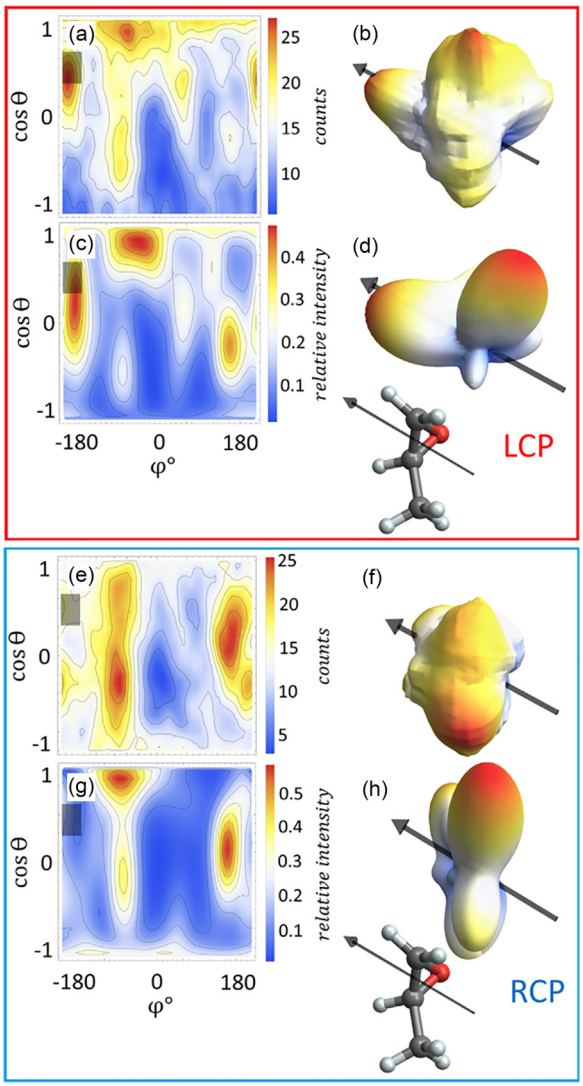

FIG. 24. Examples of measured (a), (b), (e), (f) and computed (c), (d), (g), (h) three-dimensional molecular-frame electron angular distributions using left circularly and right circularly polarized photons (top and bottom, respectively) for the ejection of the electron. The figure has been adapted and reprinted with permission from Ref. [201].

vector of the electrons, that are measured in coincidence with the momentum vector of the ionic fragments, can then be transformed into the molecular-frame yielding the three-dimensional photoelectron diffraction pattern. Examples of such patterns are shown in Fig. 24, which has been taken from Ref. [201]. In the context of this roadmap article, the following point is particularly noteworthy: As the photoelectron diffraction is sensitive to the molecular structure it is also sensitive to the handedness of this structure, i.e., it is enantiosensitive. In addition, if the photoelectron wave is launched by circularly polarized photons this enantiosensitivity is typically enhanced, since the photon imprints an angle-dependent phase onto the electron wave during its birth. It is the combination of the scattering by the three-dimensional molecular potential and this angle-dependent phase, that causes finally the PECD introduced already in Sec. III A of this article.

PECD is a light-helicity dependent forward/backward asymmetry of the photoelectron flux, that survives even an integration over molecular orientation. This property makes it directly accessible by means of angle-resolved electron spectroscopy. In most cases, however (when ejecting the electron from an achiral orbital), the scattering of the electron wave by the molecular potential is the mechanism underlying PECD. Accordingly, the strength of the PECD-signal increases already drastically if the molecular orientation is only partially fixed in the laboratory-frame [202] and PECD in some cases becomes a 100% effect if the chiral molecule is fully fixed in space [201]. A corresponding example is shown in Fig. 33 in Sec. IV D. There, the heatmap on the left shows the measured PECD, the one one the right the results from theoretical predictions. The molecule is aligned with respect to the photon propagation direction as depicted by the sketches on the right.

PECD and photoelectron diffraction measured in a COLTRIMS reaction microscope has grown into a much-used powerful technique during the past decade and much of the underlying physics of these effects can be considered understood today. With the advent of circularly polarized XFEL radiation, the field will most obviously target the time domain in the near future and time-resolved studies of transient chiral structures are a first target of choice. Related time-resolved (pump-probe) studies using linearly polarized XFEL light are already underway. These cannot observe PECD as such for obvious reasons, but yet image the underlying three-dimensional molecular geometry using photoelectron diffraction or Coulomb explosion imaging [13,133]. As this roadmap article addresses future opportunities for polarization-controlled free-electron laser light, we want to speculate about two other possible, yet less studied chiral effects. These do not emerge from the chiral molecular structure directly, but may occur due to a (transient) chiral structure in the molecular (or even atomic) electron cloud.

As a first example we refer to Fig. 25 which has been taken from Ref. [203]. It shows a chiral electron cloud of an excited H atom. In this case of a centrosymmetric potential, this state is formed by the superposition of degenerate higher angular momentum states. In general there are two classes of such states: those where the square of the wave function, i.e., the probability density, is a chiral object and secondly those where the square of the wave function is achiral, but the phase structure of the wave function makes it a chiral object. As the derivative of the phase of the wave function is related to the flux, this corresponds to a chiral nature of electron flux and thus a chiral momentum distribution. A most simple example would be a state $l = 1$, $m = +1$ which has a ring current and is prochiral. Real chiral distributions can be created by excitation of K-shell electrons by circularly polarized photons in a chiral molecule. Most probably, this can also be achieved in achiral molecules if the molecule is fixed in space under distinct angles with respect to the light propagation. Such transient chiral electron distributions are fascinating objects for time-resolved ionization experiments at XFELs being capable of providing circularly polarized light. At low photon energies these have been studied already in pioneering work (where the process has been termed "photoelectron excitation circular dichroism") using high harmonic laser light sources [204]. We

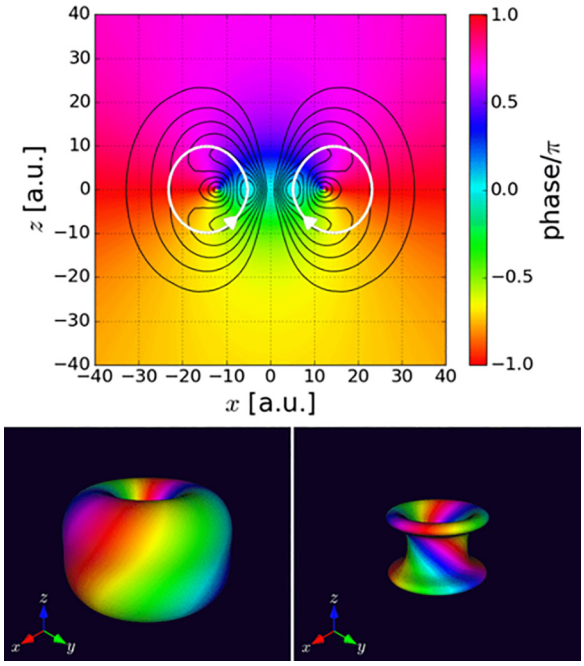

FIG. 25. Example for a chiral hydrogenic wave function χ in form of a cut along $y = 0$ (top) and isosurfaces for $|\chi| = 0.003$ a.u. and $|\chi| = 0.005$ a.u., please refer to the original publication for details. The wave function's phase is indicated by the colors. The white circles in the top figure indicate the direction of the probability current in the plane $y = 0$. The figure has been adapted and reprinted with permission from Ref. [203].

envision two tools to interrogate such chiral electronic wave functions. The first is direct photoionization of the orbital carrying the chiral flux. This is best done with high-energy photons. When the photoelectron wavelength is short enough, the final continuum state of electron is well described within the Born approximation, which entails that one neglects the scattering of the photoelectron wave by the potential of the molecular ion after its emission. As shown in Ref. [205] under these circumstances the photoelectron angular distribution maps directly the initial state momentum distribution of the bound electron. Thus, one can hope to obtain a fingerprint of the chiral phase structure (and thus the chiral current) in angular emission distributions of high-energy electrons. Alternatively, one can envision to not eject the chiral electron itself but a different (e.g., K-shell) electron instead. This photoelectron wave then probes the chiral electron cloud, i.e., similar to photoelectron diffraction this will probe the molecular potential created by the excited electron. Such scattering probes the potential which itself is determined by the chiral electron density. Thus, we have two tools at hand which probe different aspects of the chiral electron cloud: scattering of electrons from K-orbitals which senses chiral densities of the cloud, and ejecting the electron from the chiral orbital itself which probes the chiral flux rather than the density.

All of this promises a rich harvest for time-resolved circularly polarized x-ray photoemission studies of transient chiral objects in the molecular frame by coincidence techniques. The timescales of interest spans from the attosecond regime expected for changes in the chiral electron cloud to the

femto- to picosecond regime on which the chiral molecular structure evolves.

F. Ultrafast chirality at FELs: New enantiosensitive observables, site-specific, PECD and charge-directed reactivity

Francesca Calegari, Olga Smirnova, and Caterina Vozzi.

Conceptually new *local* approaches to inducing, probing and controlling chirality with light are known as the electric dipole revolution in chiral measurements [206,207]. In contrast to traditional methods such as absorption CD and optical rotation, these new methods do not rely on the interaction with the magnetic field component of the light wave but instead use exclusively electric dipole transitions to excite and probe dynamics in electronic, vibronic or rotational states of chiral molecules via detection of emitted photons or photoelectrons.

One of the most advanced in this family of methods is PECD. Predicted in Refs. [208,209], and first observed in Ref. [107], PECD constitutes the emergence of enantiosensitive photoelectron current upon one-photon ionization of chiral molecules by circularly polarized light (see, e.g., Refs. [210,211]). Opportunities for ultrafast chiral measurements utilizing PECD emerged after recent works demonstrating few-photon [212–222] and strong-field [223] analogues of PECD using femtosecond pulses, leading to time-resolved PECD [108,224,225], photoexcitation circular dichroism in bound molecular states (PXCD) [204], two-color PECD [226–229], and even detection of attosecond (1 as = 0.001 fs) photoionization delays from chiral molecules [230].

FELs with polarization control add site specificity to these measurement protocols and thus enable local imaging and control of chiral molecules, which is highly desirable for applications in chiral analytics but is currently missing. For example, a large chiral molecule, such as a peptide, can contain smaller units, such as amino acids, of different chirality. Resolving the handedness of such units and detecting their spatial structure is an important challenge.

1. Geometric magnetism and synthetic chiral light at FELs

For two decades PECD stood out as *one-of-a-kind* effect with record enantiosensitivity in the range of tens of percents, representing a "golden standard" for chiral detection. Recently it has been shown that PECD is only a "tip of the iceberg": new classes of observables with similarly high enantiosensitivity united by the concept of geometric fields [231] have been predicted. What is more, these observables are unique messengers of chiral currents in electronic, vibrational, rotational or spin degree of freedom, because they only exist if an arrow of time is introduced into the system. One example of such a new observable is enantiosensitive molecular orientation after photoionization by circularly polarized light (PI-MOCD, molecular orientation circular dichroism by photoionization) [231].

Physically, the chiral molecular geometry together with broken time-reversal symmetry via excitation of currents of any kind leads to the emergence of the Berry curvature—similar to the one operating in solids and underlying, e.g., the quantum Hall effect. In chiral molecules it emerges due to the excitation of chiral electronic current, the dependence of this current on the orientation of the laser field with respect to the molecule [232], and is defined in the space of light field orientations (in contrast to the Berry curvature in solids where its is defined in the space of crystal momenta). The curvature $\vec{\Omega}$ can be formalized as $\vec{\Omega} = i\langle\vec{\nabla}_{\vec{E}}\psi_{\rm el}(\vec{E})| \times |\vec{\nabla}_{\vec{E}}\psi_{\rm el}(\vec{E})\rangle$, where $\psi_{\rm el}(\vec{E})$ is the laser-driven electronic wave function in the molecular frame and $\vec{E}$ is direction of the light field polarization in the molecular frame. The gradient $\vec{\nabla}_{\vec{E}}$ of the wave function with respect to the light field polarization vector highlights that the curvature is dictated by the changes in electronic dynamics in response to changes in the orientation of the light field with respect to the molecule [232]. The curvature leads to new properties emerging in randomly oriented molecules after the interaction with light, such as, e.g., ensemble-averaged permanent dipoles proportional to the Berry curvature and oriented in opposite directions in left and right enantiomers. This effect opens the opportunity to control the direction and degree of molecular orientation by controlling electronic or vibronic molecular excitations.

FEL pulses offer an exciting opportunity to induce PI-MOCD in randomly oriented molecules via core excitation with few-femtosecond or attosecond x-ray pulses. In contrast to excitations in valence shells, localized site-specific core excitation could initiate currents from different locations inside the molecule and may result in more accurate and versatile control of the Berry curvature. This excitation can then be used by a delayed probe pulse with a much lower carrier frequency to achieve enantiosensitive reactivity directed by the excited charge dynamics.

As a result of the excitation by an ultrashort FEL pump pulse, the left enantiomer of a chiral molecule, when photoionized by a time-delayed circularly polarized probe pulse, orients itself in such a way that the Berry curvature generated by the pump-excited electronic current points in the positive direction of **k**, **k** being the propagation vector of the ionizing probe pulse. In contrast to the left enantiomer, the right enantiomer orients itself in the exactly opposite direction. Fragmentation of an oriented molecule will lead to enantiosensitive fragment distributions, such that chemically identical fragments originating from opposite enantiomers will fly in opposite directions of the light propagation axis. Thus, we can control *vectorial* properties of molecules with an efficiency comparable to the "golden standard" of the PECD.

The concept of geometric fields also predicts new geometry-driven *scalar* observables, such as photoionization or photoexcitation yields, which are proportional to the Berry phase. None of these geometry-driven observables has been observed so far, but they promise spectacular applications, such as efficient and robust control of enantiosensitive chemical reactions. The efficiency stems from the electric-dipole nature of these new observables, while robustness may come from their purely geometric origin. For FELs, this opportunity translates into enabling local enantiosensitive imaging. For example, the challenge of enantiodiscriminating small chiral units embedded in a large molecule, such as amino acids attached to peptides, could be addressed by efficient selective excitation of, say, left units.

Looking broadly, the polarization shaping at FELs could be extended toward creating new efficient schemes for chiral low-order nonlinear processes such as chiral sum-frequency

generation [233], nonlinear optical rotation [234] or chiral CARS in electric dipole approximation. Noncollinear or tightly focused FEL beams could be used to create synthetic chiral light [235] or chiral topological light [236] in the x-ray range. In contrast to standard chiral light, which uses the (nonlocal) spatial helix of circularly polarized light, synthetic chiral light encodes chirality in the temporal dimension and may allow higher enantiosensitivity at photoexcitation and X-CARS.

2. *Chiral femtochemistry probed by core-level photoemission*

Studies of ultrafast structural dynamics in chiral molecules can provide insights into fundamental questions in chiral chemical and physical processes, from the role of chirality in chemical reactions to its influence on biological processes. The development of ultrafast x-ray FELs enables such studies and opens avenues for understanding the chiral activity of photoexcited states.

In this respect, time-resolved x-ray photoelectron spectroscopy (TR-XPS) is a powerful approach for the investigation of photochemistry in molecules providing information about the local charge distribution with atomic specificity in the electronic ground states. Furthermore, the localization of core orbitals makes this approach site-selective. Since the ionization potential (IP) gives the difference between the neutral state and the core-ionized state for a specific atom in the molecule, the chemical shift of the IP gives information on the charged environment near the specific probed atom. In contrast to standard XPS, TR-XPS enables access to nonequilibrium charge distribution and ultrafast relaxation pathways with chemical selectivity. A recent pioneering experiment performed at Flash2 demonstrated the capability to capture the UV-excited dynamics of 2-thiouracil and deduced charge distribution changes in excited molecules in the framework of a potential model [237]. The photoexcitation can trigger a change in chemical shifts, which can be used to distinguish between the contributions of the different atoms of the same species in the molecule, thus enhancing the site specificity of the technique. This approach is indeed relevant for the study of chiral dynamics since the most sensitive technique for the study of these dynamics is time-resolved photoelectron circular dichroism (TR-PECD).

The availability of circularly polarized femtosecond pulses in the soft x-ray range at FELs enabled the extension of TR-PECD to core-level photoemission for chemical-specific and site-selective probing of the chiral electronic structure and its relaxation dynamics. Recently, Ilchen *et al.* reported a chemical-specific investigation of the dissociating trifluoromethyloxirane chiral cation ($C_3H_3F_3O^+$) [110] performed with an x-ray pump and x-ray probe at the LCLS-XFEL at SLAC. They measured PECD at the binding energy corresponding to the fluorine K-edge during the molecular dissociation dynamics, however, the contribution of the three fluorine atoms in this molecule could not be distinguished.

Another experiment performed at FERMI investigated structural dynamics in fenchone ($C_{10}H_{16}O$) induced by a UV pump and probed by core-level TR-PECD at the carbon K-edge [111]. Core-level probing was used to study the electronic scattering potential of the photoexcited molecules.

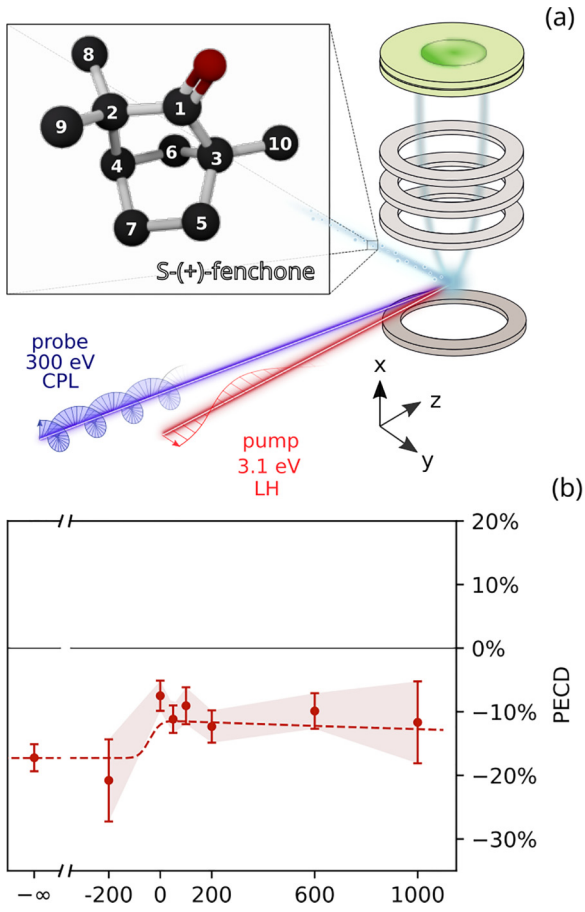

FIG. 26. (a) Experimental setup for TR-PECD. The circularly polarized XUV probe and the visible pump with linear horizontal polarization are focused quasicollinearly in the molecular beam of S-(+)-fenchone enantiomers. The inset shows a 3D representation of the S-(+)-fenchone, where only carbon (black) and oxygen (red) atoms are shown, while hydrogen atoms are hidden for the sake of clarity. (b) Measured TR-PECD at 292.53 eV, shown with violet dots along with the error bars. The figure has been adapted from Ref. [111].

The delocalized excitation to the 3s Rydberg state has been shown to affect the PECD of the carbon 1s photoelectrons. Thanks to a substantial chemical shift in the carbonyl group and an additional chemical shift caused by the excitation, the experiment was able to distinguish the chiral signal from C(1s) = O and its two neighboring carbons from the rest of the carbon atoms by detecting the photoelectron dichroism at different pump-probe delays and photoelectron kinetic energies. A sketch of the experimental setup is shown in Fig. 26(a) and the temporal evolution of the measured PECD at 292 eV is shown in Fig. 26(b).

The combination of the experimental results with theoretical calculations was important for understanding the role of the different carbon atoms in the ground state relative to the contribution to the total PECD signal coming from the excited molecule.

These results represent the first step toward chemical, site-specific, enantiosensitive observations of the electronic and structural dynamics of photoexcited chiral molecules. Such

studies will greatly benefit from the availability of high repetition rate x-ray FELs with circularly polarized ultrafast pulses in the future.

3. Enantioselective charge-directed reactivity

Another fascinating route in the ultrafast control of the chiroptical response of molecules is offered by charge migration [238–240] and charge-directed reactivity [241–243]. Charge migration occurs after sudden ionization or excitation of a molecule by a broadband laser pulse and may involve processes driven by electron-electron correlations [238–240]. The superposition of electronic states created by such excitation leads to nonstationary charge density distribution that typically oscillates along the molecular backbone on a timescale from a few tens of attoseconds to a few femtoseconds before the nuclei have had a chance to move. In turn, charge-directed reactivity implies chemical change, i.e., the dynamics of the nuclei following as a result of such attosecond electron dynamics. Charge migration has been theoretically predicted [238–240,242,243] and subsequently experimentally demonstrated to occur in aromatic amino acids [244,245] and nucleobases [246] after prompt ionization by an XUV attosecond pulse. Recently, charge migration has been observed in inner-valence ionized molecules exploiting a two-color attosecond time-resolved approach at the LCLS free-electron laser [247]. The role of the nuclear dynamics in the dephasing and the revival of these coherent electronic oscillations has been studied by soft x-ray attosecond transient absorption spectroscopy of strong-field excited molecules [248].

In this context, there has been an increasing interest in understanding the impact of coherent electron dynamics on the chiral response of molecules. Local chirality is a property of both the nuclear and electronic structure. Where the nuclei create a chiral structure, the electron density distribution is expected to follow suit. However, one may ask what happens to the chiroptical response, i.e., the interaction with chiral light, when this charge density distribution is no longer static. Is the CD affected by the electronic current originated along the molecular backbone? Is it possible to switch the sign of the CD in the same enantiomer by exploiting its electron dynamics? Preliminary work has been conducted both theoretically and experimentally to address these fundamental questions.

Enantiosensitive charge migration and enantiosensitive charge-directed reactivity are the next challenging milestones, which require efficient excitation of attosecond electron dynamics in chiral molecules as well as enantiosensitive detection of its impact on the dynamics of the nuclei. The recently predicted PI-MOCD [231] resulting upon excitation of nonequilibrium charge distribution in chiral molecules is an example of such protocol. The first step—charge migration in a neutral chiral molecule—has been detected in a very recent experiment [249] preparing a coherent superposition of Rydberg states via broadband UV-light excitation of the chiral molecule methyl-lactate and observing its periodic evolution on a few-femtosecond timescale by TR-PECD. Chiral currents observed in this experiment can lead to PI-MOCD: molecules whose orientation is such that the current behaves near in-plane and in-phase with the circularly polarized electric field of the ionizing probe pulse will be preferentially ionized, leading to an oriented ensemble of ions, with the left and right enantiomers oriented in opposite directions. Detecting the direction of the fragments ejection (forward or backward with respect to the propagation of the circularly polarized ionizing pulse) provides an enantiosensitive observable. Even more strikingly, by adjusting the delay between the pump pulse preparing the electronic coherences and the probe pulse photoionizing the molecule, one can control the direction of the fragments ejection without changing enantiomer, therefore opening a route toward the implementation of the enantiosensitive charge directed reactivity.

The use of attosecond x-ray free-electron lasers offers new avenues for exploring these phenomena. In particular, employing a two-color scheme, charge migration could be selectively activated via single or double core-hole ionization and the resulting chiral currents could be probed with attosecond time resolution, while the Auger-Meitner decay occurs, and with site and stereo selectivity at the k-edge of the molecular chiral center. Circularly polarized attosecond FEL pulses are key for this investigation, since probing or pumping with circularly polarized light would offer the possibility to explore the attosecond TR- PECD or PXCD response, respectively. In the PXCD geometry, the selective chiral excitation of the electronic currents would allow the control of the chemical reactivity of the molecule to be achieved at the electron timescale.

G. Interplay between photonic spin and orbital angular momentum as a tool for new spectroscopies and for tailoring matter properties at the nanoscale

Giovanni De Ninno, Jonas Wätzel, and Jamal Berakdar

Photons have a fixed spin (SAM) and an unbounded orbital (OAM) angular momentum. While the former is related to light polarization, the latter is manifested in a particular spatial structure of the orbital part of the electric field. The expectation value of the optical OAM with respect to the propagation axis of the light wave is $\hbar\ell$, where ℓ is an integer and indicates the number of windings in a wavelength [49]. The corresponding nonuniform spatial texture of the photonic vector potential can act as a source for additional scattering during light-matter interaction. This may lead to new phenomena such as the transfer of optical OAM to charges as well as the possibility of spatially resolved control of the light-matter interaction below the optical diffraction limit. The interaction with OAM results in electronic transitions beyond the dipolar propensity rules, as they occur during photoionization. The structured-light-induced generation of unidirectional charge current loops with an associated orbital magnetic moment has been demonstrated [250–253], as well as the production of skyrmionic defects [254] with potential applications in nanoscale magnetic memory devices. A particularly useful setup is the combination of XUV with IR laser pulses simultaneously acting on matter. The benefit is that by varying the beams' focusing, the SAM, and the OAM transfer to matter can be spatiotemporally controlled [250,251]. Generally, technical advances enabled new ways for material characterization techniques such as OAM dichroism [250,253], OAM ptychography [255], and stimulated emission depletion-like microscopy [256]. Technically, ultrashort, high-intensity XUV or x-ray sources are needed

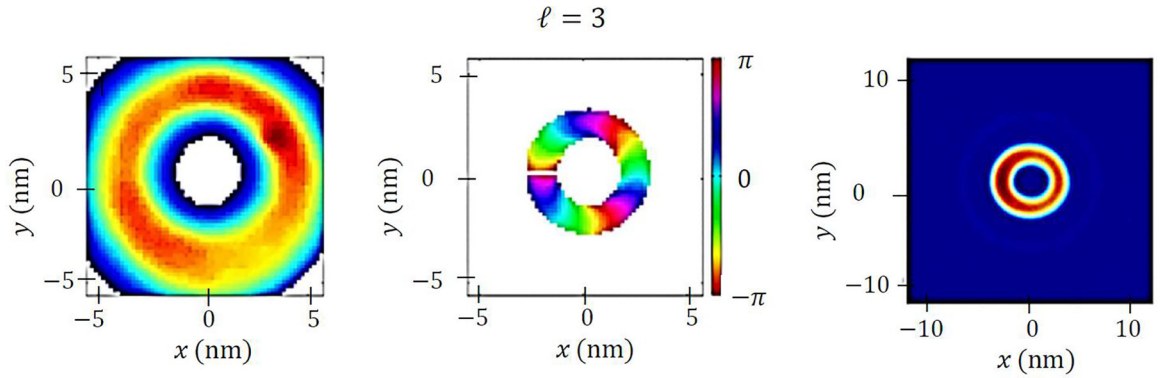

FIG. 27. Measured far-field intensity (left column) and phase (middle column), and the intensity distribution in the focal plane (right column) for ZPs with charge $l = 3$. The figure has been adapted from Ref. [50].

that are capable of producing vortex beams. In contrast to optical vortex generation in the visible and infrared (IR) spectral regions, where such beams have been successfully used in a wide array of applications ranging from particle manipulation [257,258] and detection of spinning objects [259,260] to optical communications [261] and super-resolution imaging [262], the generation of intense XUV or x-ray vortices remains a challenging task. Recently, two groups reported the production of XUV beams with tunable topological charge using high-harmonic generation in a wave-mixing setup [263,264]. In Ref. [265], significant experimental progress was made toward plasma-based vortex generation, which shows promise for producing intense harmonics of the driving laser with adjustable OAM. However, the current performance of such tabletop systems in terms of the intensity of the generated XUV light is orders of magnitude lower compared to the new generation of accelerator-based sources such as FELs, and may not be sufficient to perform some of the proposed experiments. Therefore, several schemes have been studied for producing optical vortices at FELs [266,267]. At the FERMI FEL, two methods are currently used for generating intense XUV beams carrying OAM [50]. The first one takes advantage of the vortex nature of harmonics emitted in a helical undulator [268], allowing to obtain intense, femtosecond, coherent XUV vortices. The second technique relies on the use of aspiral zone plate, which is placed directly into the FEL beam path. The setup produces a focused, micron-sized, high-intensity optical vortex without requiring extensive modifications of the FEL beamline; see Fig. 27.

The distinctive way in which the photon spin dictates the electron motion upon light–matter interaction is the basis for numerous well-established spectroscopies. By contrast, imprinting OAM on a matter wave, specifically on a propagating electron, is generally considered very challenging and the anticipated effect undetectable. In Ref. [269], the authors provided evidence of OAM-dependent absorption of light by a bound electron. Recently, two experiments have been carried out at the low density matter beam line [250,251] of the FERMI FEL, on a gas-phase sample. In these experiments, the interplay between an IR laser pulses with OAM and a circularly polarized XUV FEL pulse allowed to demonstrate that: (a) OAM can be imprinted coherently onto a propagating electron wave [250]; (b) an optical vortex can induce orbital magnetization at the nanoscale [251]. The obtained results are summarized below. In Ref. [250], using extreme XUV radiation from the FERMI FEL, electrons in a He gas cell are elevated to just above the single-ionization threshold by one photon. During this process an intense infrared laser field is present (Fig. 28).

The FEL beam has a fixed (right-handed) circular polarization and the IR field has an orbital phase corresponding to a

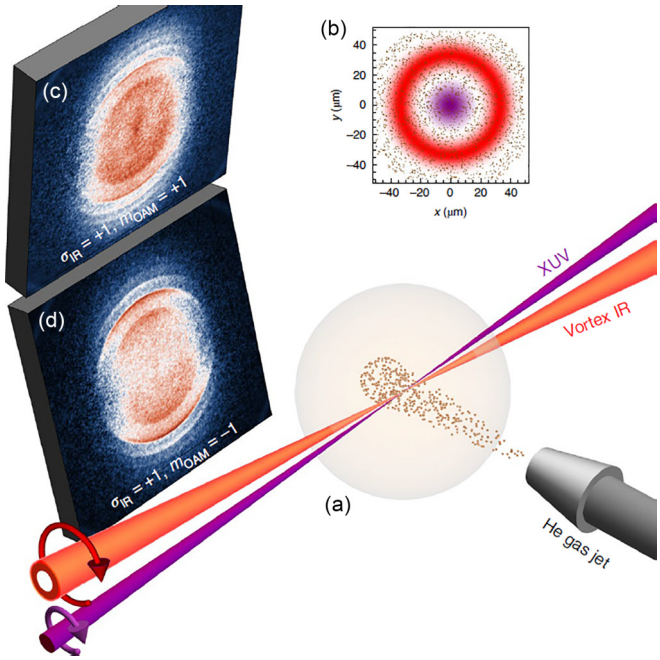

FIG. 28. Setup demonstrating the OAM transfer to a photoelectron. (a) Two colinearly propagating lasers (XUV and IR vortex field carrying OAM) interact with a Helium gas cell. (b) A cross sectional view on the intensity distributions: violet dot (red circle) is the XUV (IR) laser intensity profile. (c) Measured photoionization cross section (DCS) for the laser setup with an IR field carrying OAM of $+1\hbar$. (d) Same as panel (c) for an IR field with OAM of $-1\hbar$. The different rings in the cross section belong to different "sidebands" caused by IR multiphoton processes. All measurements and parameters of the XUV laser field and the polarization state of the IR field are kept the same. The figure has been adapted from Ref. [250].

well-defined OAM with respect to the propagation direction. The question of concern is whether it is possible to observe a vortex-dependent OAM dichroic signal (meaning a dependence of the ionization probability on the sign of the OAM), even though the atoms are randomly distributed across the laser spot of the OAM-carrying beam. This would be surprising: The atomic wave function is extremely localized on the scale of the OAM beam's waist [Fig. 28(b)]. Off-axis atoms experience the infrared laser field as an ordinary Gaussian beam and atoms close to the optical axis, where the OAM is well defined, experience a vanishingly small field. Besides, the fraction of near-axis atoms is small. Although the transfer of optical OAM to photoelectrons seems unlikely, if it happens, then it should involve a new type of nondipole transition, related to the OAM-carrying vector potential of the IR field. To clarify experimentally the above issue, atoms are irradiated with XUV beam copropagating with an infrared laser with adjustable right- or left-handed circular polarization, and variable OAM $l = \pm 1$. The two beams are focused and intersect a gas jet of He atoms in a vacuum chamber equipped with a velocity map imaging (VMI) spectrometer [251]. The velocity distribution of electrons produced in the interaction volume is projected onto a two-dimensional (2D) imaging detector parallel to the optical axis of both beams. For sufficiently high infrared intensities, the resulting photoelectron spectra [Figs. 28(c) and 28(d)] show a main band, corresponding to direct (XUV-induced) photoemission, together with a series of weaker rings, called sidebands, whose radius increment (decrement) represents the energy acquired (lost) by the photoemitted electrons upon absorption (emission) of one or more infrared photons. All bands depend on the polar angle at which photoelectrons are emitted. They reflect the interplay between XUV and optical fields during the photoionization process, providing information on the transfer of light properties, for example, angular momentum, to matter. When the two beams are circularly polarized and $l = 0$, there is a few-percent difference in the angular electron distributions for corotating and counterrotating XUV and infrared fields, resulting in a dichroic contrast in the range of 5–10% [163]. Now what happens if $l = \pm 1$. The two VMI spectra shown in Figs. 28(c) and 28(d) are obtained for fixed (right and left-handed) infrared circular polarization and alternate OAM ($+\hbar$ and $-\hbar$, respectively), with all other experimental conditions kept unchanged. The images demonstrate that different topological charges l result in qualitatively different photoelectron spectra, attesting a clear OAM-dependent dichroic effect. To clarify the underlying mechanism for the experimental evidence of the OAM-dependent dichroism, a first-principle theoretical model has been developed [250,251,253] that accounts for all nonlinear effects in light–matter interaction in a spatially structured vector potential. As in the experiment, the challenge is to account for the two vastly different length scales of the bound electrons and the spatial structuring of the vector potential. In addition to the full numerical solution of the time-dependent Schrödinger equation on a space-time-grid, perturbation theory [270,271] accounts for the coherent interaction of both lasers with the atoms, endorsing the following picture. The initially bound wave function is excited with one single XUV photon to just above the threshold inflating its extension. At this event in time and space, the electron wave packet starts scanning over the structured vector potential of the IR laser, acquiring information on its orbital phase. As shown in Ref. [250], the well-defined OAM of the IR laser implies that, in the azimuthal direction the phase gradient of the vector potential of the IR laser is constant. Hence, any atom at a certain radial distance from the optical axis experience the same phase gradient of the IR laser, regardless of the atoms' orientation, which explains the finite OAM dichroism, even after performing a thermal average over the ensemble of the atoms in the gas cell.

Having understood the nature of the OAM transfer to a random ensemble of atoms, one may think of orbitally magnetizing the distribution of the atoms. Thereby, the laser beams act as the bias field which orients each atom individually by driving a unidirectional charge current upon the transfer of SAM and OAM from the laser fields. The orbital magnetic moment associated with the charge current is robust since the excitations occur predominantly via a single-photon resonant excitation to Rydberg states which subsequently decays in absence of fields on the microsecond timescale. Interatomic interaction is negligible due to the low atom density. Obviously, such a method, if successful, can generate femtoseconds magnetic fields within micrometers. Even though the field strength averaged over a macroscopic scale might be very small, the local field can reach values useful for triggering local magnetization dynamics in nearby magnetically ordered material. To validate this scenario, experiments have been performed. For that, use has been made of a gas of He atoms. The spatiotemporal control of the excited magnetic moment was obtained by exciting atom's ground state to a Rydberg state with the XUV circularly polarized photon beam generated by FEL. The spatial extent of the generated Rydberg orbital is set by the XUV frequency. A second copropagating IR vortex pulse assists in generating the unidirectional current. Tuning the intensity ratio between the XUV and the IR pulses controls the cross-sectional area where the magnetic moments reside, allowing in this way for a nanoscale tuning of the generated magnetic fields with a resolution well below the diffraction limit of the IR laser. The magnetic field associated with the quantum mechanical current density $\mathbf{J}_\varphi$ is obtained from classical electrodynamics; see Fig. 29. $\mathbf{J}_\varphi$ itself is deduced from full *ab initio* quantum evolution of the initial state wave functions in the laser fields.

The proposed scheme is not restricted to He. Rydberg states are a generic feature of electronic compounds, and their photoexcitation does not require a symmetry breaking in the sample. For example, the approach can be applied to adsorbates such as rare gases that are physisorbed at magnetically active surfaces [272], allowing one to study the spatiotemporal material's magnetic response to the fields of the photogenerated magnetic moments. A further future development is the spatiotemporal modulation of the spin part (polarization) of orbitally structured laser electric fields. This would pave the way for the generation of new types of topological optical fields in the XUV regime with the prospect of new insights and applications, particularly to topological and vortex materials, as shown for superconductors [273]. Femtosecond polarization shaping of spatially homogeneous free-electron laser pulses has been demonstrated recently [274].

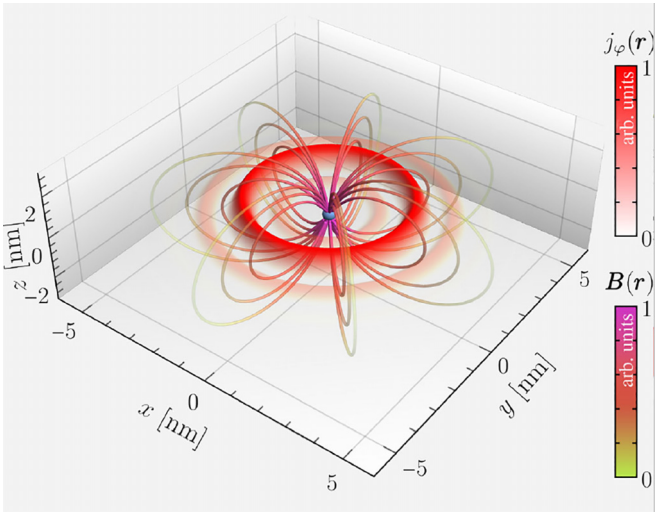

FIG. 29. Irradiating atoms by a copropagating circularly polarized XUV laser pulse and IR vortex field carrying OAM induces in a He atom a circular unidirectional charge Rydberg current density $j_\varphi(r)$. The current leads to a nanoscale localized, persistent magnetic field (B) around each atom. The figure has been adapted from Ref. [251].

H. Perspectives for stereochemistry in complex molecules

Sadia Bari and Lucas Schwob.

Amino acids, which are the building blocks of proteins, are all left-handed, while the sugars in DNA and RNA are right-handed (see also Sec. III C). Yet the origin of this homochirality of life still remains unsolved. CD studies exploit the chiral properties of biomolecules to reveal structural information [275,276]. The availability of commercial CD instruments covering the energy range from the far UV (190 nm) to the NIR (1600 nm) makes it easy to address different absorption bands and thus different structural aspects and molecular systems. Here we focus on the electronic CD where, for example, in the UV the absorption by DNA bases reveals their relative positions and thus the different conformational forms of DNA [276]. CD of proteins in the far-UV analyzes the fraction content of the secondary structures due to a strong π–π^* transition around 190 nm and a weaker but broader n–π^* transition between 210 and 220 nm in the peptide bond [275]. In the near UV the CD is dependent on the aromatic side chains and disulphide bonds and can give information about the tertiary structure of a protein. Synchrotrons allow the use of photon energies in the VUV with orders of magnitude higher photon fluxes for CD measurements than in commercial CD instruments, which compensates for the stronger absorption in the VUV region due to, e.g., air, buffer solutions, and salts, and generally improves the signal-to-noise ratio of the spectra significantly. The lower wavelengths down to 120 nm lead to the observation of more CD bands in biomolecules and therefore more conformational information. First measurements in the soft x-ray regime on amino-acids films show the feasibility of observation of x-ray natural absorption CD and pave the way together with theoretical calculations for a new local probe by the element and orbital specific transitions [277,278]. When combined with "near edge x-ray absorption fine structure" (NEXAFS) spectroscopy, a powerful tool for studying of the molecular electronics and geometric structure, it could provide additional information due to the fact that particular atoms or functional groups which have very similar x-ray absorption spectra may have different chiral properties [278].

Most biomolecular CD studies are done in the condensed phase and can be performed on molecular systems of any size and under various solvent and temperature conditions without the need for crystallization. In contrast to x-ray crystallography, CD allows obtaining additional conformational information, such as protein denaturation [279,280]. However, studies on complex isolated biomolecules in the gas phase are still lacking to decipher the purely intramolecular effects from the influences of the environment. These studies would allow careful chemical control, a bottom-up approach by gradually increasing the complexity of the systems, and easier comparison with theoretical models because intermolecular interactions can be excluded. Furthermore, in the gas phase, i.e., in vacuum, one would avoid the strong photoabsorptions into the environment mentioned above. Due to the lower target densities in the gas phase, CD measurements are performed using photoionization and measuring differences in the photoelectron emission rather than differences in absorption yields. For example, resonance-enhanced multiphoton ionization (REMPI) used in combination with mass spectrometry and table top UV lasers have detected a CD asymmetry up to almost 30% for small organic molecules [281]. Strong effects were as well observed for small organic molecules by PECD using a velocity map imaging spectrometer in the VUV [282] and a hemispherical analyzer in the soft x-ray regime [144]. That means that CD studies in the gas phase can reach asymmetries orders of magnitude higher than in conventional CD such that the applied techniques should be adapted for more complex biomolecules.

Studying in the gas phase larger, thermally fragile and nonvolatile, biologically relevant molecular systems requires the use of soft-ionization techniques. Electrospray ionization (ESI), developed in the 1980s by Nobel laureate John B. Fenn [283,284], is such a technique. It allows transferring the analyte molecule from the liquid phase to the gas phase by the production of a spray of charged microdroplets under a strong electric field. The desolvation of the droplets eventually produces a beam of the molecular ions of positive or negative charge depending on the solvent used and direction of the electric field. Working with ions enables the use of advanced ion-manipulation techniques employed in mass spectrometry (MS). These techniques are based on static and radio-frequency electric fields and enable ion beam guiding and focusing, mass and conformer selection of analyte ions, accumulation and trapping. ESI-MS has become popular, noteworthy in the analytical field, for its high sensitivity and low sample consumption (typical analyte solution concentration of nmol/L to umol/L).

As an analytic tool, mass spectrometry as such is blind to chirality. Being widely used for the analysis of complex biological samples and pharmaceutical drugs, much research effort has been made in the past 20 years to couple MS to chiral-selective methods [285]. MS has primarily been combined with separation tools such as liquid or gaseous

chromatographic techniques to differentiate enantiomers of chiral molecules prior to MS analysis. However, incompatibilities with the process of electrospray ionization are limiting the use of hyphenated MS techniques. In parallel, chiral analysis solely based on ESI-MS has been developed under the principle of the chiral recognition mechanisms. The methods rely on intricate ion-molecule reactions as well as on formation and/or dissociation processes of molecular complexes between a guest enantiomer and a host chiral selector, such as crown ethers [286].

As discussed thoroughly earlier, polarized light is a most straightforward and universal tool to probe chirality. In recent decades, ESI-MS has been successfully and routinely coupled with a variety of light sources, from tabletop lasers to synchrotron and free-electron lasers, to perform action-spectroscopy on gas-phase biomolecular ions in the IR, UV, VUV and soft x-ray energy ranges. To compensate for the low ion density produced by ESI sources, the molecular ions are exposed to light while stored in an ion trap. In this configuration, the overlap between the target ions and the photon beam is facilitated and the duration of the light exposure can be controlled to achieve a good signal-to-noise ratio. However, the detection of photoelectrons is impossible due to radio-frequency field in the ion trap and their close geometry.

Circular dichroism spectroscopy of mass-selected, trapped, biomolecular anions using ESI-MS and circularly polarized UV light has been first reported in 2020 by Daly *et al.* [287] (see Fig. 30). The authors investigated a series of negatively charged right- and left-handed DNA G-quadruplexes and G-duplexes (> 5000 Da) by means of electron photodetachment, which is a single-photon process thanks to the low electron detachment threshold in polyanions. The CD spectra is thus obtained by recording, as a function of the laser wavelength, the yield of $[M-nH]^{(n-1)-}$ from the reaction $[M-nH]^{n-}+h\nu \rightarrow [M-nH]^{(n-1)-}+e^-$. Overall, by comparing the solution and gas-phase CD spectra in the 200 to 300 nm wavelength range, they observed that the DNA polyanions have similar CD spectra in terms of sign and position of maximum and minimum intensity. Most importantly, their measured gas-phase CD spectra showed up to fivefold more intensity in the asymmetry factors than those measured in the solution phase. The authors concluded that the stacking pattern of the nucleobases is conserved in the gas phase and that the excited states responsible for CD in the UV range also trigger the photodetachment process.

While the latter study is based only on ion yields as an observable for the circular dichroism, it appears evident to the reader that measurement of the photoelectrons, such as the backward/forward direction, would bring unequivocal information on the CD, even in case when CD cannot be distinguished from the ion yields. As detailed thoroughly in the previous sections, PECD is mostly recorded in VMI-type instruments in crossed-beams configuration. Such experiments are extremely challenging for ions produced by an ESI source due to low target density available and complications inherent to the use of charged target molecules instead of neutral. UV PECD of electrosprayed molecular anions has been successfully reported for the first time by Krüger and Wietzel in 2021 [288]. Their proof-of-principle experiments were performed on deprotonated left- and right-handed glutamic acid and 3,4-dihydroxyphenylalanine (DOPA), using a circularly polarized UV laser at 355 nm. Like in the work by Daly *et al.* [287], electron photodetachment of anions requires a single UV photon, making it a more simple technique than REMPI-based CD, both in terms of technical requirement and theoretical description. Strong CD effects of up to 4.5% were measured in the forward–backward asymmetry in the photoelectron angular distribution for both molecules, although no CD effect could be identified from the ion yields only. This highlights once again the power of PECD spectroscopy to resolve chiral compounds.

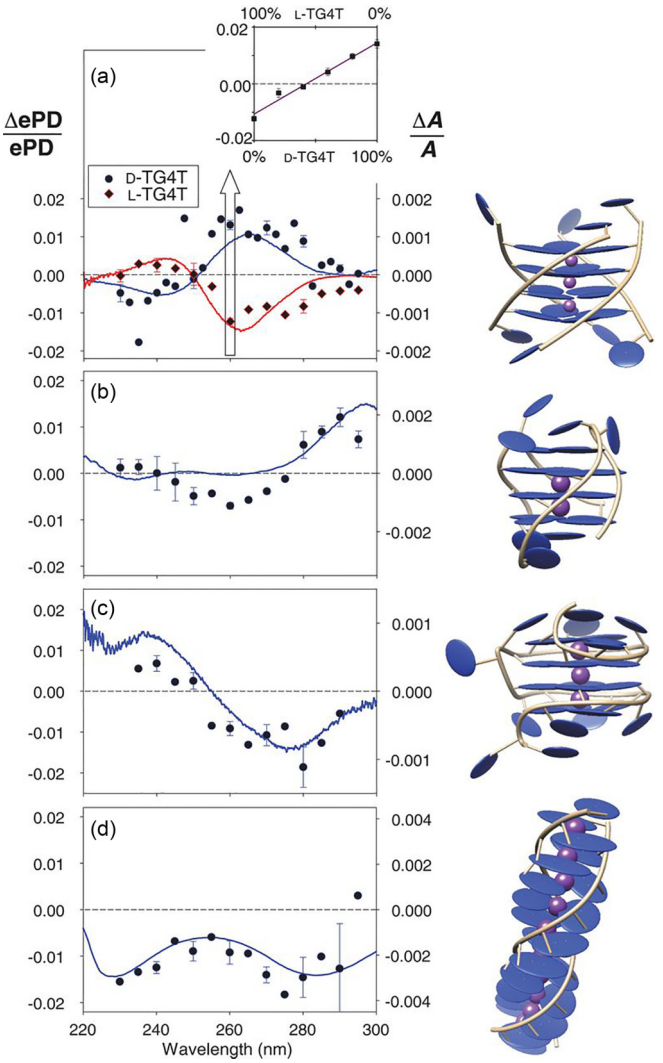

FIG. 30. Gas-phase circular dichroism spectra (ΔePD/ePD) compared to solution-phase spectra (ΔA/A). Symbols and lines denote gas-phase and solution-phase CD data, respectively. (a) Right-handed D– and left-handed L–TG4T ($([(TGGGGT)_4\cdot(NH_4^+)_3]^{5-}$) with inset showing CD at 260 nm for different ratio of D–TG4T and L–TG4T. (b)–(d) CD spectra for the antiparallel G-quadruplex $5YEY^{5-}$ (b), left-handed G-quadruplex $ZG4^{6-}$ (c), and G-duplex $GAgG^{5-}$ (d). The figure has been reprinted with permission from Ref. [287].

Overall, circularly polarized light-based chiral analysis of gas-phase complex biomolecules produced by soft ionization

source is an emerging field based on well known experimental tools. In pioneering experiments using electron photodetachment of anions, Daly *et al.* [287] and Krüger and Wietzel [288] paved the way for CD spectroscopy of electrosprayed molecules using UV lasers. This work has now to be extended to more systems and also to cations, for which a single UV photon is not sufficient to induce photoionization. As was shown for the extensively studied fenchone molecule, extending PECD in the VUV energy range [289] and even in the soft x-ray regime [143,144] allows reaching very high (up to 20%) asymmetry factors. Thus, by interrogating chirality of large gas-phase biomolecules in such an energy range, one would benefit from stronger CD effects in addition to overcoming the limit of UV-induced electron photodetachment. Especially due to the low ion density available with ESI sources, highly brillant x-ray sources are needed. XFELs would therefore be of prime importance to extend the capabilities of gas-phase CD spectroscopy. Finally, biomolecular chirality studies using polarized soft x-rays would profit from the high absorption site selectivity of soft x-ray photons, which in the form of ultrashort pulses would enable dynamical investigation of structural and chiral properties.

IV. THEORETICAL PERSPECTIVES FOR POLARIZATION-CONTROLLED FELS

This section is devoted to selected theoretical aspects of the topic. We will not attempt to provide a comprehensive summary of all the tools that are currently available, the ideas behind them, or a discussion of their strengths and (often severe) limitations. Instead, we will first illustrate the current state-of-the art by reporting a few selected benchmark studies within the scope of the topical orientation of this roadmap.

We will start with the popular single-active-electron (SAE) model to solve the time-dependent Schrödinger equation (TDSE). This model is, of course, the ideal tool for truly one-electron targets such as atomic hydrogen or the He^+ ion. It can also be expected to be successful for quasi-one-electron systems such as alkali-like atoms or ions with an appropriate core potential, as long as all the processes of interest only involve the valence electron. One example of the latter are recent studies involving optical lasers [290–292]. Nevertheless, the SAE approach has been used extensively for helium (e.g., Ref. [293]) and even more complex targets such as the heavier noble gases neon [294] or argon [295]. While none of these studies employed undulator-based polarized XFEL radiation, increasing the XUV intensity using the latter may open up additional possibilities for studying nonlinear phenomena also in asymmetric processes.

After presenting one undulator-based circular-dichroism study, we will discuss selected already available approaches that go beyond the SAE model, mostly for more complex atoms and relatively small molecules. Additional subsections are then devoted to observations that have become possible by polarization-based XFEL radiation, but whose theoretical description will require the development of new theoretical and computational tools due to the complexity of the targets (large molecules) involved.

A. Single-active-electron approximation

Klaus Bartschat and Nicolas Douguet.

At the fully quantum-mechanical level, the simplest approach that starts with the TDSE is the so-called "SAE approximation." As the name indicates, only one electron in the target is considered to be affected by the laser field. Even without the field, the interaction of this electron with the nucleus and any other electron is only treated approximately. Except for atomic hydrogen, He^+, and other true one-electron systems, therefore, the active electron is assumed to move in some average, usually spherically symmetric, field that is made up by both the nucleus and the other electrons. The pure (pointlike nucleus) nonrelativistic Coulomb problem for this setup can, indeed, be solved numerically with very high accuracy, although the choice of laser parameters can still make the problem challenging. Furthermore, currently available experimental techniques involving XFELs are not sufficiently sensitive to require accounting for very small effects that, for example, should be considered in highly sophisticated atomic-structure calculations.

Moving on to helium as a two-electron target, it turns out that the SAE approach *might* (see next subsection for more sophisticated approaches) still be applied with some confidence to support many ongoing experimental investigations. This is due to the fact that the nonactive 1s electron is very tightly bound and often only acts as a spectator. Even though there is a significant difference between the Hartree-Fock 1s orbital for the ground state and the 1s orbital of He^+, which is a very good approximation for all the excited $1snℓ$ bound states of helium, does not seem to seriously affect the quality of SAE predictions. The most important aspect here is to represent the effect of the spectator electron by a suitably chosen potential. In reality, this potential would have a nonlocal component due to the exchange interaction, but in practice local terms to approximate exchange as well as core polarization and possibly even absorption effects have been quite successful.

The very same approach can be employed in particular to describe studies involving the valence electron of alkali atoms. In fact, the well-known spectra of these atoms allow the design of very appropriate potentials to be used in the SAE approach. Not surprisingly, therefore, the theoretical predictions are often in excellent agreement with experiment. In fact, if there is disagreement, then it may well be worth to check the experimental data even more thoroughly than it is done anyway.

Coming back to helium, it is very important to note that there are now highly sophisticated codes around (see further below) that can fully treat the interaction of both electrons with each other as well as the laser field. Hence, it is possible to determine with high confidence the range of applicability of the SAE approaches. In addition, true correlation effects involving, for example, autoionizing resonances, can be studied with these methods. This has, indeed, been used to image the time evolution of the famous Fano resonances [296–298]. Another interesting two-electron system is H^-, where correlation effects in the ground state are stronger than in helium, while no excited states exist at all. However, this target does not seem to be particularly suitable for FEL studies and hence will not be discussed further.

Moving on to even larger atomic targets, both SAE and fully correlated two-electron approaches are undoubtedly reaching their limits when it comes to the experimentally often favored heavy noble-gas targets Ne, Ar, Kr, and Xe. To begin with, the active electron is often the outer p-electron, although the slightly tighter bound s-electron in the same major shell can affect the outcome as well—even by just making the signal less clear and hence more difficult to interpret. The first challenge, of course, is to find suitable SAE potentials. There are well-known problems already when it comes to reproducing the standard photoionization cross section. Such problems, of course, would cast doubt on any SAE results in certain energy regions.

Next, the calculations need to be performed for individual magnetic sublevels. For linearly polarized laser light, the results for $m = \pm 1$ are related in a simple way. For example, the ionization probabilities starting from either one are the same due to the cylindrical symmetry of the scheme. However, they are different for the initial $m = 0$ sublevel, and hence the results have to be combined appropriately. When circularly or elliptically polarized beams are used, the situation is even more complicated. In this case, a thorough general description of the observables in terms of the relevant amplitudes needs to be developed as well.

Another challenge is the structure description of these targets. Even neon as the lightest of these species is not well described in pure *LS* coupling. As a result, instead of one $2p^5 4s$ state with a total electronic angular momentum $J = 1$ [namely, $(2p^5 4s)^1P_1$ in *LS* notation] being available as a stepping stone in an $\omega + 2\omega$ setup [294], a second one [usually labeled $(2p^5 4s)^3P_1$ in *LS* notation] could also be accessed. While it is possible to select one of the two by tuning the photon energy, this shows that the complexity increases substantially when the simplest and strictest selection rules are no longer applicable. Similar, even more complex, considerations need to be given to the $n_1 p^5 n_2 d$ configuration. And, finally, the fact that the target s- and d-orbitals are actually term-dependent further complicates the situation.

By carefully comparing predictions from perturbative calculations with a sophisticated target description and nonperturbative SAE calculations with a much simpler structure model, the similarities and remaining differences have been analyzed in a number of cases. Similarly, predictions from SAE models have occasionally been compared with those from two-electron codes and, for heavy noble gases, even all-electron approaches such as R-matrix (close-coupling) with time dependence [299]. Unfortunately, it is generally a major challenge to define a starting point that is sufficiently close to allow testing of a single aspect of these models. Even though this often cannot be done to full satisfaction, agreement between results obtained with vastly different methods can provide confidence in these predictions and subsequently be used as a basis for the interpretation of the experimental studies that these calculations are supposed to support.

One example of an undulator-based circular-dichroism study on a simple target is the experiment reported by Ilchen *et al.* [164]. A circularly polarized XUV pulse was applied to neutral helium in the $(1s^2)^1S$ state to ionize the target and, in the same step, the remaining electron in the $He^+(1s)$ ground state was excited to the $m = +1$ magnetic sublevel of the 3p state. This excited and oriented state was then ionized by a corotating or counterrotating near-infrared (NIR) field.

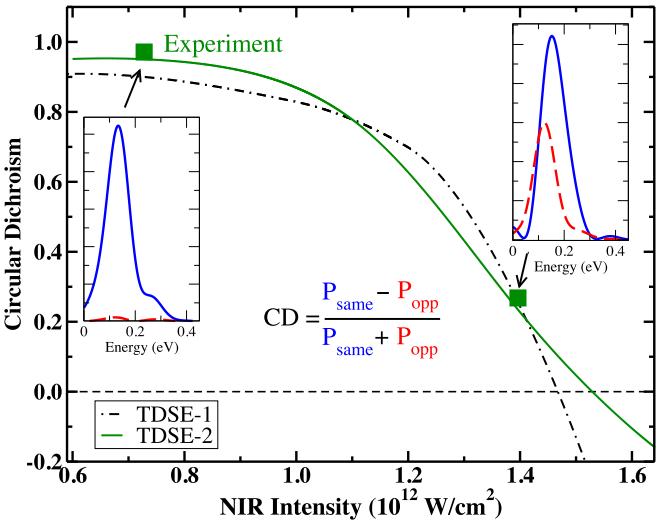

FIG. 31. Circular dichroism in the low-kinetic-energy peak as function of the NIR peak intensity for an XUV peak intensity of 1.0×10^{13} W/cm^2. The two experimental points are compared with predictions from two independent TDSE calculations (TDSE-1 [300], TDSE-2 [301]). The insets show the low-energy spectra from the TDSE-2 calculation for the two experimental cases. The figure has been adapted from Ref. [164].

Figure 31 shows the angle-integrated CD of the low-kinetic-energy peak at about 0.12 eV as a function of the NIR intensity. With increasing NIR intensity, the CD rapidly decreases and is predicted to even change sign at $I_{\mathrm{NIR}} \gtrsim 1.5 \times 10^{12}$ W/cm^2, i.e., ionization by counterrotating fields becomes more effective. This can be clearly seen in the very large differences in the predicted signals for the co- and counterrotating cases when the intensity is changed. Given that this is an ideal problem for a single-active-electron method (one can actually start with only the electron in the excited ionic state), it is not surprising that there was excellent agreement between experiment and theory, albeit the comparison at the time was limited to just two points.

The explanation for the strong dependence on the NIR intensity proposed by Ilchen *et al.* [164] was a different, helicity-dependent shift of the $He^+(3p, m = \pm 1)$ states due to the presence of the circularly polarized NIR field. This explanation was, indeed, confirmed later by Grum-Grzhimailo *et al.* [188]. Hence, even this apparently simple system, which can be used for a benchmark comparison between experiment and theory, carries surprises that justified further studies. Indeed, Wagner *et al.* [187] recently performed a follow-up experiment, in which a delay between the XUV and the NIR was introduced to prepare the initial He^+ state without the NIR already being present.

Photoionization of the simplest molecular ion, H_2^+, can be treated exactly, within the fixed-nuclei approximation, by using an SAE approach with elliptical coordinates. The most general methods usually employ compact B-splines or finite-element discrete variable representations (FEDVRs). In H_2^+, it is also possible to treat the nuclear motion explicitly, which provides an interesting case study. Molecular hydrogen is

another interesting case, as it can be treated accurately with a two-active-electrons method and thus represents a benchmark for theory for electron correlation in molecules.

Affine to the SAE method, where one electron is described in the field of a fixed potential, are those many-body methods for atomic and molecular ionization where both the initial bound state of the system and the final states in the continuum are restricted to a single-reference.

The XATOM code, an "integrated toolkit for x-ray and atomic physics" developed at CFEL by Sang-Kil Son and Robin Santra, is based on the Hartree-Fock-Slater method. The code is ideally suited to describe the generation of multiply charged ions generated by the interaction of intense XFEL radiation with atoms by means of sequential ionization mechanisms [10,11,302–304]. XATOM uses the static-exchange approximation to compute bound-state energies, ionization cross sections, Auger-decay rates, and fluorescence rates of all charged states involved. Even though XATOM neglects any single or multiple excitations from the ionic reference states, the mere process of creating vacancies in the target, as well as in the product of its subsequent Auger and radiative decays, gives rise to millions of configurations and a manyfold of more ionization paths. XATOM employs a Monte-Carlo method to sample the most relevant reaction paths in the rate equations for the system. The XMOLECULE code [305] is an extension to molecules of the Hartree-Fock-Slater methodology used in XATOM. It includes a classical treatment of nuclear motion, which is solved on-the-fly alongside the electron dynamics, in association with a Monte Carlo approach. XMOLECULE is capable of determining the yields of fragments that emerge from the interaction of a molecule with an intense XFEL pulse, and which can undergo multiple photoionization and nonradiative decay steps [12,12,306–308].

The E-POLYSCAT code [309,310], developed by Lucchese and coworkers, can describe the single-ionization electronic continuum of nonlinear molecules, within the fixed-nuclei and the static exchange approximation. The continuum functions are based on a single-center expansion. E-POLYSCAT has been applied to the calculation of electron-molecule scattering cross sections [308] and of multiphoton ionization observables of nonlinear molecules.

The TIRESIA B-spline density-function method is based on single-center [311–318] and polycenter expansions [319–324]. It has been used to predict the ionization yield in molecular strong-field ionization [325–327] and high-harmonic generation [328]. The method has also been applied to the calculation of one-photon vibrationally resolved core photoionization of molecules, which was instrumental to conclusively characterize the interference effects associated to two-center emissions and to intramolecular photoelectron scattering [329–335]. Furthermore, it has been applied to the study of charge-migration processes in biologically relevant molecules [244,245,336–338], where it has been key to interpret molecular fragmentation in attosecond pump-probe experiments.

OCTOPUS [339,340] is a general-purpose scientific program based on density-function theory (DFT) and time-dependent density-functional theory (TDDFT) [341] with a grid representation of the wave function. OCTOPUS has been applied to attosecond photoelectron spectroscopy [342], high-harmonic spectroscopy [343,344], and transient-absorption spectroscopy [345–348]. TDDFT has also been applied with a focus on tunnel ionization [349,350] and to track charge migration in midsize molecular ions [344,351,352]. While TDDFT approaches have enabled significant advances in attosecond science, they have limitations in handling strong correlation effects [353,354] and are still computationally expensive.

Single-active-electron methods reproduce the main features of strong-field ionization processes [326] and of those photoelectron spectroscopies were electronic correlation does not play a central role, such as in the case of the photoemission of high-energy electrons (several hundred eV) from core orbitals [332]. They are also useful for complex processes that lead to the complete fragmentation of a target [333]. When multiply excited states or the entanglement between fragments play a fundamental role, however, more complex approaches are required.

B. Going beyond the SAE

Luca Argenti, Klaus Bartschat, Nicolas Douguet, and Kathryn Hamilton.

As described above, the SAE approximation works well at energies low enough that the residual parent ion cannot be excited. It can also work well for the ionization of relatively uncorrelated core electrons, in atoms and molecules, when the released photoelectron is highly energetic. Indeed, in this case the interaction between different channels is negligible. Hence, the system can be described by a set of noninteracting single-active-electron effective potentials, one for each hole created in the single-configuration core of the target atom or molecule.

The SAE, however, cannot reproduce all the dynamical states of polyelectronic systems. In particular, ionization in energy regions close to the opening of an excited threshold entails the formation of multiply excited states and ionization channels with slow electrons, which are strongly coupled with each other, giving rise to Auger decay and inelastic scattering. These conditions are common in the ionization of atoms and molecules from the valence or inner- shells with VUV or XUV radiation. It is relevant also for near-edge core ionization. In the case of core ionization, furthermore, the parent ion itself is in a metastable state. The interplay between the photoelectron and the Auger electron is entirely neglected not only by the SAE method but also by computer codes restricted to single ionization.

A first step toward an accurate representation of correlated ionization dynamics near threshold can be achieved with the close-coupling (CC) approach. This approximation assumes that the parent ion of a target system explores only a finite number of localized bound states, while the photoelectron is unconstrained. The lowest-order approximation to this approach is the so-called "CI-singles" model, in which the configuration space comprises only the Hartree-Fock ground state of the target, as well as all single excitations from it. In this approach, the ionic states are assumed to be unrelaxed single determinants. Most of the correlation in the parent ion is ignored, which is a major limitation. However, in contrast

to SAE approaches, the approach already accounts for interchannel coupling.

A better approach is to describe the parent ions by correlated instead of monodeterminantal functions. In this case, the close-coupling framework allows one to represent with high accuracy the asymptotic portion of the wave function at any energy below the second ionization threshold. The inclusion of a few additional localized configurations for the neutral system not included in the CC expansion can greatly improve the quality of the wave function at short ranges as well. This approach to the definition of a system configuration space is used by most current state-of-the-art codes for atomic and molecular ionization. These codes are able to reproduce with variable accuracy the valence multiphoton ionization cross sections of atoms and even small molecules in the fixed-nuclei approximation.

The current limitations of these codes are threefold. First, the short-range correlation may require a very large number of configurations to reach convergence. Second, the calculation of matrix elements between the close-coupling wave functions with strongly correlated ions can be extremely complex. Many of the currently existing programs, therefore, restrict the configuration space of the ions, or neglect some exchange terms in the hamiltonian. Third, the size of the target ion is limited, either by the difficulty of carrying out many-body calculations in large systems or because the numerical method forces the parent ion to be confined to a comparatively small sphere. None of these codes is currently able to describe correlated double-ionization processes in polyelectronic systems.

In the case of genuinely two-body systems, such as helium or the H_2 molecule, it is possible to include in the CC calculation the full-CI space of localized configurations built from an effectively complete set of orbitals in a sphere of the size of tens of Bohr radii. In this case, therefore, as far as single-ionization states are concerned, the representation of the system in the fixed-nuclei approximation can be virtually exact.

As soon as the number of electrons liberated to the continuum or the number of active electrons in the ion increases, however, the complexity of the problem explodes exponentially. For example, even two-electron systems push the current limit of computation when they are explored above the double-ionization threshold. In this case, the state of neither of the two electrons can be restricted to a fixed small set of orbitals. Furthermore, the two electrons keep interacting appreciably up to large distances. For this reason, a large number of states, of the order of several thousands for each electron, must be considered. This results in configuration spaces with sizes of the order of millions. Consequently, a complete spectral resolution of the Hamiltonian is out of the question.

In molecules, the nuclear and rotational motions should, in principle, be taken into account explicitly. However, a first-principles approach combining the nuclear and electronic dynamics in short and intense laser pulses is at the moment computationally prohibitive. Nevertheless, impressive efforts have recently been pursued to combine, with some necessary approximations (e.g., the Born-Oppenheimer approximation and semi-classical nuclei propagation), the nuclear dynamics within the density-functional formalism.

Fortunately, many ultrafast processes in molecules subjected to short pulses can be modeled, to a good approximation, by assuming fixed nuclei. This approximation is justified considering the slow motion of the nuclei when compared to the ultrafast electronic motion. As a consequence, it is often possible to consider the effect of the laser at different relevant molecular geometries and invoke the Franck-Condon approximation when necessary. While rotational averaging can readily be performed for weak-field processes in randomly oriented molecules, nonperturbative processes require repeating calculations for many molecular orientations, which can be computationally demanding.

Below we list a number of methods and computer codes that are currently available. A first group of methods, known as time-dependent (TD) multiconfiguration (MC) self-consistent-field (SCF) approaches, bypass the demanding basis requirement of close-coupling approaches by optimizing a limited number of orbitals during the simulation. TDMCSCF methods achieve an extremely compact description for the wave function, paying the cost of propagating nonlinear equations. These methods include multiconfiguration TD Hartree [355] and Hartree-Fock [356–361], TD restricted-active-space (RAS) SCF [362–366], TD generalized-active-space SCF [367,368], TD complete-active-space SCF [369–371], TDMCSCF [372], and TD coupled-cluster methods [373–377]. These methods are particularly suited to reproduce optical observables, such as high-harmonic generation. Since the parent ions can continue evolving close to the asymptotic limit, even in the absence of external fields, channel-resolved photoelectron distributions may be more difficult to converge.

The methods mentioned below are based on the CC method. While more computationally expensive than the SAE or TDSCF methods, CC guarantees that the wave function of the photo fragments have the correct asymptotic behavior and that the time evolution is rigorously linear, which allows for stable and easily parallelizable solvers. The CC methods differ in how they represent electronic correlation in the ions, in the approximations used to compute the representatives of the relevant operators in the CC basis, and in the constraints they set on the size of the target system, and on its maximum excitation energy.

The most elementary realization of the CC approach is the so-called configuration-interaction singles (CIS) [378–381] approach, which restricts the configuration space to single excitations from a reference monodeterminantal ground state. While simple to implement, the CIS method can reproduce only a limited set of ionic thresholds and, lacking double excitations, it underestimates correlation.

In more accurate CC implementations, the parent ions are expressed in a multiconfiguration basis, and the CC expansion may include a nourished group of localized configurations for the neutral system to reproduce the dynamic correlation correlations in bound and continuum states that is not captured by the conventional CC expansion alone. Different programs implement various strategies to mix Gaussian-type orbitals, which are best suited to represent states localized near the nuclei, with numerical bases, which are required to reproduce photoelectron states at intermediate and large distances from the molecule. Numerical functions include monocentric

[382] and polycentric [319] B-splines, or monocentric [383] and polycentric finite-element discrete variable representation (FEDVR) functions [384].

The R-matrix method for atomic, molecular, and optical processes [385] is a general approach to solve the close-coupling equations for electron collisions with atoms, ions, and molecules. This includes the final state after photoionization or photodetachment. Since the method is also applicable to the calculation of bound states, it can be used to generate the necessary matrix elements to describe photoinduced processes. Originally implemented for electron scattering and stationary regimes, the atomic packages RMATRX-I [386,387] and RMATRX-II [388], as well as UKRMOL [389–391] have recently been extended to time-dependent photoionization processes, resulting in the general R-matrix with time-dependence RMT code [299,392], which can treat atoms and molecules in arbitrarily polarized short-pulse intense laser fields. Specifically for molecules, UKRMOL+ [392–397] employs hybrid Gaussian B-spline bases and can deal with arbitrary hybrid integrals.

A promising alternative to the standard implementation of the R-matrix approach is the B-spline R-matrix (BSR) method developed by Zatsarinny [398,399]. In addition to the use of B-splines, which has since been adapted in the most recent versions of RMATRX-I, RMATRX-II, and UKRMOL+, the use of nonorthogonal sets of term-dependent one-electron orbitals can reduce the size of the CI expansion considerably while maintaing and often even improving the accuracy of the target description. Efforts to interface the output from the atomic BSR package with RMT are currently in progress.

The Complex-Kohn approach has an economical representation of the continuum functions, since it identifies, beyond a certain distance, the channel functions with a linear combination of their asymptotic regular and irregular components. The implementation of the Complex-Kohn method developed by McCurdy, Orel, Rescigno, Schneider, and others [400–406], which we will refer to as CK-MESA, is based on the MESA program and has the unique capability of reproducing dynamic correlation through an optical potential generated from a large configuration space of localized functions. This approach allows to compute accurate scattering and photoionization cross sections. While CK-MESA was originally restricted to one-photon transition processes, it was recently extended to account for continuum-continuum radiative transitions and two-photon transitions processes [407]. A variant called ATTOMESA, in which the analytic asymptotic continuum functions are replaced by FEDVR functions, currently under development in the group of Douguet, promises to be able to reproduce arbitrary nonperturbative processes, such as strong-field ionization and high-harmonic generation.

The Recursive indeXing code (T-RECX) is a code for integrating *ab initio* the time-dependent Schrödinger equation of atoms and molecules [408–411]. It is able to carry out close-coupling calculations in a hybrid basis for systems in intense laser fields. It can treat both single and double ionization processes, nonlinear models (in which the Hamiltonian depends in a simple way on the wave function being propagated), and source terms.

The XCHEM code implements a close-coupling approach that leverages the multiconfiguration methods implemented in state-of-the-art quantum chemistry (QC) programs, such as MOLCAS, to evaluate close-coupling matrix elements in the molecular region. Since QC programs contemplate only Gaussian orbitals, XCHEM defines a large set of single-center tempered Gaussian functions to fill the space of possible configurations for the photoelectron within a fixed radius from the molecular center of mass. Beyond this radius, the ionic orbitals are assumed to be negligible, and the polycentric character of any virtual polycentric orbital is assumed to be well represented by a single-center expansion. In this way, XCHEM reduces the calculations of all the CC matrix elements that involve numerical orbitals to simple monocentric integrals [412–418]. XCHEM, which can account for a short-range correlation space and can compute ions at the RAS-SCF level, is well suited to accurately reproduce the photoionization of small molecules, both in stationary regime and resolved in time.

Recently, Ruberti developed a new code for time-resolved molecular ionization that is based on the algebraic diagrammatic construction [419–424]. The code makes use of the polycentric B-spline basis developed for TIRESIA.

The multichannel Schwinger configuration interaction method (MCSCI), developed by Robert Lucchese, implements the graphical unitary group approach [425–427] for linear molecules, taking molecular symmetry fully into account. The method has been successfully applied to time-resolved photoelectron spectroscopy [369,427,428].

Attosecond transitions (ASTRA) [429] is a recently developed wave-function close-coupling approach based on the formalism of transition-density-matrix close-coupling. ASTRA implements the exact expressions of the matrix elements between close-coupling states in a hybrid basis, which allows it to tackle larger molecules, and it uses the efficient formalism of spin-strings [430] to compute transition-density-matrix elements between ionic states of arbitrary symmetry and multiplicity. ASTRA relies, for the QC part, on LUCIA, a large-scale CI code developed by Olsen, and for the hybrid-integral part on the GBTOlib library, developed by Masin. Currently, the code is capable of reproducing the photoionization cross section and molecular-frame photoelectron angular distributions in molecules such as N_2, CO, and formaldehyde, at the same level of accuracy as the other state-of-the-art molecular-ionization codes.

C. Novel observables enabled by polarization control at XFELs

Jérémy R. Rouxel and Shaul Mukamel.

The appeal of polarization control at FELs to monitor molecular chirality has already been introduced in Sec. III A. Sections III C to III F demonstrate how PECD can be a sensitive probe of molecular chirality with unusually large asymmetry ratios. Here, we survey other chirality-sensitive techniques [431] that make use of FEL polarization control, and in particular of CPL.

The precise control of FEL polarization is now enabling the design of novel windows for molecular chirality in the time-domain in a near future. The description and interpretation of ultrafast chiral spectroscopic observables thus combines the challenges from both chirality and ultrafast dynamics. X-ray chiral signals naturally provide two structural information:

the mirror inversion breaking probed by chiral signals and a window onto local atomic structures through the element sensitivity of x-rays at resonance. The ultrashort time-resolution offered by FELs will allow to selectively target local ultrafast dynamics involving parity breaking, making and changes. Examples include photodissociation at a chiral center [432,433], low-energy vibrational dynamics [434], and ligands twisting in chiral metallic complexes [435]. In the frequency-domain, synchrotron-based x-ray Circular Dichroism (XCD) experiments probing local chirality in crystals and molecules have been achieved in recent decades [436–438]. Experiments at FELs using circularly polarized light are still few [434].

Many chiral-sensitive signals rely on CPL differential measurements to generate a dichroic response that cancels out in the electric-dipole (ED) response. These signals include x-ray CD[174,175,276,277] or x-ray Raman optical activity [439], and can be well-described by using the multipolar expansion truncated at the magnetic dipole (MD)/electric quadrupole (EQ) order [438]. In this case, the interaction Hamiltonian coupling the x-ray pulses and the matter is

$$H_{\rm int}(t) = -\boldsymbol{\mu}\cdot\boldsymbol{E}(t) - \boldsymbol{m}\cdot\boldsymbol{B}(t) - \boldsymbol{q}\cdot\boldsymbol{\nabla E}(t), \tag{2}$$

where $\boldsymbol{\mu}$, $\boldsymbol{m}$, and $\boldsymbol{q}$ are electric dipole, magnetic dipole, and electric quadrupole operators, respectively. Signals relying on higher multipoles are intrinsically weak since they are a small correction over an achiral background. PECD [143] and nonlinear even-order techniques offer large asymmetry ratios since they chiral sensitive at the electric dipole order. However, XCD relies on differential absorption which is a simple process to describe and implement experimentally.

In the EUV or x-ray regime, signals relying on the multipolar expansion can also greatly profit from quadrupolar interactions since x-rays have large wave vectors. Static signals XCD cannot take advantage of this because the ED-EQ two-point response tensor $\langle\boldsymbol{\mu q}\rangle$ vanishes upon rotational averaging. For time-dependent signals, the situation is different. They involve higher rank matter response tensors and one must include quadrupolar couplings [440]. For example, the perturbative description of a standard pump-probe experiment involves a four-point correlation function $\langle\boldsymbol{\mu\mu\mu\mu}\rangle$ of transition electric dipoles μ. Time-resolved XCD (tr-XCD) measures the circular dichroism of a delayed x-ray probe beam following an actinic pulse that triggers a chiral nuclear dynamics. It has contributions from 8 response functions ($\langle\boldsymbol{\mu\mu\mu m}\rangle$, $\langle\boldsymbol{\mu\mu\mu q}\rangle$ and their permutations of the $\boldsymbol{m}$ and $\boldsymbol{q}$ interactions). Here, both the magnetic dipole and electric quadrupole coupling with the ultrafast x-ray probe will contribute to the signal. On computational aspects, the numerical calculation of multipoles must be done with caution. When using a truncated basis, the multipoles matrix elements can become dependent on the origin of coordinates and special care must be made to recover accurate observables by summing over states, using a gauge-including atomic orbitals [441,442]. Finally, x-ray molecular chirality in the multiscattering regime of EXAFS signals is virtually unexplored and may require a different level of theory [437].

Alternative approaches avoiding the multipolar expansion altogether can be envisioned to simplify the numerical calculation of chiral observables and to build different intuitions. Rather than using a truncated multipolar expansion and extract the pseudoscalars measured by a given technique, one can use the complete radiation-matter interaction Hamiltonian [443]. The Power-Zienau-Woolley Hamiltonian $H_{\rm PZW} = -\int d\boldsymbol{r}\boldsymbol{P}(\boldsymbol{r})\cdot\boldsymbol{E}(\boldsymbol{r},t) - \int d\boldsymbol{r}\boldsymbol{M}(\boldsymbol{r})\cdot\boldsymbol{B}(\boldsymbol{r},t)$ is based on the full matter polarization and magnetization fields, and can be used as a starting point for a truncated multipolar expansion as discussed above. Its implementation is not easy since there are no simple closed-form operators corresponding to the classical polarization and magnetization [444]. It is simpler and more physically sound to use the minimal coupling description that is based on the charge and current density operators:

$$H_{\rm mc} = -\int d\boldsymbol{r}\boldsymbol{j}(\boldsymbol{r})\cdot\boldsymbol{A}(\boldsymbol{r},t) - \frac{e}{2m}\int d\boldsymbol{r}\,\sigma(\boldsymbol{r})\boldsymbol{A}^2(\boldsymbol{r},t), \tag{3}$$

where $\boldsymbol{j}$ and σ are the current and charge density operators. $\boldsymbol{A}$ is the transverse component of the incoming x-ray pulse. The expectation values of $\boldsymbol{j}$ and σ have an obvious physical meaning and are relatively simple to compute from *ab initio* packages. The multipolar expansion of polarization-based signals is thus circumvented, and chiral techniques involving x-ray field with important spatial variations can be considered [431].

For example, the ultrafast x-ray CD signal can be expressed as [445]:

$$S_{\rm CD}(\omega,T) = S_{\rm abs}(\omega,T,L) - S_{\rm abs}(\omega,T,R), \tag{4}$$

where ω is the detected spectrum of the transmitted dispersed probe, T is the time delay between the actinic pulse and the probe. The actinic pulse is included implicitly in the wave function and its interaction can be calculated perturbatively or numerically. The frequency-dispersed absorption signal in the minimal coupling picture is given by

$$S_{\rm abs}(\omega,T,L/R) = \frac{2}{\hbar}{\rm Im}\int d\mathbf{r}\langle\mathbf{J}_{L/R}(\mathbf{r},\omega)\rangle_\Omega\cdot\mathbf{A}^*_{L/R}(\mathbf{r},\omega), \tag{5}$$

where the current expectation value is given by

$$\mathbf{J}_{L/R}(\mathbf{r},t) = -\frac{i}{\hbar}\int dt'd\mathbf{r}'\langle\mathbf{j}(\mathbf{r},t)\mathbf{j}(\mathbf{r}',t')\rangle_\Omega\cdot A_{L/R}(\mathbf{r}',t') - \langle\mathbf{j}(\mathbf{r}',t')\mathbf{j}(\mathbf{r},t)\rangle_\Omega\cdot A^*_{L/R}(\mathbf{r}',t'). \tag{6}$$

Here, $\mathbf{j}$ is the transition current density and $\mathbf{A}_{L/R}$ is the vector potential of the incoming field with left or right circular polarization. Ω indicates rotational averaging over the molecular ensemble. The time of arrival T of the CD probe pulse and its central frequency ω are implicitly contained in the field $\mathbf{A}$.

Equations (4)–(6) describe the differential absorption of an x-ray probe using the minimal coupling interaction Hamiltonian. This approach offers different intuition and possibilities, and also some new simulation challenges. The following discussion uses ultrafast x-ray CD as an example, but most of it can be adapted to other polarization-based chiral techniques.

First, the signal is expressed as a spatial overlap between the matter and field tensors. This is particularly convenient to include the effect of fields having complex spatial profiles, e.g., an OAM. x-ray OAM is an independent field degree of freedom from the spin angular momentum (SAM) that can be used conjointly with the OAM. Signal computations show that combining SAM and OAM could lead to increased chiral

sensitivity (higher asymmetry ratio), in an hybrid technique of circular and helical dichroism [172]. Studies suggest that the longitudinal polarization components that appear when beams are highly focused are the source of the largeer dichroic effect [446–448] Even when the light polarization is the only degree of freedom used in the dichroic measurement, the local nature of x-ray interactions [110] can make a spatially dependent description more insightful. Molecular chirality has long been considered as an on or off property (either the molecule is chiral or it is achiral) but x-rays sources now allow to study the spatial structure of the molecular chirality within the probed system.

A drawback of the exact description using current and charge densities is that the required rotational averaging for isotropic molecular ensembles becomes a nontrivial task. In the static case and within the multipolar description, the XCD signal is well described by a two-point correlation function of an electric and a magnetic dipoles. This second-rank tensor can be straightforwardly rotationally averaged analytically, leading to the well-known rotatory strength $R_{ij} = \boldsymbol{\mu}_{ji} \cdot \boldsymbol{m}_{ij}$. In the ultrafast regime, one must include the excited wave function into the matter rotational averaging. Neglecting reorientation during the dynamics (which holds for very short timescales) and considering first order perturbation on the wave function, one must then average a 4-rank (3ED/1MD) or a 5-rank tensor (3ED/1EQ). For a 4-rank tensor, there are 4 diagrammatic contributions to the chiral signals and the averaging tensor contains 9 terms, leading to 36 relevant correlation functions. This approach is tedious, not physically transparent, and becomes inadequate when using propagators allowing for reorientation or using the minimal coupling description. In this case, rotational averaging is best tackled numerically by calculating the signal on a grid of Euler angles [449] for an initial distribution of molecules and averaging it out.

Third, the temporal convolution that appears in Eq. (6) is a standard feature of time-domain observables when the impulsive limit cannot be used. It is likely that given the ultrashort nature of some chiral nuclear or electronic dynamics, the impulsive limit cannot be taken in polarization-based FEL dichroic measurements. For example, ultrafast X-ray CD can be used to monitor the flipping between two enantiomers around a chiral carbon. Typically, it is the lightest group that experience the most motion that can be as small as a single hydrogen atom. As a result, the chiral nuclear dynamics can be on the timescale of few femtoseconds [175]. Even shorter, ultrafast x-ray dichroic measurements can be used to probe charge migration in chiral molecules. To achieve chiral sensitivity, one must ensure that the field envelope is indeed shorter that the chiral dynamics, especially in the case in which the molecular bounces between its two enantiomers. Otherwise, the temporal integration averages them, and the dicroic signal vanishes. Alternatively, advanced polarization schemes can be employed in which the field envelope is not shorter than the chiral dynamics but its polarization evolves in time to follow it. This can be considered as a form of polarization pulse-shaping. For example, one could envision an experiment in which the field polarization state is left polarized for half the pulse envelope and then switches to right polarized. While this is challenging to achieve at an FEL, schemes relying on the combination of polarized radiation from two undulators could achieve nontrivial time-dependent polarizations [96].

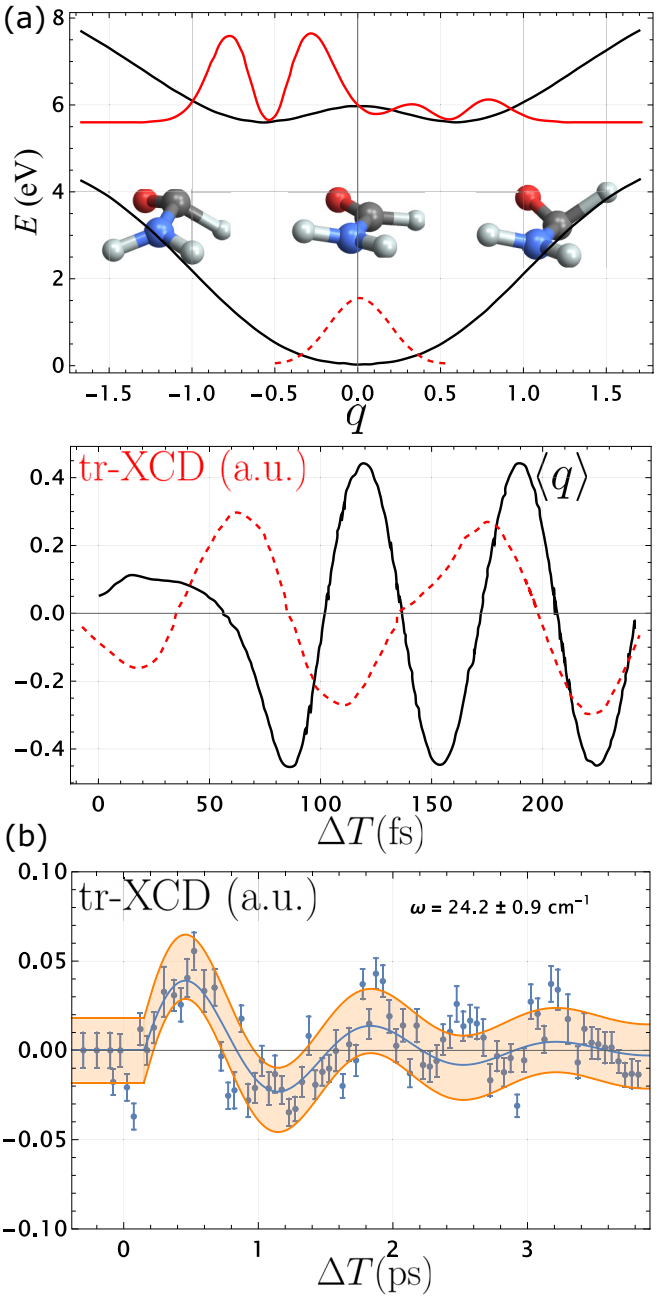

FIG. 32. (a) The formamide molecule is achiral in its ground state and becomes chiral in its first excited state through pyramidalization. When pumped by circularly polarized UV light, the nuclear wave packet oscillates between the two enantiomers (top panel). The tr-XCD signal (middle panel, dashed, red) follows closely the nuclear wave-packet center of mass dynamics (solid, black) [175] and is a sensitive probe of the local chiral nuclear dynamics. (b) tr-XCD can also be used as a local windows into chiral vibrational dynamics. In the lower panel, low-lying vibrational excitations are pumped by a UV Raman process [434] and tr-XCD is used as a local probe of chiral nuclear dynamics.

Figure 32 summarizes recent results on ultrafast chirality probed by x rays. In Fig. 32(a), the out-of-plane stretching of

formamide [175] was probed by pump-probe tr-XCD. In the excited state, the molecule experiences a pyramidalization and becomes chiral. When pumping the molecule with circular polarized light, an asymmetric wave packet is generated to generate an asymmetric nuclear wave packet in the first excited electronic state, that is the center of mass of the nuclear wave packet is located on one of the two possible enantiomers and oscillate between them on an ultrafast timescale. The tr-XCD signal at the carbon K-edge offers a sensitive probe of this time-evolution by following closely this oscillation between the two-enantiomers. Figure 32(b) displays the tr-XCD signal recorded on ibuprofen dimer pumped by ultrashort UV light and probed at the carbon K-edge [434]. Through a Raman process, a large amount of vibrational modes are excited and the ones with low-energies, describing global vibrational modes, are known to be difficult to disentangle. Using resonant ultrafast x-rays as a windows, one can select which group of carbon atoms are probed by selecting a central frequency and bandwidth exciting only these ones in the pre-edge C K-edge. The addition of the XCD detection mode further allows to probe only atoms located in parts of the molecule lacking mirror inversion. For example, we have recently shown that chlorine and fluorine atoms substituted at different locations in a helicene molecule can be used as probes of the local helical state of the molecular helix [450]. Helicenes are screw-shape molecules that can racemize by reaching a thermally, globally achiral, excited state of mixed helicity of opposite side of the molecule. From that state, one of the two sides can switch to the opposite helicity and time-resolved XCD resonant with the Cl or F atomic chromophores can be used to monitor on which side this is happening.

While this brief overview has mostly focused on the use of CPL, the probing of molecular chirality can also be achieved using schemes relying on controlled linear polarizations. Even-order spectroscopies, for example, sum frequency generation of difference frequency generation, are sensitive to chirality in the bulk of isotropic ensembles [451]. A condition on the applicability of the technique is that the triple product of the three involved field polarizations do not vanish, i.e., they are not coplanar. This calls for multipulse FEL schemes with independent linear polarizations. Similarly, it has been shown that cross-polarization transient grating experiments is sensitive to molecular chirality [452]. Such experiments involve the crossing of two FEL beams with crossed linear polarizations on a chiral sample and the diffraction of a delayed probe is measured.

D. Toward time-resolved emitter-site-selective PECD of fixed-in-space chiral molecules

Philipp V. Demekhin and Nikolay M. Novikovskiy.

Short-wavelength radiation provided by XFELs governs primary inner-shell ionization and, thus, addresses individual chemical elements (electron emitters) located on specific molecular sites. In many cases, electrons ejected from equivalent emitters experience different chemical shifts and can thus be distinguished due to their kinetic energy. Being created at a specific site of a molecule, an initially well-localized photoelectron wave packet propagated outwards and experiences each and every detail of the molecular potential on its way out. An accompanying multiple scattering of this wave packet on a molecular scaffold results in characteristic interference and/or diffraction pattern in the resulting photoelectron angular emission distributions, which thus provide detailed information on the molecular potential itself. In many cases, the photoemission probability depends on the polarization of the ionizing radiation, resulting thereby in a variety of dichroic phenomena. Particularly promising is the fascinating chiroptical phenomenon of forward-backward asymmetry in the photoemission from randomly oriented chiral molecules with respect to the propagation direction of circularly polarized light [208], known as PECD.

One usually distinguishes two contributions to PECD: one from a chiral initial electronic state and another from chiral final continuum state of the photoelectron, both naturally imprinted in the electric-dipole transition matrix element. In the case of inner-shell photoionization from an almost-symmetric inner-shell orbital, the former contribution is negligibly small. Thereby, in the inner-shell ionization, PECD is governed solely by the final-state effect, which offers a unique opportunity to inspect chiral asymmetries of the potential of the molecular ion. To date, many experimental and theoretical studies on randomly oriented chiral molecules in the gas phase confirmed that PECD in inner-shell ionization [109,110,140,144,201,202,321,453–463] is as large as in the outer-shell ionization, where a chiral asymmetry of the initial state can play an additional role. Those studies suggest site-selectivity [109,321,453,456,457,461] and emitter-selectivity [109,321,461] of inner-shell PECD, as well as its complex dependence on the molecular configuration [321,458–460] and photoelectron energy [144,321,453–455,457,460], indicating also an important role of the core-excited resonances [140,456,457]. Utilizing polarization-controlled FELs in the future may thus be a perspective route to explore the emitter-site-selectivity of inner-shell PECD in a nonlinear regime.

Any inner-shell ionization is undoubtedly followed by a radiative or Auger decay (or even a cascade of the decay events), which increases the charge state of the residual ion. Such highly charged molecular ions are typically unstable and undergo an ultrafast dissociation by a Coulomb explosion into several ionic and neutral fragments. Under the assumption of the so-called axial-recoil approximation [200], which suggests a moderate deterministic rotation of a molecule during its ultrafast fragmentation, the ionic momenta provide access to the spatial orientation of the molecule at the instant of photoionization. Measuring the photoelectron momentum in coincidence with the ionic momenta, allows to access its relative emission angle in the molecular frame of reference [198,404,464,465], so-called molecular frame photoelectron angular distributions (MFPADs).

Even achiral molecules, being distinctly oriented in space, show a number of dichroic phenomena in photoemission, such as circular dichroism in the angular distribution (CDAD, [466,467]) or an *apparent* PECD [468], both on the order of 100%. Such orientation-induced dichroic asymmetries in the photoemission superimpose with the intrinsic dichroic asymmetry present in chiral molecules, resulting in a much stronger PECD for spatially oriented chiral molecules, as well [201,202,460–463]. This is because averaging over molecular orientations leads to a loss of information,

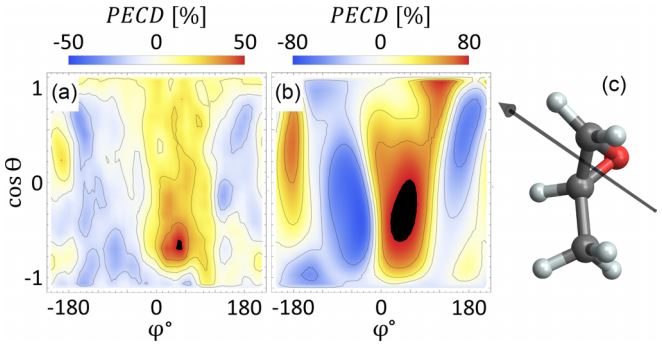

FIG. 33. Measured (a) and computed (b) differential PECDs of the O 1s-photoelectrons of S-methyloxirane with the kinetic energy of 11.5 eV as functions of the two photoelectron emission angles for the chosen molecular orientation with respect to the light propagation direction panel (c). At certain photoemission directions (indicated by black color), the measured and computed PECDs exceed the chosen upper and lower limits of the respective asymmetry scales. The figure has been adapted and reprinted with permission from Ref. [201].

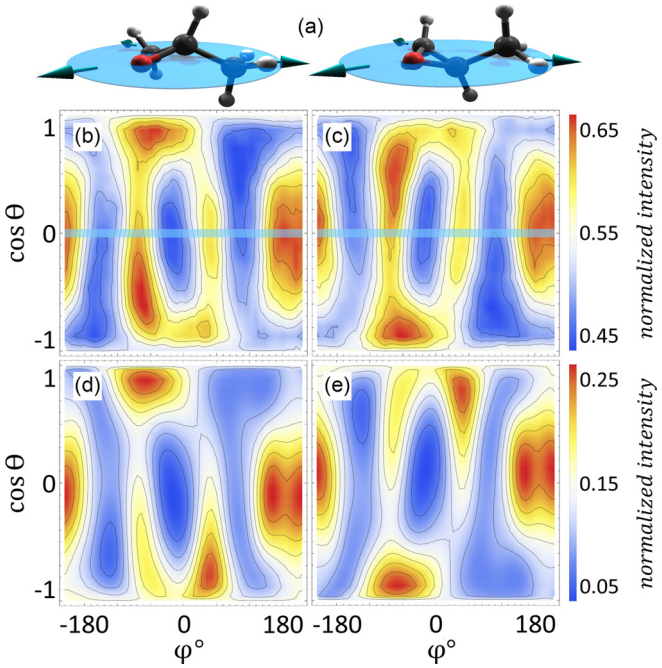

FIG. 34. A visualization of two enantiomers of methyloxirane molecule (a) and the respective molecular frames of reference derived from the measured asymptotic momenta of three fragments (turquoise arrows which define cyan plane for each enantiomer). Polarization-averaged angular emission distributions of the O 1s-photoelectrons with the kinetic energy of 11.5 eV, measured (b), (c) and computed (d), (e) for two enantiomers of methyloxirane in the frame of molecular reference. Switching between two enantiomers reflects the PA-MFPADs with respect to the cyan plane [indicated by the horizontal line in panels (b) and (c)]. The figure has been adapted from Ref. [462].

reducing thereby the PECD substantially [208]. In particular, fixing already one molecular orientation axis in space increases the PECD by a factor of about ten [202,460,461], and the differential PECD of a fully fixed-in-space molecule can reach up to 100% [201,202,463]. The latter fact is illustrated in Fig. 33, which depicts a normalized difference of the photoelectron distributions of a fixed-in-space S-methyloxirane molecule recorded for circularly polarized light with positive and negative helicities, $\mathrm{PECD}(\theta,\varphi) = [I_+(\theta,\varphi) - I_-(\theta,\varphi)]/[I_+(\theta,\varphi) + I_-(\theta,\varphi)]$. The considered molecular orientation with respect to the light propagation direction is visualized in Fig. 33(c). As one can see, for some photoelectron emission angles (black spots), the measured PECD in panel A exceeds 50%, while the computed PECD in Fig. 33(b) is somewhat stronger. Such a strong dichroic asymmetry in the photoemission from fixed-in-space molecules increases the sensitivity for chiral recognition in the gas phase [201].

Even polarization-averaged MFPADs are enantiosensitive [462]. This fact is illustrated in Fig. 34, which depicts the measured [Figs. 34(b) and 34(c)] and computed [Figs. 34(d) and 34(e)] PA-MFPADs of two enantiomers of methyloxirane. As one can recognize from panel A, the momenta of three molecular fragments define a plane, and switching between the two enantiomers reflects the molecule with respect to this plane. As a consequence, the respective PA-MFPADs for two enantiomers are just mirror-images of each other with respect to $\cos\theta = 0$ [the horizontal line in Figs. 34(b) and 34(c)]. In the experiment, such PA-MFPADs provide much higher statistics, since they include all photoionization events averaging over all possible directions from which the ionizing light hits the molecule. As a consequence, such PA-MFPADs can be utilized for the determination of the geometrical structure (bond length, angles, etc.) of molecules with enantioselectivity and an accuracy of about 5%, even for weak scatterers such as hydrogen atoms [462].

A new type of experiments with polarization-controlled FELs on the time-resolved PECD of randomly oriented chiral molecule was performed in Ref. [110] at the AMO beamline of the LCLS at the SLAC National Accelerator Laboratory in the USA. It is based on the x-ray pump–x-ray probe scheme, where the pump pulse triggers molecular fragmentation dynamics by ionizing the F 1s-shell of a trifluoromethyloxirane molecule. After an ultrafast Auger decay, the doubly charged molecule can Coulomb-explode into a fluorine ion and the singly charged mother-fragment. The time-delayed x-ray probe pulse releases an additional F 1s-photoelectron from the mother-fragment, and its PECD is investigated as a function of the time delay between two pulses, i.e., at different internuclear separations between the ions. The PECDs, computed in Ref. [110] in the SAE approximation for individual combinations of the ejected and ionized fluorine atoms, vary by almost an order of magnitude for rather large elongations of the bond to about 12 a.u. (far beyond the chemical bond breaking), which corresponds to the time-delay of about 150 fs. Such a long-range sensitivity of the PECD can be explained by the long-range influence of the Coulomb potential of the fluorine ion, which is seen by the mother-fragment. However, averaging over possible combinations of the primary and secondary addressed fluorine atoms makes the effect almost independent of the separation, but still observable.

In a recent UV pump–XUV probe experiment [112], performed at the Free-electron LASer in Hamburg (FLASH),

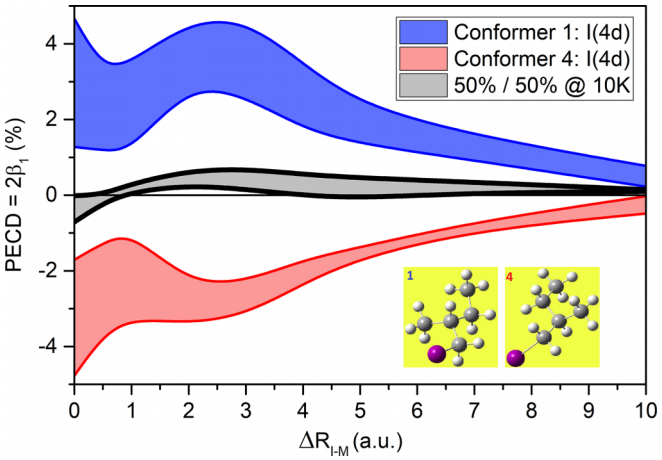

FIG. 35. Theoretical PECD of the 4d-photoelectrons of the iodine atom, computed for (R)-1-iodo-2-methylbutane at different distances $R_{\text{I-M}} = R_{\text{eq}} + \Delta R$ between the neutral chiral mother-fragment and neutral iodine atom dissociating along the bond. The shaded areas represent dispersions of the PECDs in the selected kinetic energy interval of 4–8 eV. The theory predicts that averaging over the relevant conformers results in an almost complete cancellation of the effect.

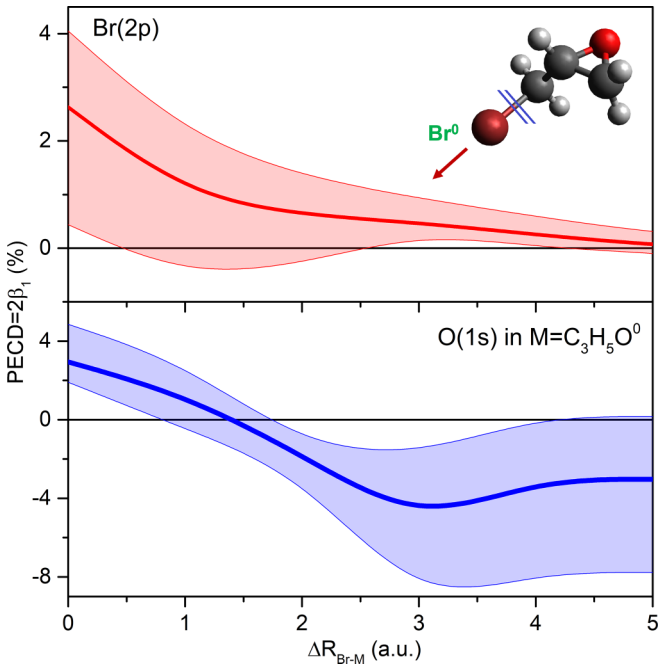

FIG. 36. Theoretical PECD of the 2p-photoelectrons of the bromine atom (upper panel) and 1s-photoelectrons of the oxygen atom (lower panel), computed for (R)-epibromohydrin at different distances $R_{\text{Br-M}} = R_{\text{eq}} + \Delta R$ between the neutral chiral mother-fragment and neutral bromine atom dissociating along the bond. The shaded areas represent dispersions of the PECDs in the selected kinetic energy intervals of 4–8 eV for Br 2p- and 5–9 eV for O 1s-photoelectrons. The theory predicts that PECD saturates to its asymptotic values if the bond length is enlarged already by about 5 a.u.

a neutral dissociation of a chiral molecule 1-iodo-2-methylbutane was studied by examining the ultrafast evolution of the iodine 4d binding energy. In the experiment, the UV pump pulse excites the molecule in a dissociative state such that a neutral iodine atom is ejected, and the time-delayed XUV pulse probes the 4d-shell of iodine at different separations from the neutral mother-fragment. Unfortunately, the PECD of the released photoelectrons was not accessible in the experiment [112]. A simulation of the time-resolved PECD of the 4d-photoelectrons of the iodine atom, which can be expected in such an experiment, is shown in Fig. 35. These estimates were performed by the single center (SC) method and code [469–471] in the SAE approximation under assumptions that: (i) the iodine atom dissociates along its initial bond, and (ii) the geometry of the mother-fragment does not adjust in the course of the fragmentation.

A noticeable PECDs of the 4d-photoelectrons of the iodine atom as a function of internuclear separation from the rest of the 1-iodo-2-methylbutane molecule during its neutral dissociation can be seen in Fig. 35 for two relevant conformers of the molecule (see insets). The effect persists far beyond the chemical bond breaking up to elongations of the bond by about 10 a.u., which, according to Ref. [112] (see Fig. 10 there), corresponds to a time-delay of about 175 fs. Such a long-range PECD sensitivity can be explained by the large scaffold of the mother fragment, which is seen by the 4d-photoelectron emitted from the iodine atom within a large solid angle even at these separations. Nevertheless, Fig. 35 predicts that averaging the PECDs over two conformers, which are relevant at the temperature of 10 K, makes the effect almost undetectable. One, thus, would need to decrease the temperature in a molecular beam to make contribution from the ground-state conformer dominant.

To conduct a successful experiment on time-resolved PECD at a polarization-controlled FEL, it is extremely important to find a suitable candidate-molecule, which is free of the disadvantages discussed above. Since larger chiral molecules appear usually in many (energetically close-by) conformer configurations, one can look for more compact (and therefore) conformer-free chiral molecules. Figure 36 depicts results of a theoretical simulation of the time-dependent PECD of epibromohydrin molecules. Similarly to the just discussed process, an UV pump pulse initiates a neutral dissociation of the bromine atom along its bond, and a delayed x-ray pulse probes either the 2p-shell of the bromine atom (upper panel) or the 1s-shell of the oxygen atom in the remaining neutral mother-fragment (lower panel) as a function of their separation. Simulations were performed by the SC method [469–471] in the SAE approximation under similar assumptions as in Fig. 35. Figure 36 illustrates a measurable PECDs which saturate to their asymptotic values (zero for Br 2p-photoelectrons in the upper panel and a constant value for O 1s-photoelectrons of the chiral mother-fragment in the lower panel) when the respective bond elongates by about 5 a.u. Thus, the time-evolution of the PECDs can be traced here using pump-probe time-delays below 100 fs. Such a short-range sensitivity of the PECDs is a disadvantage of using small chiral molecules, for which photoelectrons emitted from one of the fragment see another fragment only in a relatively small solid angle already at short separations.

Summarizing, studies of time-resolved emitter-site-selective PECD of fixed-in-space chiral molecules in the

gas phase and their ultrafast structure determination via photoelectron-diffraction patterns are far-reaching and have a bright perspective for application of FELs with polarization control. Performing, however, robust experiments on the PECD and its temporal evolution on an ensemble of randomly oriented chiral molecules with the FELs is a very important intermediate milestone.

V. SUMMARY AND OUTLOOK

Free-electron lasers are evolving to be versatile machines for site specifically investigating polarization dependent phenomena in, e.g., chiral and oriented systems in the gas phase via dichroic phenomena. Their ultrashort and ultrabright pulses unprecedentedly allow for creating and interrogating hitherto inaccessible states of (transient) matter, and to investigate electronic and structural properties and dynamics of small systems, with imminent perspectives toward larger molecules such as amino acids and peptides. One of the core pillars of FEL-driven gas-phase science is the fundamental correlation of the physics perspective and the subsequently evolving chemical perspective. Latest technological breakthroughs of FEL-operation such as full polarization control with seeded or attosecond pulses in combination with state-of-the art optical lasers, new sample delivery methods, advanced theoretical modeling and data analysis, as well as sophisticated instrumentation and diagnostics set the stage for a novel field of research with promising prospects for science, industry, and society. Several facilities worldwide have identified this opportunity and have initialized the respective efforts, as presented above in the first section of this roadmap. The subsequently discussed opportunities for experimental and theoretical sciences in the light of these developments sketched the state-of-the-art in this young field of research.

ACKNOWLEDGMENTS

This work has been supported by the Bundesministerium für Bildung und Forschung (BMBF) Grant No. 13K22CHA. M.I. acknowledges funding from the Volkswagen Foundation for a Peter-Paul-Ewald Fellowship. M.I., P.V.D., N.M.N., and R.D. acknowledge support from the Deutsche Forschungsgemeinschaft (DFG)—Project No. 328961117-SFB 1319 ELCH ("Extreme light for sensing and driving molecular chirality"). W.H. and M.I. acknowledge funding of the BMBF-ErUM-Pro project "TRANSALP" (Grant No. 05K22PE3). P.W. acknowledges funding from SLAC under the U.S. Department of Energy, Office of Science, Office of Basic Energy Sciences under Contract No. DE-AC02-76SF00515. J.B. and J.W. acknowledge funding from the DFG under Projects No. 429194455 and No. 465098690. S.B. and L.S. acknowledge support from DESY (Hamburg, Germany), a member of the Helmholtz Association HGF and the Helmholtz Initiative and Networking Fund. H.D. acknowledges the National Natural Science Foundation of China (Grants No. 12125508 and No. 11935020). C.F. acknowledges the National Natural Science Foundation of China (Grants No. 12122514 and No. 11975300). K.B. acknowledges funding from the U.S. National Science Foundation under Grants No. PHY-2110023 and No. PHY-2408484. N.D. acknowledges funding from the U.S. National Science Foundation under Grant No. PHY-2012078. L.A. acknowledges funding from the U.S. National Science Foundation under Grant No. 2309133, and from the DOE AMOS program under Grant No. DE-SC0020311. C.V. acknowledges support from the European Union's Horizon 2020 research and innovation program under Grant Agreements No. 860553 (SMART-X) and No. 654148 (LASERLAB-EUROPE), and from the European COST Action No. CA18222 (AttoChem). F.C. and M.I. acknowledge the Cluster of Excellence "Advanced Imaging of Matter" of the Deutsche Forschungsgemeinschaft (DFG)—EXC 2056—Project ID No. 390715994. F.C. furthermore acknowledges the DFG—SFB-925—Project ID No. 170620586, and the COST action No. CA18222 Attochem. J.R.R. acknowledges support from the U.S. Department of Energy, Office of Science, Basic Energy Science, Chemical Sciences, Geosciences and Biosciences Division under Contract No. DE-AC02-06CH11357.

[1] C. Bostedt, J. Bozek, P. Bucksbaum, R. Coffee, J. Hastings *et al.*, Ultra-fast and ultra-intense x-ray sciences: First results from the LINAC coherent light source free-electron laser, J. Phys. B: At. Mol. Opt. Phys. **46**, 164003 (2013).

[2] B. Erk, R. Boll, S. Trippel, D. Anielski, L. Foucar *et al.*, Imaging charge transfer in iodomethane upon x-ray photoabsorption, Science **345**, 288 (2014).

[3] L. Young, K. Ueda, M. Gühr, P. H. Bucksbaum, M. Simon *et al.*, Roadmap of ultrafast x-ray atomic and molecular physics, J. Phys. B: At. Mol. Opt. Phys. **51**, 032003 (2018).

[4] D. Rolles, Time-resolved experiments on gas-phase atoms and molecules with XUV and x-ray free-electron lasers, Adv. Phys.: X **8**, 2132182 (2023).

[5] J. Duris, S. Li, T. Driver, E. G. Champenois, J. P. MacArthur *et al.*, Tunable isolated attosecond x-ray pulses with gigawatt peak power from a free-electron laser, Nat. Photon. **14**, 30 (2020).

[6] N. Hartmann, G. Hartmann, R. Heider, M. Wagner, M. Ilchen *et al.*, Attosecond time–energy structure of x-ray free-electron laser pulses, Nat. Photon. **12**, 215 (2018).

[7] S. Li, T. Driver, P. Rosenberger, E. G. Champenois, J. Duris *et al.*, Attosecond coherent electron motion in Auger-Meitner decay, Science **375**, 285 (2022).

[8] A. A. Sorokin, S. V. Bobashev, T. Feigl, K. Tiedtke, H. Wabnitz, and M. Richter, Photoelectric effect at ultrahigh intensities, Phys. Rev. Lett. **99**, 213002 (2007).

[9] G. Doumy, C. Roedig, S.-K. Son, C. I. Blaga, A. D. DiChiara *et al.*, Nonlinear atomic response to intense ultrashort x rays, Phys. Rev. Lett. **106**, 083002 (2011).

[10] L. Young, E. P. Kanter, B. Krässig, Y. Li, A. M. March *et al.*, Femtosecond electronic response of atoms to ultra-intense x-rays, Nature (London) **466**, 56 (2010).

[11] B. Rudek, S.-K. Son, L. Foucar, S. W. Epp, B. Erk *et al.*, Ultra-efficient ionization of heavy atoms by intense x-ray free-electron laser pulses, Nat. Photon. **6**, 858 (2012).

[12] A. Rudenko, L. Inhester, K. Hanasaki, X. Li, S. J. Robatjazi *et al.*, Femtosecond response of polyatomic molecules to ultra-intense hard x-rays, Nature (London) **546**, 129 (2017).

[13] R. Boll, J. M. Schäfer, B. Richard, K. Fehre, G. Kastirke *et al.*, x-ray multiphoton-induced Coulomb explosion images complex single molecules, Nat. Phys. **18**, 423 (2022).

[14] T. Mazza, M. Ilchen, M. D. Kiselev, E. V. Gryzlova, T. M. Baumann *et al.*, Mapping resonance structures in transient core-ionized atoms, Phys. Rev. X **10**, 041056 (2020).

[15] U. Eichmann, H. Rottke, S. Meise, J.-E. Rubensson, J. Söderström *et al.*, Photon-recoil imaging: Expanding the view of nonlinear x-ray physics, Science **369**, 1630 (2020).

[16] N. Rohringer, x-ray Raman scattering: A building block for nonlinear spectroscopy, Philos. Trans. R. Soc. A. **377**, 20170471 (2019).

[17] G. Schütz, W. Wagner, W. Wilhelm, P. Kienle, R. Zeller, R. Frahm, and G. Materlik, Absorption of circularly polarized x rays in iron, Phys. Rev. Lett. **58**, 737 (1987).

[18] D. Higley, K. Hirsch, G. Dakovski, E. Jal, E. Yuan, T. Liu, A. Lutman *et al.*, Femtosecond x-ray magnetic circular dichroism absorption spectroscopy at an x-ray free-electron laser, Rev. Sci. Instrum. **87**, 033110 (2016).

[19] S. Sasaki, K. Kakuno, T. Takada, T. Shimada, K. ichi Yanagida, and Y. Miyahara, Design of a new type of planar undulator for generating variably polarized radiation, Nucl. Instrum. Methods Phys. Res. Sect. A **331**, 763 (1993).

[20] M. Calvi, C. Camenzuli, E. Prat, and T. Schmidt, Transverse gradient in APPLE-type undulators, J. Synchrotron Radiat. **24**, 600 (2017).

[21] P. Li, T. Wei, Y. Li, and J. Pflueger, Magnetic design of an Apple-X afterburner for the SASE3 undulator of the European XFEL, Nucl. Instrum. Methods Phys. Res. Sect. A **870**, 103 (2017).

[22] X. Liang, M. Calvi, C. Kittel, N. J. Sammut, and T. Schmidt, Advanced operational models of the APPLE X undulator, in *Proceedings of the FEL'19*, Free Electron Laser Conference (JACoW Publishing, Geneva, Switzerland, 2019), pp. 541–544.

[23] T. Schmidt, A. Anghel, P. Böhler, M. Brügger, M. Calvi, S. Danner *et al.*, Magnetic design of an Apple III undulator for SwissFEL, in *Proceedings of the 36th International Free Electron Laser Conference: FEL2014*, edited by J. Chrin, S. Reiche, and V. R. W. Schaa (JACoW Publishing, Basel, Switzerland, Geneva, Switzerland, 2015), pp. 116–120.

[24] T. Schmidt and M. Calvi, APPLE X undulator for the SwissFEL soft x-ray beamline athos, Synchrotron Radiat. News **31**, 35 (2018).

[25] J. Bahrdt *et al.*, In-vacuum APPLE II undulator, in *Proceedings of the 9th International Particle Accelerator Conference (IPAC'18)*, International Particle Accelerator Conference (JACoW Publishing, Geneva, Switzerland, 2018), pp. 4114–4116.

[26] H.-D. Nuhn, Polarizing afterburner for the LCLS-II undulator line, Technical report, SLAC National Accelerator Laboratory, Menlo Park, CA (2019).

[27] A. A. Lutman, J. P. MacArthur, M. Ilchen, A. O. Lindahl, J. Buck *et al.*, Polarization control in an x-ray free-electron laser, Nat. Photon. **10**, 468 (2016).

[28] S. Sasaki, Analyses for a planar variably-polarizing undulator, Nucl. Instrum. Methods Phys. Res. Sect. A **347**, 83 (1994).

[29] M. Kokole, T. Milharčič, G. Soregaroli, M. Tedeschi, M. Zambelli *et al.*, Magnetic characterization of the FEL-1 undulators for the FERMI@Elettra free-electron laser, in *Proceedings of the FEL'10* (JACoW Publishing, Geneva, Switzerland, 2010), pp. 664–666.

[30] M. Kokole, T. Milharčič, G. Soregaroli, M. Tedeschi, M. Zambelli *et al.*, Magnetic characterization of FEL-2 undulators for the FERMI@elettra free-electron laser, in *Proceedings of IPAC2011, San Sebastián, Spain* (2011).

[31] E. Allaria, L. Badano, S. Bassanese, F. Capotondi, D. Castronovo *et al.*, The FERMI free-electron lasers, J. Synchrotron Radiat. **22**, 485 (2015).

[32] E. Allaria, R. Appio, L. Badano, W. A. Barletta, S. Bassanese *et al.*, Highly coherent and stable pulses from the FERMI seeded free-electron laser in the extreme ultraviolet, Nat. Photon. **6**, 699 (2012).

[33] L. H. Yu, Generation of intense UV radiation by subharmonically seeded single-pass free-electron lasers, Phys. Rev. A **44**, 5178 (1991).

[34] E. Allaria, D. Castronovo, P. Cinquegrana, P. Craievich, M. D. Forno *et al.*, Two-stage seeded soft-x-ray free-electron laser, Nat. Photon. **7**, 913 (2013).

[35] P. R. Ribič, A. Abrami, L. Badano, M. Bossi, H. H. Braun *et al.*, Coherent soft x-ray pulses from an echo-enabled harmonic generation free-electron laser, Nat. Photon. **13**, 555 (2019).

[36] G. Penco, E. Allaria, G. D. Ninno, E. Ferrari, and L. Giannessi, Experimental demonstration of enhanced self-amplified spontaneous emission by an optical klystron, Phys. Rev. Lett. **114**, 013901 (2015).

[37] E. Allaria, B. Diviacco, C. Callegari, P. Finetti, B. Mahieu *et al.*, Control of the polarization of a vacuum-ultraviolet, high-gain, free-electron laser, Phys. Rev. X **4**, 041040 (2014).

[38] R. Bonifacio, F. Casagrande, G. Cerchioni, L. de Salvo Souza, P. Pierini *et al.*, Physics of the high-gain FEL and superradiance, La Rivista del Nuovo Cimento **13**, 1 (1990).

[39] K. J. Kim, A synchrotron radiation source with arbitrarily adjustable elliptical polarization, Nucl. Instrum. Methods Phys. Res. **219**, 425 (1984).

[40] K.-J. Kim, Circular polarization with crossed-planar undulators in high-gain FELs, Nucl. Instrum. Methods Phys. Res. A **445**, 329 (2000).

[41] E. Ferrari, E. Allaria, J. Buck, G. D. Ninno, B. Diviacco *et al.*, Single shot polarization characterization of XUV FEL pulses from crossed polarized undulators, Sci. Rep. **5**, 13531 (2015).

[42] E. Ferrari, E. Roussel, J. Buck, C. Callegari, R. Cucini *et al.*, Free-electron laser polarization control with interfering crossed polarized fields, Phys. Rev. Accel. Beams **22**, 080701 (2019).

[43] N. Sudar, R. Coffee, and E. Hemsing, Coherent x rays with tunable time-dependent polarization, Phys. Rev. Accel. Beams **23**, 120701 (2020).

[44] J. Morgan and B. McNeil, Attosecond polarization modulation of x-ray radiation in a free-electron laser, Phys. Rev. Accel. Beams **24**, 010701 (2021).

[45] S. Kerbstadt, K. Eickhoff, T. Bayer, and M. Wollenhaupt, Control of free electron wave packets by polarization-tailored ultrashort bichromatic laser fields, Adv. Phys. X **4**, 1672583 (2019).

[46] G. Penco, G. Perosa, E. Allaria, L. Badano, F. Bencivenga *et al.*, Nonlinear harmonics of a seeded free-electron laser as a coherent and ultrafast probe to investigate matter at the water window and beyond, Phys. Rev. A **105**, 053524 (2022).

[47] E. Allaria, F. Curbis, M. Coreno, M. Danailov, B. Diviacco *et al.*, Experimental characterization of nonlinear harmonic generation in planar and helical undulators, Phys. Rev. Lett. **100**, 174801 (2008).

[48] H.-D. Nuhn, S. Anderson, Y. Ding, Z. Huang, M. Ilchen *et al.*, Commissioning of the delta polarizing undulator at LCLS, in *Proceedings of FEL2015, Daejeon, Korea* (JACoW, United States, 2015).

[49] L. Allen, M. W. Beijersbergen, R. J. C. Spreeuw, and J. P. Woerdman, Orbital angular momentum of light and the transformation of Laguerre-Gaussian laser modes, Phys. Rev. A **45**, 8185 (1992).

[50] P. Rebernik Ribič, B. Rösner, D. Gauthier, E. Allaria, F. Döring *et al.*, Extreme-ultraviolet vortices from a free-electron laser, Phys. Rev. X **7**, 031036 (2017).

[51] P. Emma, R. Akre, J. Arthur, R. Bionta, C. Bostedt, J. Bozek, A. Brachmann *et al.*, First lasing and operation of an ångstrom-wavelength free-electron laser, Nat. Photon. **4**, 641 (2010).

[52] Y. Ding, K. L. F. Bane, W. Colocho, F.-J. Decker, P. Emma *et al.*, Beam shaping to improve the free-electron laser performance at the linac coherent light source, Phys. Rev. Accel. Beams **19**, 100703 (2016).

[53] P. Emma, K. Bane, M. Cornacchia, Z. Huang, H. Schlarb, G. Stupakov, and D. Walz, Femtosecond and subfemtosecond x-ray pulses from a self-amplified spontaneous-emission-based free-electron laser, Phys. Rev. Lett. **92**, 074801 (2004).

[54] Y. Ding, C. Behrens, R. Coffee, F.-J. Decker, P. Emma *et al.*, Generating femtosecond x-ray pulses using an emittance-spoiling foil in free-electron lasers, Appl. Phys. Lett. **107**, 191104 (2015).

[55] A. A. Lutman, T. J. Maxwell, J. P. MacArthur, M. W. Guetg *et al.*, Fresh-slice multicolour x-ray free-electron lasers, Nat. Photon. **10**, 745 (2016).

[56] A. A. Lutman, M. W. Guetg, T. J. Maxwell, J. P. MacArthur, Y. Ding, C. Emma, J. Krzywinski, A. Marinelli, and Z. Huang, High-power femtosecond soft x rays from fresh-slice multistage free-electron lasers, Phys. Rev. Lett. **120**, 264801 (2018).

[57] W. Qin, Y. Ding, A. A. Lutman, and Y.-C. Chao, Matching-based fresh-slice method for generating two-color x-ray free-electron lasers, Phys. Rev. Accel. Beams **20**, 090701 (2017).

[58] M. W. Guetg, A. A. Lutman, Y. Ding, T. J. Maxwell, and Z. Huang, Dispersion-based fresh-slice scheme for free-electron lasers, Phys. Rev. Lett. **120**, 264802 (2018).

[59] S. Huang, Y. Ding, Y. Feng, E. Hemsing, Z. Huang *et al.*, Generating single-spike hard x-ray pulses with nonlinear bunch compression in free-electron lasers, Phys. Rev. Lett. **119**, 154801 (2017).

[60] E. A. Schneidmiller and M. V. Yurkov, Obtaining high degree of circular polarization at x-ray free-electron lasers via a reverse undulator taper, Phys. Rev. ST Accel. Beams **16**, 110702 (2013).

[61] J. P. MacArthur, A. A. Lutman, J. Krzywinski, and Z. Huang, Microbunch rotation and coherent undulator radiation from a kicked electron beam, Phys. Rev. X **8**, 041036 (2018).

[62] A. A. Lutman, R. Coffee, Y. Ding, Z. Huang, J. Krzywinski, T. Maxwell, M. Messerschmidt, and H. D. Nuhn, Experimental demonstration of femtosecond two-color x-ray free-electron lasers, Phys. Rev. Lett. **110**, 134801 (2013).

[63] M. Ilchen, L. Glaser, F. Scholz, P. Walter, S. Deinert *et al.*, Angular momentum sensitive two-center interference, Phys. Rev. Lett. **112**, 023001 (2014).

[64] H.-D. Nuhn, Polarizing afterburner for the LCLS-II undulator line, in *Proceedings of the FEL'19*, Free Electron Laser Conference (JACoW Publishing, Geneva, Switzerland, 2019), pp. 560–563.

[65] G. Hartmann, A. Lindahl, A. Knie, N. Hartmann, A. Lutman *et al.*, Circular dichroism measurements at an x-ray free-electron laser with polarization control, Rev. Sci. Instrum. **87**, 083113 (2016).

[66] W. Ackermann *et al.*, Operation of a free-electron laser from the extreme ultraviolet to the water window, Nat. Photon. **1**, 336 (2007).

[67] K. Tiedtke, A. Azima, N. Von Bargen, L. Bittner, S. Bonfigt *et al.*, The soft x-ray free-electron laser flash at desy: beamlines, diagnostics and end-stations, New J. Phys. **11**, 023029 (2009).

[68] E. Schneidmiller, and M. V. Yurkov, Reverse undulator tapering for polarization control and background-free harmonic production in XFELs: Results from FLASH, in *Proceedings of the International Free Electron Laser Conference (FEL'17)*, International Free Electron Laser Conference (JACoW, Geneva, Switzerland, 2018), pp. 106–108.

[69] Y. Ivanyushenkov *et al.*, Conceptual design of a novel SCAPE undulator, in *Proceedings of the International Particle Accelerator Conference (IPAC'17)*, International Particle Accelerator Conference (JACoW, Geneva, Switzerland, 2017), pp. 1596–1598.

[70] E. Prat, M. Calvi, and S. Reiche, Generation of ultra-large-bandwidth x-ray free-electron-laser pulses with a transverse-gradient undulator, J. Synchrotron Radiat. **23**, 874 (2016).

[71] Y. Li, R. Lindberg, and K.-J. Kim, Transverse gradient undulator in a storage ring x-ray free electron laser oscillator, Phys. Rev. Accel. Beams **26**, 030702 (2023).

[72] E. Prat, M. Calvi, R. Ganter, S. Reiche, T. Schietinger *et al.*, Undulator beamline optimization with integrated chicanes for x-ray free-electron-laser facilities, J. Synchrotron Radiat. **23**, 861 (2016).

[73] E. Prat, E. Ferrari, M. Calvi, R. Ganter, S. Reiche *et al.*, Demonstration of a compact x-ray free-electron laser using the optical klystron effect, Appl. Phys. Lett. **119**, 151102 (2021).

[74] N. R. Thompson, D. Dunning, and B. McNeil, Improved temporal coherence in SASE FELs, in *Proceedings of the 1st International Particle Accelerator Conference: IPAC 2010* (Kyoto, Japan, 2010).

[75] J. Wu, A. Marinelli, and C. Pellegrini, Generation of longitudinally coherent ultra high power x-ray FEL pulses by phase and amplitude mixing, in *Proceedings of the FEL'12* (JACoW Publishing, Geneva, Switzerland, 2012), pp. 237–240.

[76] J. Wu, C. Pellegrini, A. Marinelli, H.-D Nuhn, F.-J Decker, H. Loos, A. Lutman, D. Ratner, Y. Feng, J. Krzywinski, D. Zhang, and D. Zhu, X-ray spectra and peak power control with ISASE, in *Proceedings of the 4th International Particle Accelerator Conference: IPAC 2013* (Shanghai, China, 2013), pp. 2068–2070.

[77] B. W. J. McNeil, N. R. Thompson, and D. J. Dunning, Transform-limited x-ray pulse generation from a

high-brightness self-amplified spontaneous-emission free-electron laser, Phys. Rev. Lett. **110**, 134802 (2013).

[78] E. Prat, W. Hu, C. Arrell, M. Calvi, P. Dijkstal, R. Follath, and S. Reiche, Experimental demonstration of mode-coupled and high-brightness self-amplified spontaneous emission in an x-ray free-electron laser, Phys. Rev. Lett. **133**, 205001 (2024).

[79] R. Bonifacio, C. Pellegrini, and L. Narducci, Collective instabilities and high-gain regime in a free-electron laser, Opt. Commun. **50**, 373 (1984).

[80] R. Bonifacio, N. Piovella, and B. W. J. McNeil, Superradiant evolution of radiation pulses in a free-electron laser, Phys. Rev. A **44**, R3441 (1991).

[81] E. Prat, F. Löhl, and S. Reiche, Efficient generation of short and high-power x-ray free-electron-laser pulses based on superradiance with a transversely tilted beam, Phys. Rev. ST Accel. Beams **18**, 100701 (2015).

[82] G. Wang, P. Dijkstal, S. Reiche, K. Schnorr, and E. Prat, Millijoule femtosecond x-ray pulses from an efficient fresh-slice multistage free-electron laser, Phys. Rev. Lett. **132**, 035002 (2024).

[83] G. Stupakov, Using the beam-echo effect for generation of short-wavelength radiation, Phys. Rev. Lett. **102**, 074801 (2009).

[84] E. Prat, A. Al Haddad, C. Arrell, S. Augustin, M. Boll *et al.*, An x-ray free-electron laser with a highly configurable undulator and integrated chicanes for tailored pulse properties, Nat. Commun. **14**, 5069 (2023).

[85] S. Abeghyan, M. Bagha-Shanjani, G. Chen, U. Englisch, S. Karabekyan *et al.*, First operation of the SASE1 undulator system of the European x-ray free-electron laser, J. Synchrotron Radiat. **26**, 302 (2019).

[86] R. Abela, A. Alarcon, J. Alex, C. Arrell, V. Arsov *et al.*, The SwissFEL soft x-ray free-electron laser beamline: Athos, J. Synchrotron Radiat. **26**, 1073 (2019).

[87] E. Saldin, E. Schneidmiller, and M. Yurkov, Fast: A three-dimensional time-dependent FEL simulation code, Nucl. Instrum. Methods Phys. Res. A **429**, 233 (1999).

[88] T. Tanaka, SIMPLEX: simulator and postprocessor for free-electron laser experiments, J. Synchrotron Radiat. **22**, 1319 (2015).

[89] T. Wei, P. Li, Y. Li, and J. Pflueger, Radiation properties of the SASE3 afterburner for European XFEL, in *Advances in X-ray Free-Electron Lasers Instrumentation IV*, edited by T. Tschentscher and L. Patthey, International Society for Optics and Photonics Vol. 10237 (SPIE, Bellingham, WA, 2017), p. 102370J.

[90] S. Karabekyan, S. Abeghyan, M. Bagha-Shanjani, S. Casalbuoni, U. Englisch *et al.*, SASE3 variable polarization project at the European XFEL, in *Proceedings of the IPAC'21*, International Particle Accelerator Conference (JACoW Publishing, Geneva, Switzerland, 2021), pp. 1678–1680.

[91] S. Karabekyan *et al.*, The status of the SASE3 variable polarization project at the European XFEL, in *Proceedings of the 13th International Particle Accelerator Conference (IPAC'22)*, International Particle Accelerator Conference (JACoW Publishing, Geneva, Switzerland, 2022), pp. 1029–1032.

[92] O. Chubar, P. Elleaume, and J. Chavanne, A three-dimensional magnetostatics computer code for insertion devices, J. Synchrotron Radiat. **5**, 481 (1998).

[93] S. Sasaki and I. McNulty, Proposal for generating brilliant x-ray beams carrying orbital angular momentum, Phys. Rev. Lett. **100**, 124801 (2008).

[94] E. Hemsing, Coherent photons with angular momentum in a helical afterburner, Phys. Rev. Accel. Beams **23**, 020703 (2020).

[95] S. Serkez, G. A. Geloni, V. Kocharyan, and E. Saldin, Circular polarization opportunities at the SASE3 undulator line of the European XFEL, arXiv:1608.08175.

[96] S. Serkez, A. Trebushinin, M. Veremchuk, and G. Geloni, Method for polarization shaping at free-electron lasers, Phys. Rev. Accel. Beams **22**, 110705 (2019).

[97] D. Ratner, R. Abela, J. Amann, C. Behrens, D. Bohler *et al.*, Experimental demonstration of a soft x-ray self-seeded free-electron laser, Phys. Rev. Lett. **114**, 054801 (2015).

[98] E. Schneidmiller and M. V. Yurkov, Reverse undulator tapering for polarization control and background-free harmonic production in XFELs: Results from FLASH, in *Proceedings of the International Free Electron Laser Conference (FEL'17)*, International Free Electron Laser Conference (JACoW, Geneva, Switzerland, 2018), pp. 106–108.

[99] Z. T. Zhao, Progress in SDUV-FEL and development of x-ray FELs in Shanghai, in *Proceedings of the FEL'10* (JACoW Publishing, Geneva, Switzerland, 2010), pp. 15–19.

[100] Z. Zhao, D. Wang, Q. Gu, L. Yin, M. Gu *et al.*, Status of the SXFEL facility, Appl. Sci. **7**, 607 (2017).

[101] Z. Zhu, Z. T. Zhao, D. Wang, Z. H. Yang, and L. Yin, SCLF: An 8-GeV CW SCRF Linac-based x-ray FEL facility in Shanghai, in *Proceedings of the FEL'17* (JACoW Publishing, Geneva, Switzerland, 2017), pp. 182–184.

[102] H. Deng, T. Zhang, L. Feng, C. Feng, B. Liu *et al.*, Polarization switching demonstration using crossed-planar undulators in a seeded free-electron laser, Phys. Rev. ST Accel. Beams **17**, 020704 (2014).

[103] L. Feng, H.-X. Deng, T. Zhang, C. Feng, J.-H. Chen *et al.*, Single-shot measurement of free-electron laser polarization at SDUV-FEL, Chin. Phys. C **39**, 028101 (2015).

[104] Z. Liu, H. Deng, and B. Liu, Design, construction and offline calibration for the prototype of arpolar instrument in SXFEL user facility, Radiat. Detect. Technol. Methods **6**, 1 (2022).

[105] Z. Liu, B. Deng, H. Deng, and B. Liu, Numerical study of transverse position monitor and compensation for x-ray polarization diagnosis, Rev. Sci. Instrum. **92**, 113104 (2021).

[106] B. Ritchie, Theoretical studies in photoelectron spectroscopy. molecular optical activity in the region of continuous absorption and its characterization by the angular distribution of photoelectrons, Phys. Rev. A **12**, 567 (1975).

[107] N. Böwering, T. Lischke, B. Schmidtke, N. Müller, T. Khalil *et al.*, Asymmetry in photoelectron emission from chiral molecules induced by circularly polarized light, Phys. Rev. Lett. **86**, 1187 (2001).

[108] S. Beaulieu, A. Comby, B. Fabre, D. Descamps, A. Ferré *et al.*, Probing ultrafast dynamics of chiral molecules using time-resolved photoelectron circular dichroism, Faraday Discuss. **194**, 325 (2016).

[109] M. Ilchen, G. Hartmann, P. Rupprecht, A. N. Artemyev, R. N. Coffee *et al.*, Emitter-site-selective photoelectron circular dichroism of trifluoromethyloxirane, Phys. Rev. A **95**, 053423 (2017).

[110] M. Ilchen, P. Schmidt, N. M. Novikovskiy, G. Hartmann, P. Rupprecht *et al.*, Site-specific interrogation of an ionic chiral fragment during photolysis using an x-ray free-electron laser, Commun. Chem. **4**, 119 (2021).

[111] D. Faccialà, M. Devetta, S. Beauvarlet, N. Besley, F. Calegari, C. Callegari *et al.*, Time-resolved chiral x-ray photoelectron spectroscopy with transiently enhanced atomic site selectivity: A free-electron laser investigation of electronically excited fenchone enantiomers, Phys. Rev. X **13**, 011044 (2023).

[112] F. Allum, V. Music, L. Inhester, R. Boll, B. Erk *et al.*, A localized view on molecular dissociation via electron-ion partial covariance, Commun. Chem. **5**, 42 (2022).

[113] R. Dörner, V. Mergel, O. Jagutzki, L. Spielberger, J. Ullrich *et al.*, Cold target recoil ion momentum spectroscopy: A "momentum microscope" to view atomic collision dynamics, Phys. Rep. **330**, 95 (2000).

[114] J. Ullrich, R. Moshammer, A. Dorn, R. Dörner, L. P. H. Schmidt *et al.*, Recoil-ion and electron momentum spectroscopy: Reaction-microscopes, Rep. Prog. Phys. **66**, 1463 (2003).

[115] M. Pitzer, M. Kunitski, A. S. Johnson, T. Jahnke, H. Sann *et al.*, Direct determination of absolute molecular stereochemistry in gas phase by Coulomb explosion imaging, Science **341**, 1096 (2013).

[116] A. Knie, M. Ilchen, P. Schmidt, P. Reiß, C. Ozga *et al.*, Angle-resolved study of resonant Auger decay and fluorescence emission processes after core excitations of the terminal and central nitrogen atoms in, Phys. Rev. A **90**, 013416 (2014).

[117] H. N. Chapman, A. Barty, M. J. Bogan, S. Boutet, M. Frank *et al.*, Femtosecond diffractive imaging with a soft-x-ray free-electron laser, Nat. Phys. **2**, 839 (2006).

[118] H. N. Chapman, P. Fromme, A. Barty, T. A. White, R. A. Kirian *et al.*, Femtosecond x-ray protein nanocrystallography, Nature (London) **470**, 73 (2011).

[119] C. Weninger, M. Purvis, D. Ryan, R. A. London, J. D. Bozek *et al.*, Stimulated electronic x-ray Raman scattering, Phys. Rev. Lett. **111**, 233902 (2013).

[120] D. W. Chandler and P. L. Houston, Two-dimensional imaging of state-selected photodissociation products detected by multiphoton ionization, J. Chem. Phys. **87**, 1445 (1987).

[121] A. T. J. B. Eppink and D. H. Parker, Velocity map imaging of ions and electrons using electrostatic lenses: Application in photoelectron and photofragment ion imaging of molecular oxygen, Rev. Sci. Instrum. **68**, 3477 (1997).

[122] D. H. Parker and A. T. J. B. Eppink, *Velocity Map Imaging: Applications in Molecular Dynamics and Experimental Aspects* (Cambridge University Press, Cambridge, UK, 2003), pp. 20–64.

[123] R. Wester, Velocity map imaging of ion–molecule reactions, Phys. Chem. Chem. Phys. **16**, 396 (2014).

[124] M. Lampton, O. Siegmund, and R. Raffanti, Delay line anodes for microchannel-plate spectrometers, Rev. Sci. Instrum. **58**, 2298 (1987).

[125] K. A. Hanold, A. K. Luong, T. G. Clements, and R. E. Continetti, Photoelectron-multiple-photofragment coincidence spectrometer, Rev. Sci. Instrum. **70**, 2268 (1999).

[126] D. A. Debrah, G. A. Stewart, G. Basnayake, A. Nomerotski, P. Svihra *et al.*, Developing a camera-based 3D momentum imaging system capable of 1 Mhits/s, Rev. Sci. Instrum. **91**, 023316 (2020).

[127] M. Fisher-Levine, R. Boll, F. Ziaee, C. Bomme, B. Erk *et al.*, Time-resolved ion imaging at free-electron lasers using timepixcam, J. Synchrotron Radiat. **25**, 336 (2018).

[128] T. Osipov, C. Bostedt, J. C. Castagna, K. R. Ferguson, M. Bucher *et al.*, The lamp instrument at the linac coherent light source free-electron laser, Rev. Sci. Instrum. **89**, 035112 (2018).

[129] B. Erk, J. P. Müller, C. Bomme, R. Boll, G. Brenner *et al.*, Camp@flash: An end-station for imaging, electron- and ion-spectroscopy, and pump–probe experiments at the flash free-electron laser, J. Synchrotron Radiat. **25**, 1529 (2018).

[130] P. O'Keeffe, V. Feyer, P. Bolognesi, M. Coreno, C. Callegari *et al.*, A velocity map imaging apparatus for gas phase studies at FERMI@elettra, Nuclear Instrum. Methods Phys. Res. B **284**, 69 (2012).

[131] S. Li, E. G. Champenois, R. Coffee, Z. Guo, K. Hegazy *et al.*, A co-axial velocity map imaging spectrometer for electrons, AIP Adv. **8**, 115308 (2018).

[132] T. Jahnke, T. Weber, T. Osipov, A. L. Landers, O. Jagutzki *et al.*, Multicoincidence studies of photo and Auger electrons from fixed-in-space molecules using the COLTRIMS technique, J. Electron Spectrosc. Relat. Phenom. **141**, 229 (2004).

[133] G. Kastirke, M. S. Schöffler, M. Weller, J. Rist, R. Boll *et al.*, Double core-hole generation in o2 molecules using an x-ray free-electron laser: Molecular-frame photoelectron angular distr, Phys. Rev. Lett. **125**, 163201 (2020).

[134] X. Li, L. Inhester, T. Osipov, R. Boll, R. Coffee *et al.*, Electron-ion coincidence measurements of molecular dynamics with intense x-ray pulses, Sci. Rep. **11**, 505 (2021).

[135] T. Jahnke, R. Guillemin, L. Inhester, S.-K. Son, G. Kastirke *et al.*, Inner-shell-ionization-induced femtosecond structural dynamics of water molecules imaged at an x-ray free-electron laser, Phys. Rev. X **11**, 041044 (2021).

[136] G. Kastirke, M. S. Schöffler, M. Weller, J. Rist, R. Boll *et al.*, Photoelectron diffraction imaging of a molecular breakup using an x-ray free-electron laser, Phys. Rev. X **10**, 021052 (2020).

[137] P. Walter, A. Kamalov, A. Gatton, T. Driver, D. Bhogadi *et al.*, Multi-resolution electron spectrometer array for future free-electron laser experiments, J. Synchrotron Radiat. **28**, 1364 (2021).

[138] M. Ilchen, G. Hartmann, E. Gryzlova, A. Achner, E. Allaria *et al.*, Symmetry breakdown of electron emission in extreme ultraviolet photoionization of argon, Nat. Commun. **9**, 4659 (2018).

[139] A. De Fanis, M. Ilchen, A. Achner, T. M. Baumann, R. Boll *et al.*, High-resolution electron time-of-flight spectrometers for angle-resolved measurements at the SQS instrument at the European XFEL, J. Synchrotron Rad. **29**, 755 (2022).

[140] G. Hartmann, M. Ilchen, P. Schmidt, C. Küstner-Wetekam, C. Ozga *et al.*, Recovery of high-energy photoelectron circular dichroism through Fano interference, Phys. Rev. Lett. **123**, 043202 (2019).

[141] A. Rijs, E. Backus, C. de Lange, N. Westwood, and M. Janssen, "Magnetic bottle" spectrometer as a versatile tool for laser photoelectron spectroscopy, J. Electron Spectrosc. Relat. Phenom. **112**, 151 (2000).

[142] A. Matsuda, M. Fushitani, C. M. Tseng, Y. Hikosaka, J. H. Eland *et al.*, A magnetic-bottle multi-electron-ion coincidence spectrometer, Rev. Sci. Instrum. **82**, 103105 (2011).

[143] M. N. Pohl, S. Malerz, F. Trinter, C. Lee, C. Kolbeck *et al.*, Photoelectron circular dichroism in angle-resolved photoemission from liquid fenchone, Phys. Chem. Chem. Phys. **24**, 8081 (2022).

[144] V. Ulrich, S. Barth, S. Joshi, U. Hergenhahn, E. Mikajlo *et al.*, Giant chiral asymmetry in the C 1*s* core level photoemission from randomly oriented fenchone enantiomers, J. Phys. Chem. A **112**, 3544 (2008).

[145] A. Sanchez-Gonzalez, P. Micaelli, C. Olivier, T. Barillot, M. Ilchen *et al.*, Accurate prediction of x-ray pulse properties from a free-electron laser using machine learning, Nat. Commun. **8**, 15461 (2017).

[146] K. Dingel, T. Otto, L. Marder, L. Funke, A. Held *et al.*, Artificial intelligence for online characterization of ultrashort x-ray free-electron laser pulses, Sci. Rep. **12**, 17809 (2022).

[147] P. Juranić, J. Rehanek, C. A. Arrell, C. Pradervand, R. Ischebeck *et al.*, SwissFEL aramis beamline photon diagnostics, J. Synchrotron Radiat. **25**, 1238 (2018).

[148] S. Moeller, J. Arthur, A. Brachmann, R. Coffee, F.-J. Decker *et al.*, Photon beamlines and diagnostics at LCLS, Nucl. Instrum. Methods Phys. Res. Sect. A **635**, S6 (2011).

[149] M. Zangrando, A. Abrami, D. Cocco, C. Fava, S. Gerusina *et al.*, The photon beam transport and diagnostics system at FERMI@ Elettra, the italian seeded FEL source: Commissioning experience and most recent results, in *x-ray Free-Electron Lasers: Beam Diagnostics, Beamline Instrumentation, and Applications* (SPIE, Bellingham, WA, 2012), Vol. 8504, pp. 12–19.

[150] J. Grünert, M. P. Carbonell, F. Dietrich, T. Falk, W. Freund *et al.*, x-ray photon diagnostics at the European XFEL, J. Synchrotron Radiat. **26**, 1422 (2019).

[151] K. Tono, T. Togashi, Y. Inubushi, T. Katayama, S. Owada *et al.*, Overview of optics, photon diagnostics and experimental instruments at SACLA: Development, operation and scientific applications, in *Advances in x-ray Free-Electron Lasers Instrumentation IV* (SPIE, Bellingham, WA, 2017), Vol. 10237, p. 1023706.

[152] K. Li, J. Laksman, T. Mazza, G. Doumy, D. Koulentianos *et al.*, Ghost-imaging-enhanced noninvasive spectral characterization of stochastic x-ray free-electron-laser pulses, Commun. Phys. **5**, 191 (2022).

[153] G. Brenner, S. Kapitzki, M. Kuhlmann, E. Ploenjes, T. Noll *et al.*, First results from the online variable line spacing grating spectrometer at flash, Nucl. Instrum. Methods Phys. Res. Sect. A **635**, S99 (2011).

[154] K. Tiedtke, J. Feldhaus, U. Hahn, U. Jastrow, T. Nunez *et al.*, Gas detectors for x-ray lasers, J. Appl. Phys. **103**, 094511 (2008).

[155] B. Keitel, E. Plönjes, S. Kreis, M. Kuhlmann, K. Tiedtke *et al.*, Hartmann wavefront sensors and their application at flash, J. Synchrotron Radiat. **23**, 43 (2016).

[156] M. Zangrando, D. Cocco, C. Fava, S. Gerusina, R. Gobessi *et al.*, Recent results of padres, the photon analysis delivery and reduction system, from the FERMI FEL commissioning and user operations, J. Synchrotron Radiat. **22**, 565 (2015).

[157] M. Seaberg, R. Cojocaru, S. Berujon, E. Ziegler, A. Jaggi *et al.*, Wavefront sensing at x-ray free-electron lasers, J. Synchrotron Radiat. **26**, 1115 (2019).

[158] Y. Kayser, S. Rutishauser, T. Katayama, H. Ohashi, T. Kameshima *et al.*, Wavefront metrology measurements at SACLA by means of x-ray grating interferometry, Opt. Express **22**, 9004 (2014).

[159] P. Craievich, M. Bopp, H. Braun, R. Ganter, T. Kleeb *et al.*, Status of the Polarix-TDS project, in *Proceedings of the IPAC'18* (JACoW Publishing, Geneva, Switzerland, 2018), pp. 3808–3811.

[160] M. Vogt, B. Faatz, J. Feldhaus, K. Honkavaara, S. Schreiber *et al.*, Status of the free-electron laser FLASH at desy, in *Proceedings of IPAC2011, San Sebastián, Spain* (2011).

[161] C. Behrens, F.-J. Decker, Y. Ding, V. Dolgashev, J. Frisch *et al.*, Few-femtosecond time-resolved measurements of x-ray free-electron lasers, Nat. Commun. **5**, 3762 (2014).

[162] E. Ferrari, E. Allaria, J. Buck, G. De Ninno, B. Diviacco *et al.*, Single shot polarization characterization of XUV FEL pulses from crossed polarized undulators, Sci. Rep. **5**, 1 (2015).

[163] T. Mazza, M. Ilchen, A. J. Rafipoor, C. Callegari, P. Finetti *et al.*, Determining the polarization state of an extreme ultraviolet free-electron laser beam using atomic circular dichroism, Nat. Commun. **5**, 3648 (2014).

[164] M. Ilchen, N. Douguet, T. Mazza, A. J. Rafipoor, C. Callegari *et al.*, Circular dichroism in multiphoton ionization of resonantly excited He^+ ions, Phys. Rev. Lett. **118**, 013002 (2017).

[165] S. Krinsky and R. Gluckstern, Analysis of statistical correlations and intensity spiking in the self-amplified spontaneous-emission free-electron laser, Phys. Rev. Special Topics—Accel. Beams **6**, 050701 (2003).

[166] J. Itatani, F. Quéré, G. L. Yudin, M. Y. Ivanov, F. Krausz, and P. B. Corkum, Attosecond streak camera, Phys. Rev. Lett. **88**, 173903 (2002).

[167] R. Kienberger, M. Hentschel, M. Uiberacker, C. Spielmann, M. Kitzler *et al.*, Steering attosecond electron wave packets with light, Science **297**, 1144 (2002).

[168] P. Eckle, M. Smolarski, P. Schlup, J. Biegert, A. Staudte *et al.*, Attosecond angular streaking, Nat. Phys. **4**, 565 (2008).

[169] S. Li, Z. Guo, R. N. Coffee, K. Hegazy, Z. Huang *et al.*, Characterizing isolated attosecond pulses with angular streaking, Opt. Express **26**, 4531 (2018).

[170] M. Kitzler, N. Milosevic, A. Scrinzi, F. Krausz, and T. Brabec, Quantum theory of attosecond XUV pulse measurement by laser dressed photoionization, Phys. Rev. Lett. **88**, 173904 (2002).

[171] P. Anderson, More is different—Broken symmetry and nature of hierarchical structure of science, Science **177**, 393 (1972).

[172] L. Ye, J. R. Rouxel, S. Asban, B. Rosner, and S. Mukamel, Probing molecular chirality by orbital-angular-momentum-carrying x-ray pulses, J. Chem. Theory Comput. **15**, 4180 (2019).

[173] L. Ye, L. Yang, X. Zheng, and S. Mukamel, Enhancing circular dichroism signals with vector beams, Phys. Rev. Lett. **126**, 123001 (2021).

[174] Y. Zhang, J. R. Rouxel, J. Autschbach, N. Govind, and S. Mukamel, x-ray circular dichroism signals: a unique probe of local molecular chirality, Chem. Sci. **8**, 5969 (2017).

[175] J. R. Rouxel, M. Kowalewski, and S. Mukamel, Photoinduced molecular chirality probed by ultrafast resonant x-ray spectroscopy, Struct. Dyn. **4**, 044006 (2017).

[176] P. O'Keeffe, R. López-Martens, J. Mauritsson, A. Johansson, A. L'Huillier *et al.*, Polarization effects in two-photon nonresonant ionization of argon with extreme-ultraviolet and

infrared femtosecond pulses, Phys. Rev. A **69**, 051401(R) (2004).
[177] S. Aloïse, P. O'Keeffe, D. Cubaynes, M. Meyer, and A. N. Grum-Grzhimailo, Photoionization of synchrotron-radiation-excited atoms: Separating partial cross sections by full polarization control, Phys. Rev. Lett. **94**, 223002 (2005).
[178] M. Meyer, A. N. Grum-Grzhimailo, D. Cubaynes, Z. Felfli, E. Heinecke, S. T. Manson, and P. Zimmermann, Magnetic dichroism in k-shell photoemission from laser excited li atoms, Phys. Rev. Lett. **107**, 213001 (2011).
[179] P. Lambropoulos, Multiphoton ionization of one-electron atoms with circularly polarized light, Phys. Rev. Lett. **29**, 453 (1972).
[180] A. K. Kazansky, A. V. Grigorieva, and N. M. Kabachnik, Circular dichroism in laser-assisted short-pulse photoionization, Phys. Rev. Lett. **107**, 253002 (2011).
[181] N. Kabachnik, Excitation and ionization of polarized atoms, J. Electron Spectrosc. Relat. Phenom. **79**, 269 (1996).
[182] T. E. Glover, R. W. Schoenlein, A. H. Chin, and C. V. Shank, Observation of laser assisted photoelectric effect and femtosecond high order harmonic radiation, Phys. Rev. Lett. **76**, 2468 (1996).
[183] M. Meyer, P. Radcliffe, T. Tschentscher, J. T. Costello, A. L. Cavalieri *et al.*, Angle-resolved electron spectroscopy of laser-assisted Auger decay induced by a few-femtosecond x-ray pulse, Phys. Rev. Lett. **108**, 063007 (2012).
[184] T. Mazza, E. Gryzlova, A. Grum-Grzhimailo, A. Kazansky, N. Kabachnik *et al.*, Dichroism in the photoionisation of atoms at XUV free-electron lasers, J. Electron Spectrosc. Relat. Phenom. **204**, 313 (2015).
[185] M. Meyer, D. Cubaynes, D. Glijer, J. Dardis, P. Hayden *et al.*, Polarization control in two-color above-threshold ionization of atomic helium, Phys. Rev. Lett. **101**, 193002 (2008).
[186] T. Mazza, M. Ilchen, A. Rafipoor, C. Callegari, P. Finetti *et al.*, Angular distribution and circular dichroism in the two-colour XUV+NIR above-threshold ionization of helium, J. Mod. Opt. **63**, 367 (2016).
[187] R. Wagner, *Atoms and Molecules in Strong Laser Fields*, PhD. thesis, University of Hamburg (2022).
[188] A. N. Grum-Grzhimailo, N. Douguet, M. Meyer, and K. Bartschat, Two-color XUV plus near-IR multiphoton near-threshold ionization of the helium ion by circularly polarized light in the vicinity of the $3p$ resonance, Phys. Rev. A **100**, 033404 (2019).
[189] R. Freeman, *Handbook of Nuclear Magnetic Resonance* (John Wiley and Sons, New York, NY, 1987).
[190] S. Eckart, M. Kunitski, M. Richter, A. Hartung, J. Rist *et al.*, Ultrafast preparation and detection of ring currents in single atoms, Nat. Phys. **14**, 701 (2018).
[191] J. Hofbrucker, A. V. Volotka, and S. Fritzsche, Maximum elliptical dichroism in atomic two-photon ionization, Phys. Rev. Lett. **121**, 053401 (2018).
[192] A. N. Grum-Grzhimailo and E. V. Gryzlova, Nondipole effects in the angular distribution of photoelectrons in two-photon two-color above-threshold atomic ionization, Phys. Rev. A **89**, 043424 (2014).
[193] T. Mazza *et al.*, Resonant Raman Auger spectroscopy on transient core-excited Ne ions, J. Phys. B: At. Mol. Opt. Phys. **57**, 225001 (2024).
[194] C. S. Fadley, Angle-resolved x-ray photoelectron spectroscopy, Prog. Surf. Sci. **16**, 275 (1984).
[195] D. P. Woodruff and A. M. Bradshaw, Adsorbate structure determination on surfaces using photoelectron diffraction, Rep. Prog. Phys. **57**, 1029 (1994).
[196] A. V. Golovin, N. A. Cherepkov, and V. V. Kuznetsov, Photoionization of oriented molecules in a gas phase, Z. Phys. D **24**, 371 (1992).
[197] E. Shigemasa, J. Adachi, M. Oura, and A. Yagishita, Angular distributions of $1s\sigma$ photoelectrons from fixed-in-space N_2 molecules, Phys. Rev. Lett. **74**, 359 (1995).
[198] A. Landers, T. Weber, I. Ali, A. Cassimi, M. Hattass *et al.*, Photoelectron diffraction mapping: Molecules illuminated from within, Phys. Rev. Lett. **87**, 013002 (2001).
[199] H. Stapelfeldt and T. Seideman, Colloquium: Aligning molecules with strong laser pulses, Rev. Mod. Phys. **75**, 543 (2003).
[200] R. N. Zare, Photoejection dynamics, Mol. Photochem. **4**, 1 (1972).
[201] K. Fehre, N. M. Novikovskiy, S. Grundmann, G. Kastirke, S. Eckart *et al.*, Fourfold differential photoelectron circular dichroism, Phys. Rev. Lett. **127**, 103201 (2021).
[202] M. Tia, M. Pitzer, G. Kastirke, J. Gatzke, H.-K. Kim *et al.*, Observation of enhanced chiral asymmetries in the inner-shell photoionization of uniaxially oriented methyloxirane enantiomers, J. Phys. Chem. Lett. **8**, 2780 (2017).
[203] A. F. Ordonez and O. Smirnova, Propensity rules in photoelectron circular dichroism in chiral molecules. I. Chiral hydrogen, Phys. Rev. A **99**, 043416 (2019).
[204] S. Beaulieu, A. Comby, D. Descamps, B. Fabre, G. A. Garcia *et al.*, Photoexcitation circular dichroism in chiral molecules, Nat. Phys. **14**, 484 (2018).
[205] M. Waitz, R. Bello, D. Metz, J. Lower, F. Trinter *et al.*, Imaging the square of the correlated two-electron wave function of a hydrogen molecule, Nat. Commun. **8**, 2266 (2017).
[206] A. F. Ordonez and O. Smirnova, Generalized perspective on chiral measurements without magnetic interactions, Phys. Rev. A **98**, 063428 (2018).
[207] D. Ayuso, A. F. Ordonez, and O. Smirnova, Ultrafast chirality: The road to efficient chiral measurements, Phys. Chem. Chem. Phys. **24**, 26962 (2022).
[208] B. Ritchie, Theory of the angular distribution of photoelectrons ejected from optically active molecules and molecular negative ions, Phys. Rev. A **13**, 1411 (1976).
[209] I. Powis, Photoelectron circular dichroism of the randomly oriented chiral molecules glyceraldehyde and lactic acid, J. Chem. Phys. **112**, 301 (2000).
[210] M. H. M. Janssen and I. Powis, Detecting chirality in molecules by imaging photoelectron circular dichroism, Phys. Chem. Chem. Phys. **16**, 856 (2014).
[211] L. Nahon, G. A. Garcia, and I. Powis, Valence shell one-photon photoelectron circular dichroism in chiral systems, J. Electron Spectrosc. Relat. Phenom. **204**, 322 (2015).
[212] C. Lux, M. Wollenhaupt, T. Bolze, Q. Liang, J. Köhler, C. Sarpe, and T. Baumert, Circular dichroism in the photoelectron angular distributions of camphor and fenchone from multiphoton ionization with femtosecond laser pulses, Angew. Chem., Int. Ed. **51**, 5001 (2012).
[213] C. S. Lehmann, N. B. Ram, I. Powis, and M. H. M. Janssen, Imaging photoelectron circular dichroism of chiral molecules

by femtosecond multiphoton coincidence detection, J. Chem. Phys. **139**, 234307 (2013).
[214] N. Bhargava Ram, C. S. Lehmann, and M. H. M. Janssen, Probing chirality with a femtosecond reaction microscope, EPJ Web Conf. **41**, 02029 (2013).
[215] M. M. Rafiee Fanood, I. Powis, and M. H. M. Janssen, Chiral asymmetry in the multiphoton ionization of methyloxirane using femtosecond electron-ion coincidence imaging, J. Phys. Chem. A **118**, 11541 (2014).
[216] M. M. R. Fanood, N. B. Ram, C. S. Lehmann, I. Powis, and M. H. M. Janssen, Enantiomer-specific analysis of multicomponent mixtures by correlated electron imaging–ion mass spectrometry, Nat. Commun. **6**, 7511 (2015).
[217] C. Lux, M. Wollenhaupt, C. Sarpe, and T. Baumert, Photoelectron circular dichroism of bicyclic ketones from multiphoton ionization with femtosecond laser pulses, ChemPhysChem **16**, 115 (2015).
[218] C. Lux, A. Senftleben, C. Sarpe, M. Wollenhaupt, and T. Baumert, Photoelectron circular dichroism observed in the above-threshold ionization signal from chiral molecules with femtosecond laser pulses, J. Phys. B: Atom. Mol. Optic. Phys. **49**, 02LT01 (2015).
[219] A. Kastner, C. Lux, T. Ring, S. Züllighoven, C. Sarpe, A. Senftleben, and T. Baumert, Enantiomeric excess sensitivity to below one percent by using femtosecond photoelectron circular dichroism, ChemPhysChem **17**, 1119 (2016).
[220] J. Miles, D. Fernandes, A. Young, C. Bond, S. Crane, O. Ghafur, D. Townsend, J. Sá, and J. Greenwood, A new technique for probing chirality via photoelectron circular dichroism, Analytica Chimica Acta **984**, 134 (2017).
[221] A. Kastner, T. Ring, H. Braun, A. Senftleben, and T. Baumert, Observation of photoelectron circular dichroism using a nanosecond laser, ChemPhysChem **20**, 1416 (2019).
[222] S. T. Ranecky, G. B. Park, P. C. Samartzis, I. C. Giannakidis, D. Schwarzer, A. Senftleben, T. Baumert, and T. Schäfer, Detecting chirality in mixtures using nanosecond photoelectron circular dichroism, Phys. Chem. Chem. Phys. **24**, 2758 (2022).
[223] S. Beaulieu, A. Ferré, R. Géneaux, R. Canonge, D. Descamps *et al.*, Universality of photoelectron circular dichroism in the photoionization of chiral molecules, New J. Phys. **18**, 102002 (2016).
[224] A. Comby, S. Beaulieu, M. Boggio-Pasqua, D. Descamps, F. Légaré, L. Nahon, S. Petit, B. Pons, B. Fabre, Y. Mairesse, and V. Blanchet, Relaxation dynamics in photoexcited chiral molecules studied by time-resolved photoelectron circular dichroism: Toward chiral femtochemistry, J. Phys. Chem. Lett. **7**, 4514 (2016).
[225] V. Blanchet, D. Descamps, S. Petit, Y. Mairesse, B. Pons, and B. Fabre, Ultrafast relaxation investigated by photoelectron circular dichroism: An isomeric comparison of camphor and fenchone, Phys. Chem. Chem. Phys. **23**, 25612 (2021).
[226] P. V. Demekhin, A. N. Artemyev, A. Kastner, and T. Baumert, Photoelectron circular dichroism with two overlapping laser pulses of carrier frequencies ω and 2ω linearly polarized in two mutually orthogonal directions, Phys. Rev. Lett. **121**, 253201 (2018).
[227] P. V. Demekhin, Photoelectron circular dichroism with Lissajous-type bichromatic fields: One-photon versus two-photon ionization of chiral molecules, Phys. Rev. A **99**, 063406 (2019).
[228] S. Rozen, A. Comby, E. Bloch, S. Beauvarlet, D. Descamps, B. Fabre, S. Petit, V. Blanchet, B. Pons, N. Dudovich, and Y. Mairesse, Controlling subcycle optical chirality in the photoionization of chiral molecules, Phys. Rev. X **9**, 031004 (2019).
[229] A. F. Ordonez and O. Smirnova, Disentangling enantiosensitivity from dichroism using bichromatic fields, Phys. Chem. Chem. Phys. **24**, 7264 (2022).
[230] S. Beaulieu, A. Comby, A. Clergerie, J. Caillat, D. Descamps, N. Dudovich, B. Fabre, R. Géneaux, F. Légaré, S. Petit *et al.*, Attosecond-resolved photoionization of chiral molecules, Science **358**, 1288 (2017).
[231] A. F. Ordonez, D. Ayuso, P. Decleva, and O. Smirnova, Geometric magnetism and anomalous enantio-sensitive observables in photoionization of chiral molecules, Commun. Phys. **6**, 257 (2023).
[232] A. F. Ordonez, A. Roos, P. M. Maier, D. Ayuso, and O. Smirnova, Geometry of temporal chiral structures, arXiv:2409.02500.
[233] J. Vogwell, L. Rego, O. Smirnova, and D. Ayuso, Ultrafast control over chiral sum-frequency generation, Sci. Adv. **9**, eadj1429 (2023).
[234] D. Ayuso, A. F. Ordonez, M. Ivanov, and O. Smirnova, Ultrafast optical rotation in chiral molecules with ultrashort and tightly focused beams, Optica **8**, 1243 (2021).
[235] D. Ayuso, O. Neufeld, A. F. Ordonez, P. Decleva, G. Lerner *et al.*, Synthetic chiral light for efficient control of chiral light-matter interaction, Nat. Photon. **13**, 866 (2019).
[236] N. Mayer, D. Ayuso, P. Decleva, M. Khokhlova, E. Pisanty, M. Ivanov, and O. Smirnova, Chiral topological light for detection of robust enantiosensitive observables, Nat. Photon. **18**, 1155 (2024).
[237] D. Mayer, F. Lever, D. Picconi, J. Metje, S. Alisauskas, F. Calegari, S. Düsterer, C. Ehlert, R. Feifel, M. Niebuhr *et al.*, Following excited-state chemical shifts in molecular ultrafast x-ray photoelectron spectroscopy, Nat. Commun. **13**, 198 (2022).
[238] L. Cederbaum and J. Zobeley, Ultrafast charge migration by electron correlation, Chem. Phys. Lett. **307**, 205 (1999).
[239] A. I. Kuleff and L. S. Cederbaum, Charge migration in different conformers of glycine: The role of nuclear geometry, Chem. Phys. **338**, 320 (2007).
[240] A. I. Kuleff and A. Dreuw, Theoretical description of charge migration with a single Slater-determinant and beyond, J. Chem. Phys. **130**, 034102, (2009).
[241] R. Weinkauf, E. Schlag, T. Martinez, and R. Levine, Nonstationary electronic states and site-selective reactivity, J. Phys. Chem. A **101**, 7702 (1997).
[242] F. Remacle, R. D. Levine, E. W. Schlag, and R. Weinkauf, Electronic control of site selective reactivity: A model combining charge migration and dissociation, J. Phys. Chem. A **103**, 10149 (1999).
[243] F. Remacle and R. D. Levine, An electronic time scale in chemistry, Proc. Natl. Acad. Sci. USA **103**, 6793 (2006).
[244] F. Calegari, D. Ayuso, A. Trabattoni, L. Belshaw, S. De Camillis *et al.*, Ultrafast electron dynamics in phenylalanine initiated by attosecond pulses, Science **346**, 336 (2014).
[245] M. Lara-Astiaso, M. Galli, A. Trabattoni, A. Palacios, D. Ayuso *et al.*, Attosecond pump-probe spectroscopy of charge dynamics in tryptophan, J. Phys. Chem. Lett. **9**, 4570 (2018).

[246] E. P. Månsson, S. Latini, F. Covito, V. Wanie, M. Galli *et al.*, Real-time observation of a correlation-driven sub 3 fs charge migration in ionised adenine, Commun. Chem. **4**, 73 (2021).

[247] T. Barillot, O. Alexander, B. Cooper, T. Driver, D. Garratt *et al.*, Correlation-driven transient hole dynamics resolved in space and time in the isopropanol molecule, Phys. Rev. X **11**, 031048 (2021).

[248] D. T. Matselyukh, V. Despré, N. V. Golubev, A. I. Kuleff, and H. J. Wörner, Decoherence and revival in attosecond charge migration driven by non-adiabatic dynamics, Nat. Phys. **18**, 1206 (2022).

[249] V. Wanie, E. Bloch, E. P. Månsson, L. Colaizzi, K. Saraswathula, S. Ryabchuk, F. Légaré, A. Trabattoni, V. Blanchet, M.-C. Heitz *et al.*, Ultrafast chiroptical switching in UV-excited molecules, in *The International Conference on Ultrafast Phenomena (UP) 2022*, edited by F. Légaré, T. Tahara, J. Biegert, T. Brixner, and N. Dudovich, Technical Digest Series (Optica Publishing Group, 2022), paper W2B.3.

[250] G. De Ninno, J. Wätzel, P. R. Ribič, E. Allaria, M. Coreno *et al.*, Photoelectric effect with a twist, Nat. Photon. **14**, 554 (2020).

[251] J. Wätzel, P. Rebernik Ribič, M. Coreno, M. B. Danailov, C. David *et al.*, Light-induced magnetization at the nanoscale, Phys. Rev. Lett. **128**, 157205 (2022).

[252] J. Wätzel, Y. Pavlyukh, A. Schäffer, and J. Berakdar, Optical vortex driven charge current loop and optomagnetism in fullerenes, Carbon **99**, 439 (2016).

[253] J. Wätzel and J. Berakdar, Electrons in intense laser fields with local phase, polarization, and skyrmionic textures, Phys. Rev. A **102**, 063105 (2020).

[254] H. Fujita and M. Sato, Ultrafast generation of skyrmionic defects with vortex beams: Printing laser profiles on magnets, Phys. Rev. B **95**, 054421 (2017).

[255] G. D. Ninno (private communication).

[256] G. Gariepy, J. Leach, K. T. Kim, T. J. Hammond, E. Frumker, R. W. Boyd, and P. B. Corkum, Creating high-harmonic beams with controlled orbital angular momentum, Phys. Rev. Lett. **113**, 153901 (2014).

[257] H. He, M. E. J. Friese, N. R. Heckenberg, and H. Rubinsztein-Dunlop, Direct observation of transfer of angular momentum to absorptive particles from a laser beam with a phase singularity, Phys. Rev. Lett. **75**, 826 (1995).

[258] T. Kuga, Y. Torii, N. Shiokawa, T. Hirano, Y. Shimizu, and H. Sasada, Novel optical trap of atoms with a doughnut beam, Phys. Rev. Lett. **78**, 4713 (1997).

[259] M. P. J. Lavery, F. C. Speirits, S. M. Barnett, and M. J. Padgett, Detection of a spinning object using light's orbital angular momentum, Science **341**, 537 (2013).

[260] D. B. Phillips, M. P. Lee, F. C. Speirits, S. M. Barnett, S. H. Simpson, M. P. J. Lavery, M. J. Padgett, and G. M. Gibson, Rotational doppler velocimetry to probe the angular velocity of spinning microparticles, Phys. Rev. A **90**, 011801 (2014).

[261] J. Wang, J.-Y. Yang, I. M. Fazal, N. Ahmed, Y. Yan *et al.*, Terabit free-space data transmission employing orbital angular momentum multiplexing, Nat. Photon. **6**, 488 (2012).

[262] A. Jesacher, S. Fürhapter, S. Bernet, and M. Ritsch-Marte, Shadow effects in spiral phase contrast microscopy, Phys. Rev. Lett. **94**, 233902 (2005).

[263] F. Kong, C. Zhang, F. Bouchard, Z. Li, G. G. Brown *et al.*, Controlling the orbital angular momentum of high harmonic vortices, Nat. Commun. **8**, 14970 (2017).

[264] D. Gauthier, P. R. Ribič, G. Adhikary, A. Camper, C. Chappuis *et al.*, Tunable orbital angular momentum in high-harmonic generation, Nat. Commun. **8**, 14971 (2017).

[265] A. Denoeud, L. Chopineau, A. Leblanc, and F. Quéré, Interaction of ultraintense laser vortices with plasma mirrors, Phys. Rev. Lett. **118**, 033902 (2017).

[266] E. Hemsing and A. Marinelli, Echo-enabled x-ray vortex generation, Phys. Rev. Lett. **109**, 224801 (2012).

[267] P. R. Ribič, D. Gauthier, and G. De Ninno, Generation of coherent extreme-ultraviolet radiation carrying orbital angular momentum, Phys. Rev. Lett. **112**, 203602 (2014).

[268] M. Katoh, M. Fujimoto, H. Kawaguchi, K. Tsuchiya, K. Ohmi *et al.*, Angular momentum of twisted radiation from an electron in spiral motion, Phys. Rev. Lett. **118**, 094801 (2017).

[269] T. Kaneyasu, Y. Hikosaka, M. Fujimoto, T. Konomi, M. Katoh, H. Iwayama, and E. Shigemasa, Limitations in photoionization of helium by an extreme ultraviolet optical vortex, Phys. Rev. A **95**, 023413 (2017).

[270] J. M. Dahlström, D. Guénot, K. Klünder, M. Gisselbrecht, J. Mauritsson *et al.*, Theory of attosecond delays in laser-assisted photoionization, Chem. Phys. **414**, 53 (2013).

[271] A. W. Bray, D. Freeman, F. Naseem, V. K. Dolmatov, and A. S. Kheifets, Correlation-enhanced high-order-harmonic-generation spectra of Mn and Mn^+, Phys. Rev. A **101**, 053415 (2020).

[272] K. Jacobi, Y.-p. Hsu, and H. Rotermund, Photoemission from Ne, Ar, Kr, and Xe layers on Ni(110) and Ga films, Surface Science **114**, 683 (1982).

[273] B. Niedzielski, D. Schulz, and J. Berakdar, Spatio-temporal superconducting dynamics driven by THz fields from topological spintronic terahertz emitters, Sci. Rep. **12**, 15610 (2022).

[274] G. Perosa, J. Wätzel, D. Garzella, E. Allaria, M. Bonanomi *et al.*, Femtosecond polarization shaping of free-electron laser pulses, Phys. Rev. Lett. **131**, 045001 (2023).

[275] A. J. Miles and B. A. Wallace, Synchrotron radiation circular dichroism spectroscopy of proteins and applications in structural and functional genomics, Chem. Soc. Rev. **35**, 39 (2006).

[276] J. Kypr, I. Kejnovská, D. Renčiuk, and M. Vorléková, Circular dichroism and conformational polymorphism of dna, Nucleic Acids Res. **37**, 1713 (2009).

[277] M. Tanaka, K. Nakagawa, A. Agui, K. Fujii, and A. Yokoya, First observation of natural circular dichroism for biomolecules in soft-xray region studied with a polarizing undulator, Phys. Scr. 873, (2005).

[278] V. Kimberg and N. Kosugi, Calculation of *K*-edge circular dichroism of amino acids: Comparison of random phase approximation with other methods, J. Chem. Phys. **126**, 245101 (2007).

[279] N. J. Greenfield, Using circular dichroism collected as a function of temperature to determine the thermodynamics of protein unfolding and binding interactions, Nat. Protoc. **1**, 2527 (2006).

[280] N. Sreerama and R. W. Woody, Estimation of protein secondary structure from circular dichroism spectra: Comparison of CONTIN, SELCON, and CDSSTR methods with an expanded reference set, Anal. Biochem. **287**, 252 (2000).

[281] U. Boesl, A. Bornschlegl, C. Logé, and K. Titze, Resonance-enhanced multiphoton ionization with circularly polarized light: Chiral carbonyls, Anal. Bioanal. Chem. **405**, 6913 (2013).

[282] M. Tia, B. Cunha de Miranda, S. Daly, F. Gaie-Levrel, G. A. Garcia *et al.*, VUV photodynamics and chiral asymmetry in the photoionization of gas phase alanine enantiomers, J. Phys. Chem. A **118**, 2765 (2014).

[283] M. Yamashita and J. B. Fenn, Electrospray ion source. another variation on the free-jet theme, J. Phys. Chem. **88**, 4451 (1984).

[284] J. B. Fenn, M. Mann, C. K. Meng, S. F. Wong, and C. M. Whitehouse, Electrospray ionization for mass spectrometry of large biomolecules, Science **246**, 64 (1989).

[285] H. Awad and A. El-Aneed, Enantioselectivity of mass spectrometry: Challenges and promises, Mass Spectrom. Rev. **32**, 466 (2013).

[286] L. Wu and F. G. Vogt, A review of recent advances in mass spectrometric methods for gas-phase chiral analysis of pharmaceutical and biological compounds, J. Pharm. Biomed. Anal. **69**, 133 (2012).

[287] S. Daly, F. Rosu, and V. Gabelica, Mass-resolved electronic circular dichroism ion spectroscopy, Science **368**, 1465 (2020).

[288] P. Krüger and K.-M. Weitzel, Photoelectron circular dichroism in the photodetachment of amino acid anions, Angew. Chem., Int. Ed. **60**, 17861 (2021).

[289] L. Nahon, L. Nag, G. A. Garcia, I. Myrgorodska, U. Meierhenrich *et al.*, Determination of accurate electron chiral asymmetries in fenchone and camphor in the VUV range: Sensitivity to isomerism and enantiomeric purity, Phys. Chem. Chem. Phys. **18**, 12696 (2016).

[290] A. H. N. C. De Silva, D. Atri-Schuller, S. Dubey, B. P. Acharya, K. L. Romans *et al.*, Using circular dichroism to control energy transfer in multiphoton ionization, Phys. Rev. Lett. **126**, 023201 (2021).

[291] B. P. Acharya, M. Dodson, S. Dubey, K. L. Romans, A. H. N. C. De Silva *et al.*, Magnetic dichroism in few-photon ionization of polarized atoms, Phys. Rev. A **104**, 053103 (2021).

[292] B. P. Acharya, S. Dubey, K. L. Romans, A. H. N. C. De Silva, K. Foster, O. Russ, K. Bartschat, N. Douguet, and D. Fischer, Two-path interference in resonance-enhanced few-photon ionization of Li atoms, Phys. Rev. A **106**, 023113 (2022).

[293] S. Meister, A. Bondy, K. Schnorr, S. Augustin, H. Lindenblatt *et al.*, Photoelectron spectroscopy of laser-dressed atomic helium, Phys. Rev. A **102**, 062809 (2020).

[294] K. Prince, E. Allaria, C. Callegari, R. Cucini, G. De Ninno *et al.*, Coherent control with a short-wavelength free-electron laser, Nat. Photon. **10**, 176 (2016).

[295] D. Bharti, H. Srinivas, F. Shobeiry, K. R. Hamilton, R. Moshammer, T. Pfeifer, K. Bartschat, and A. Harth, Multisideband interference structures observed via high-order photon-induced continuum-continuum transitions in argon, Phys. Rev. A **107**, 022801 (2023).

[296] U. Fano, Effects of configuration interaction on intensities and phase shifts, Phys. Rev. **124**, 1866 (1961).

[297] M. Wickenhauser, J. Burgdörfer, F. Krausz, and M. Drescher, Time-resolved Fano resonances, Phys. Rev. Lett. **94**, 023002 (2005).

[298] A. Kaldun, A. Blättermann, V. Stooß, S. Donsa, H. Wei, R. Pazourek, S. Nagele, C. Ott, C.-D. Lin, J. Burgdörfer *et al.*, Observing the ultrafast buildup of a Fano resonance in the time domain, Science **354**, 738 (2016).

[299] A. C. Brown, G. S. J. Armstrong, J. Benda, D. D. A. Clarke, J. Wragg, K. R. Hamilton *et al.*, RMT: R-matrix with time-dependence. Solving the semi-relativistic, time-dependent Schrödinger equation for general, multielectron atoms and molecules in intense, ultrashort, arbitrarily polarized laser pulses, Comput. Phys. Commun. **250**, 107062 (2020).

[300] A. K. Kazansky and N. M. Kabachnik, Theoretical description of atomic photoionization by an attosecond XUV pulse in a strong laser field: Effects of rescattering and orbital polarization, J. Phys. B: At. Mol. Opt. Phys. **40**, 2163 (2007).

[301] N. Douguet, A. N. Grum-Grzhimailo, E. V. Gryzlova, E. I. Staroselskaya, J. Venzke, and K. Bartschat, Photoelectron angular distributions in bichromatic atomic ionization induced by circularly polarized VUV femtosecond pulses, Phys. Rev. A **93**, 033402 (2016).

[302] S.-K. Son, L. Young, and R. Santra, Impact of hollow-atom formation on coherent x-ray scattering at high intensity, Phys. Rev. A **83**, 033402 (2011).

[303] H. Fukuzawa, S.-K. Son, K. Motomura, S. Mondal, K. Nagaya *et al.*, Deep inner-shell multiphoton ionization by intense x-ray free-electron laser pulses, Phys. Rev. Lett. **110**, 173005 (2013).

[304] B. F. Murphy, T. Osipov, Z. Jurek, L. Fang, S.-K. Son *et al.*, Femtosecond x-ray-induced explosion of C60 at extreme intensity, Nat. Commun. **5**, 4281 (2014).

[305] Y. Hao, L. Inhester, S.-K. Son, and R. Santra, Theoretical evidence for the sensitivity of charge-rearrangement-enhanced x-ray ionization to molecular size, Phys. Rev. A **100**, 013402 (2019).

[306] L. Inhester, K. Hanasaki, Y. Hao, S.-K. Son, and R. Santra, x-ray multiphoton ionization dynamics of a water molecule irradiated by an x-ray free-electron laser pulse, Phys. Rev. A **94**, 023422 (2016).

[307] Y. Kumagai, Z. Jurek, W. Xu, H. Fukuzawa, K. Motomura *et al.*, Radiation-induced chemical dynamics in Ar clusters exposed to strong x-ray pulses, Phys. Rev. Lett. **120**, 223201 (2018).

[308] F. A. Gianturco, R. R. Lucchese, and N. Sanna, Calculation of low-energy elastic cross sections for electron-CF4 scattering, J. Chem. Phys. **100**, 6464 (1994).

[309] A. P. P. Natalense and R. R. Lucchese, Cross section and asymmetry parameter calculation for sulfur 1s photoionization of Sf_6, J. Chem. Phys. **111**, 5344 (1999).

[310] X. Gong, W. Jiang, J. Tong, J. Qiang, P. Lu, H. Ni, R. Lucchese, K. Ueda, and J. Wu, Asymmetric attosecond photoionization in molecular shape resonance, Phys. Rev. X **12**, 011002 (2022).

[311] M. Venuti, M. Stener, and P. Decleva, Valence photoionization of C6H6 by the B-spline one-centre expansion density functional method, Chem. Phys. **234**, 95 (1998).

[312] M. Stener and P. Decleva, Photoionization of first and second row hydrides by the B-spline one-centre expansion density functional method, J. Electron Spectrosc. Relat. Phenom. **94**, 195 (1998).

[313] M. Brosolo, P. Decleva, and A. Lisini, Continuum wavefunctions calculations with least-squares schemes in a B-splines basis, Comput. Phys. Commun. **71**, 207 (1992).

[314] M. Brosolo, P. Decleva, and A. Lisini, Lcao expansion in a spline basis for accurate variational determination of continuum wavefunctions. Applications to H_2^+ and HeH_2^+, Chem. Phys. **181**, 85 (1994).

[315] G. Fronzoni, M. Stener, P. Decleva, and G. De Alti, Theoretical study of the Cl 1s and 2p near edge photoabsorption spectra of HCl by accurate *ab initio* configuration interaction and density functional approaches, Chem. Phys. **232**, 9 (1998).

[316] M. Venuti, M. Stener, G. De Alti, and P. Decleva, Photoionization of C60 by large scale one-center density functional explicit continuum wave-function, J. Chem. Phys. **111**, 4589 (1999).

[317] P. Decleva, G. D. Alti, G. Fronzoni, and M. Stener, Theoretical study of resonances in the metal core photoionization of $M@C_{60}$ (M = Li, Na, K), J. Phys. B: At. Mol. Opt. Phys. **32**, 4523 (1999).

[318] M. Stener, G. Fronzoni, D. Toffoli, and P. Decleva, Time dependent density functional photoionization of CH4, NH3, H2O and HF, Chem. Phys. **282**, 337 (2002).

[319] D. Toffoli, M. Stener, G. Fronzoni, and P. Decleva, Convergence of the multicenter B-spline DFT approach for the continuum, Chem. Phys. **276**, 25 (2002).

[320] P. Decleva, M. Stener, and D. Toffoli, Continuum electronic states: The Tiresia code, Molecules **27**, 2026 (2022).

[321] M. Stener, G. Fronzoni, D. D. Tommaso, and P. Decleva, Density functional study on the circular dichroism of photoelectron angular distribution from chiral derivatives of oxirane, J. Chem. Phys. **120**, 3284 (2004).

[322] D. Toffoli and P. Decleva, Photoelectron angular distributions beyond the dipole approximation: A computational study on the N2 molecule, J. Phys. B: At. Mol. Opt. Phys. **39**, 2681 (2006).

[323] M. Stener, D. Toffoli, G. Fronzoni, and P. Decleva, Recent advances in molecular photoionization by density functional theory based approaches, Theor. Chem. Acc. **117**, 943 (2007).

[324] T. Moitra, A. Ponzi, H. Koch, S. Coriani, and P. Decleva, Accurate description of photoionization dynamical parameters, J. Phys. Chem. Lett. **11**, 5330 (2020).

[325] S. Petretti, Y. V. Vanne, A. Saenz, A. Castro, and P. Decleva, Alignment-dependent ionization of N_2, O_2, and CO_2 in intense laser fields, Phys. Rev. Lett. **104**, 223001 (2010).

[326] M. Awasthi, Y. V. Vanne, A. Saenz, A. Castro, and P. Decleva, Single-active-electron approximation for describing molecules in ultrashort laser pulses and its application to molecular hydrogen, Phys. Rev. A **77**, 063403 (2008).

[327] J. P. Farrell, S. Petretti, J. Förster, B. K. McFarland, L. S. Spector, Y. V. Vanne, P. Decleva, P. H. Bucksbaum, A. Saenz, and M. Guhr, Strong field ionization to multiple electronic states in water, Phys. Rev. Lett. **107**, 083001 (2011).

[328] O. Neufeld, D. Ayuso, P. Decleva, M. Y. Ivanov, O. Smirnova, and O. Cohen, Ultrasensitive chiral spectroscopy by dynamical symmetry breaking in high harmonic generation, Phys. Rev. X **9**, 031002 (2019).

[329] S. E. Canton, E. Plésiat, J. D. Bozek, B. S. Rude, P. Decleva *et al.*, Direct observation of Young's double-slit interferences in vibrationally resolved photoionization of diatomic molecules, Proc. Natl. Acad. Sci. USA **108**, 7302 (2011).

[330] E. Plésiat, L. Argenti, E. Kukk, C. Miron, K. Ueda, P. Decleva, and F. Martin, Intramolecular electron diffraction in vibrationally resolved *K*-shell photoionization of methane, Phys. Rev. A **85**, 023409 (2012).

[331] L. Argenti, T. D. Thomas, E. Plésiat, X.-J. Liu, C. Miron *et al.*, Double-slit experiment with a polyatomic molecule: Vibrationally resolved C1s photoelectron spectra of acetylene, New J. Phys. **14**, 033012 (2012).

[332] E. Kukk, D. Ayuso, T. D. Thomas, P. Decleva, M. Patanen *et al.*, Effects of molecular potential and geometry on atomic core-level photoemission over an extended energy range: The case study of the co molecule, Phys. Rev. A **88**, 033412 (2013).

[333] D. Ayuso, A. Palacios, P. Decleva, and F. Martín, Dissociative and non-dissociative photoionization of molecular fluorine from inner and valence shells, J. Electron Spectros. Relat. Phenomena **195**, 320 (2014).

[334] K. Ueda, C. Miron, E. Plésiat, L. Argenti, M. Patanen, K. Kooser *et al.*, Intramolecular photoelectron diffraction in the gas phase, J. Chem. Phys. **139**, 124306 (2013).

[335] M. Patanen, K. Kooser, L. Argenti, D. Ayuso, M. Kimura, S. Mondal, E. Plésiat, A. Palacios, K. Sakai, O. Travnikova, P. Decleva, E. Kukk, C. Miron, K. Ueda, and F. Martín, Vibrationally resolved C1s photoionization cross section of CF4, J. Phys. B: At. Mol. Opt. Phys. **47**, 124032 (2014).

[336] M. Lara-Astiaso, D. Ayuso, I. Tavernelli, P. Decleva, A. Palacios *et al.*, Faraday discussions decoherence, control and attosecond probing of XUV-induced charge migration in biomolecules. A theoretical outlook, Faraday Discuss. **194**, 41 (2016).

[337] D. Ayuso, A. Palacios, P. Decleva, and F. Martín, Ultrafast charge dynamics in glycine induced by attosecond pulses, Phys. Chem. Chem. Phys. **19**, 19767 (2017).

[338] M. Lara-Astiaso, A. Palacios, P. Decleva, I. Tavernelli, and F. Martín, Role of electron-nuclear coupled dynamics on charge migration induced by attosecond pulses in glycine, Chem. Phys. Lett. **683**, 357 (2017).

[339] N. Tancogne-Dejean, M. J. T. Oliveira, X. Andrade, H. Appel, C. H. Borca *et al.*, Octopus, a computational framework for exploring light-driven phenomena and quantum dynamics in extended and finite systems, J. Chem. Phys. **152**, 124119 (2020).

[340] X. Andrade, D. Strubbe, U. De Giovannini, A. H. Larsen, M. J. T. Oliveira *et al.*, Real-space grids and the octopus code as tools for the development of new simulation approaches for electronic systems, Phys. Chem. Chem. Phys. **17**, 31371 (2015).

[341] M. Marques and E. Gross, Time-dependent density functional theory, Annu. Rev. Phys. Chem. **55**, 427 (2004).

[342] U. De Giovannini, D. Varsano, M. A. L. Marques, H. Appel, E. K. U. Gross, and A. Rubio, *Ab initio* angle- and energy-resolved photoelectron spectroscopy with time-dependent density-functional theory, Phys. Rev. A **85**, 062515 (2012).

[343] X. Li, N. Govind, C. Isborn, A. E. DePrince, and K. Lopata, Real-time time-dependent electronic structure theory, Chem. Rev. **120**, 9951 (2020).

[344] K. A. Hamer, A. S. Folorunso, K. Lopata, K. J. Schafer, M. B. Gaarde, and F. Mauger, Tracking charge migration with frequency-matched strobo-spectroscopy, J. Phys. Chem. A **128**, 20 (2024).

[345] U. De Giovannini, G. Brunetto, A. Castro, J. Walkenhorst, and A. Rubio, Simulating pump–probe photoelectron and absorption spectroscopy on the attosecond timescale with time-dependent density functional theory, ChemPhysChem **14**, 1363 (2013).

[346] A. Crawford-Uranga, U. De Giovannini, E. Räsänen, M. J. T. Oliveira, D. J. Mowbray *et al.*, Time-dependent density-functional theory of strong-field ionization of atoms by soft x rays, Phys. Rev. A **90**, 033412 (2014).

[347] A. Crawford-Uranga, U. De Giovannini, D. J. Mowbray, S. Kurth, and A. Rubio, Modelling the effect of nuclear motion on the attosecond time-resolved photoelectron spectra of ethylene, J. Phys. B: At. Mol. Opt. Phys. **47**, 124018 (2014).

[348] S. A. Sato, H. Hübener, A. Rubio, and U. De Giovannini, First-principles simulations for attosecond photoelectron spectroscopy based on time-dependent density functional theory, Eur. Phys. J. B **91**, 126 (2018).

[349] A. Geyer, O. Neufeld, D. Trabert, U. De Giovannini, M. Hofmann, N. Anders, L. Sarkadi, M. S. Schöffler, L. P. H. Schmidt, A. Rubio, T. Jahnke, M. Kunitski, and S. Eckart, Quantum correlation of electron and ion energy in the dissociative strong-field ionization of H_2, Phys. Rev. Res. **5**, 013123 (2023).

[350] I. S. Wahyutama, D. D. Jayasinghe, F. Mauger, K. Lopata, M. B. Gaarde, and K. J. Schafer, All-electron, density-functional-based method for angle-resolved tunneling ionization in the adiabatic regime, Phys. Rev. A **106**, 052211 (2022).

[351] A. S. Folorunso, A. Bruner, F. Mauger, K. A. Hamer, S. Hernandez, R. R. Jones, L. F. DiMauro, M. B. Gaarde, K. J. Schafer, and K. Lopata, Molecular modes of attosecond charge migration, Phys. Rev. Lett. **126**, 133002 (2021).

[352] K. A. Hamer, F. Mauger, A. S. Folorunso, K. Lopata, R. R. Jones, L. F. DiMauro, K. J. Schafer, and M. B. Gaarde, Characterizing particle-like charge-migration dynamics with high-order harmonic sideband spectroscopy, Phys. Rev. A **106**, 013103 (2022).

[353] A. Prlj, B. F. E. Curchod, A. Fabrizio, L. Floryan, and C. Corminboeuf, Qualitatively incorrect features in the TDDFT spectrum of thiophene-based compounds, J. Phys. Chem. Lett. **6**, 13 (2015).

[354] M. Casida and M. Huix-Rotllant, Progress in time-dependent density-functional theory, Annu. Rev. Phys. Chem. **63**, 287 (2012).

[355] A. U. J. Lode, C. Lévêque, L. B. Madsen, A. I. Streltsov, and O. E. Alon, Colloquium: Multiconfigurational time-dependent Hartree approaches for indistinguishable particles, Rev. Mod. Phys. **92**, 011001 (2020).

[356] D. J. Haxton, K. V. Lawler, and C. W. McCurdy, Multiconfiguration time-dependent Hartree-Fock treatment of electronic and nuclear dynamics in diatomic molecules, Phys. Rev. A **83**, 063416 (2011).

[357] R. Sawada, T. Sato, and K. L. Ishikawa, Implementation of the multiconfiguration time-dependent Hatree-Fock method for general molecules on a multiresolution Cartesian grid, Phys. Rev. A **93**, 023434 (2016).

[358] C.-T. Liao, X. Li, D. J. Haxton, T. N. Rescigno, R. R. Lucchese, C. W. McCurdy, and A. Sandhu, Probing autoionizing states of molecular oxygen with XUV transient absorption: Electronic-symmetry-dependent line shapes and laser-induced modifications, Phys. Rev. A **95**, 043427 (2017).

[359] D. J. Haxton and C. W. McCurdy, Ultrafast population transfer to excited valence levels of a molecule driven by x-ray pulses, Phys. Rev. A **90**, 053426 (2014).

[360] D. J. Haxton, K. V. Lawler, and C. W. McCurdy, Qualitative failure of a multiconfiguration method in prolate spheroidal coordinates in calculating dissociative photoionization of H_2^+, Phys. Rev. A **91**, 062502 (2015).

[361] D. J. Haxton and C. W. McCurdy, Two methods for restricted configuration spaces within the multiconfiguration time-dependent Hartree-Fock method, Phys. Rev. A **91**, 012509 (2015).

[362] H. Miyagi and L. B. Madsen, Time-dependent restricted-active-space self-consistent-field theory for laser-driven many-electron dynamics, Phys. Rev. A **87**, 062511 (2013).

[363] J. J. Omiste and L. B. Madsen, Photoionization of aligned excited states in neon by attosecond laser pulses, J. Phys. B: At. Mol. Opt. Phys. **54**, 054001 (2021).

[364] H. Miyagi and L. Bojer Madsen, Time-dependent restricted-active-space self-consistent-field singles method for many-electron dynamics, J. Chem. Phys. **140**, 164309 (2014).

[365] H. Miyagi and L. B. Madsen, Time-dependent restricted-active-space self-consistent-field theory for laser-driven many-electron dynamics. II. Extended formulation and numerical analysis, Phys. Rev. A **89**, 063416 (2014).

[366] H. Miyagi and L. B. Madsen, Time-dependent restricted-active-space self-consistent-field theory with space partition, Phys. Rev. A **95**, 023415 (2017).

[367] S. Bauch, L. K. Sørensen, and L. B. Madsen, Time-dependent generalized-active-space configuration-interaction approach to photoionization dynamics of atoms and molecules, Phys. Rev. A **90**, 062508 (2014).

[368] S. Chattopadhyay, S. Bauch, and L. B. Madsen, Electron-correlation effects in enhanced ionization of molecules: A time-dependent generalized-active-space configuration-interaction study, Phys. Rev. A **92**, 063423 (2015).

[369] T. Sato and K. L. Ishikawa, Time-dependent complete-active-space self-consistent-field method for multielectron dynamics in intense laser fields, Phys. Rev. A **88**, 023402 (2013).

[370] T. Sato, K. L. Ishikawa, I. Březinová, F. Lackner, S. Nagele *et al.*, Time-dependent complete-active-space self-consistent-field method for atoms: Application to high-order harmonic generation, Phys. Rev. A **94**, 023405 (2016).

[371] S. Sato, H. Hübener, U. De Giovannini, and A. Rubio, *Ab initio* simulation of attosecond transient absorption spectroscopy in two-dimensional materials, Appl. Sci. **8**, 1777 (2018).

[372] Y. Li, T. Sato, and K. L. Ishikawa, Implementation of a time-dependent multiconfiguration self-consistent-field method for coupled electron-nuclear dynamics in diatomic molecules driven by intense laser pulses, Phys. Rev. A **104**, 043104 (2021).

[373] T. Sato, H. Pathak, Y. Orimo, and K. L. Ishikawa, Communication: Time-dependent optimized coupled-cluster method for multielectron dynamics, J. Chem. Phys. **148**, 051101 (2018).

[374] H. Pathak, T. Sato, and K. L. Ishikawa, Time-dependent optimized coupled-cluster method for multielectron dynamics. II. A coupled electron-pair approximation, J. Chem. Phys. **152**, 124115 (2020).

[375] H. Pathak, T. Sato, and K. L. Ishikawa, Time-dependent optimized coupled-cluster method for multielectron dynamics. III. A second-order many-body perturbation approximation, J. Chem. Phys. **153**, 034110 (2020).

[376] H. Pathak, T. Sato, and K. L. Ishikawa, Time-dependent optimized coupled-cluster method for multielectron dynamics. IV. Approximate consideration of the triple excitation amplitudes, J. Chem. Phys. **154**, 234104 (2021).

[377] T. Sato, H. Pathak, Y. Orimo, and K. L. Ishikawa, Time-dependent multiconfiguration self-consistent-field and time-dependent optimized coupled-cluster methods for intense laser-driven multielectron dynamics, Can. J. Chem. **101**, 698 (2023).

[378] D. Toffoli and P. Decleva, A multichannel least-squares B-spline approach to molecular photoionization: Theory, implementation, and applications within the configuration-interaction singles approximation, J. Chem. Theory Comput. **12**, 4996 (2016).

[379] P. Hoerner, W. Li, and H. B. Schlegel, Angular dependence of strong field ionization of 2-phenylethyl-N,N-dimethylamine (PENNA) using time-dependent configuration interaction with an absorbing potential, J. Phys. Chem. A **124**, 4777 (2020).

[380] S. Carlström, M. Spanner, and S. Patchkovskii, General time-dependent configuration-interaction singles. I. Molecular case, Phys. Rev. A **106**, 043104 (2022).

[381] S. Carlström, M. Bertolino, J. M. Dahlström, and S. Patchkovskii, General time-dependent configuration-interaction singles. II. Atomic case, Phys. Rev. A **106**, 042806 (2022).

[382] H. Bachau, E. Cormier, P. Decleva, J. E. Hansen, and F. Martín, Applications of B-splines in atomic and molecular physics, Rep. Prog. Phys. **64**, 1815 (2001).

[383] F. L. Yip, C. W. McCurdy, and T. N. Rescigno, Hybrid gaussian–discrete-variable representation approach to molecular continuum processes: Application to photoionization of diatomic li_2^+, Phys. Rev. A **78**, 023405 (2008).

[384] L. Greenman, R. R. Lucchese, and C. W. McCurdy, Variational treatment of electron-polyatomic-molecule scattering calculations using adaptive overset grids, Phys. Rev. A **96**, 052706 (2017).

[385] P. G. Burke, *R-Matrix Theory of Atomic Collisions*, *Vol. 61 of Springer Series on Atomic, Optical, and Plasma Physics*, 1st ed. (Springer, Berlin, 2011).

[386] K. A. Berrington, W. B. Eissner, and P. H. Norrington, RMATRX1: Belfast atomic R-matrix codes, Comput. Phys. Commun. **92**, 290 (1995).

[387] N. Badnell, UK APAP R-matrix codes, https://amdpp.phys.strath.ac.uk/UK_RmaX/Rmatrix.html.

[388] A. Brown, R-matrix II, https://gitlab.com/Uk-amor/RMT/rmatrixII.

[389] J. D. Gorfinkiel and J. Tennyson, Electron impact ionization of small molecules at intermediate energies: The molecular R-matrix with pseudostates method, J. Phys. B: At. Mol. Opt. Phys. **38**, 1607 (2005).

[390] J. M. Carr, P. G. Galiatsatos, J. D. Gorfinkiel, A. G. Harvey, M. A. Lysaght *et al.*, UKRmol: A low-energy electron- and positron-molecule scattering suite, Eur. Phys. J. D **66**, 58 (2012).

[391] W. J. Brigg, J. Tennyson, and M. Plummer, R-matrix calculations of low-energy electron collisions with methane, J. Phys. B: At. Mol. Opt. Phys. **47**, 185203 (2014).

[392] A. G. Harvey, D. S. Brambila, F. Morales, and O. Smirnova, An R-matrix approach to electron–photon–molecule collisions: Photoelectron angular distributions from aligned molecules, J. Phys. B: At. Mol. Opt. Phys. **47**, 215005 (2014).

[393] Z. Mašín, J. Benda, J. D. Gorfinkiel, A. G. Harvey, and J. Tennyson, UKRmol+: A suite for modelling electronic processes in molecules interacting with electrons, positrons and photons using the R-matrix method, Comput. Phys. Commun. **249**, 107092 (2020).

[394] D. S. Brambila, A. G. Harvey, Z. Masin, J. D. Gorfinkiel, and O. Smirnova, The role of multichannel effects in the photoionization of the NO_2 molecule: An *ab initio R*-matrix study, J. Phys. B: At. Mol. Opt. Phys. **48**, 245101 (2015).

[395] B. D. Bruner, Z. Mašín, M. Negro, F. Morales, D. Brambila *et al.*, Multidimensional high harmonic spectroscopy of polyatomic molecules: Detecting sub-cycle laser-driven hole dynamics upon ionization in strong mid-IR laser fields, Faraday Discuss. **194**, 369 (2016).

[396] D. S. Brambila, A. G. Harvey, K. Houfek, Z. Masin, and O. Smirnova, Role of electronic correlations in photoionization of NO2 in the vicinity of the 2A1/2B2 conical intersection, Phys. Chem. Chem. Phys. **19**, 19673 (2017).

[397] J. Benda, J. D. Gorfinkiel, Z. Mašín, G. S. J. Armstrong, A. C. Brown, D. D. A. Clarke, H. W. van der Hart, and J. Wragg, Perturbative and nonperturbative photoionization of H_2 and H_2O using the molecular R-matrix-with-time method, Phys. Rev. A **102**, 052826 (2020).

[398] O. Zatsarinny, BSR: B-spline atomic R-matrix codes, Comput. Phys. Commun. **174**, 273 (2006).

[399] O. Zatsarinny and K. Bartschat, The B-spline R-matrix method for atomic processes: Application to atomic structure, electron collisions and photoionization, J. Phys. B: At. Mol. Opt. Phys. **46**, 112001 (2013).

[400] B. I. Schneider and T. N. Rescigno, Complex Kohn variational method: Application to low-energy electron-molecule collisions, Phys. Rev. A **37**, 3749 (1988).

[401] C. W. McCurdy and T. N. Rescigno, Collisions of electrons with polyatomic molecules: Electron-methane scattering by the complex Kohn variational method, Phys. Rev. A **39**, 4487 (1989).

[402] B. I. Schneider, T. N. Rescigno, and C. W. McCurdy, Resonant vibrational excitation of H_2Co by low-energy electron impact, Phys. Rev. A **42**, 3132 (1990).

[403] T. N. Rescigno, B. H. Lengsfield, and A. E. Orel, Interchannel coupling and ground state correlation effects in the photoionization of co, J. Chem. Phys. **99**, 5097 (1993).

[404] J. B. Williams, C. S. Trevisan, M. S. Schöffler, T. Jahnke, I. Bocharova *et al.*, Imaging polyatomic molecules in three dimensions using molecular frame photoelectron angular distributions, Phys. Rev. Lett. **108**, 233002 (2012).

[405] C.-Y. Lin, C. W. McCurdy, and T. N. Rescigno, Complex Kohn approach to molecular ionization by high-energy electrons: Application to H2O, Phys. Rev. A **89**, 012703 (2014).

[406] C. W. McCurdy, T. N. Rescigno, C. S. Trevisan, R. R. Lucchese, B. Gaire *et al.*, Unambiguous observation of F-atom

core-hole localization in CF_4 through body-frame photoelectron angular distributions, Phys. Rev. A **95**, 011401(R) (2017).

[407] N. Douguet, B. I. Schneider, and L. Argenti, Application of the complex Kohn variational method to attosecond spectroscopy, Phys. Rev. A **98**, 023403 (2018).

[408] V. P. Majety and A. Scrinzi, Static field ionization rates for multi-electron atoms and small molecules, J. Phys. B: At. Mol. Opt. Phys. **48**, 245603 (2015).

[409] A. Scrinzi, TRECX—An environment for solving time-dependent Schrödinger-like problems, Comput. Phys. Commun. **270**, 108146 (2022).

[410] V. P. Majety, A. Zielinski, and A. Scrinzi, Photoionization of few electron systems: A hybrid coupled channels approach, New J. Phys. **17**, 063002 (2015).

[411] V. P. Majety and A. Scrinzi, Multielectron effects in strong-field ionization of CO2: Impact on differential photoelectron spectra, Phys. Rev. A **96**, 053421 (2017).

[412] C. Marante, M. Klinker, T. Kjellsson, E. Lindroth, J. González-Vázquez, L. Argenti, and F. Martin, Photoionization using the XCHEM approach: Total and partial cross sections of ne and resonance parameters above the $2s^2 2p^5$ threshold, Phys. Rev. A **96**, 022507 (2017).

[413] C. Marante, M. Klinker, I. Corral, J. González-Vázquez, L. Argenti *et al.*, Hybrid-basis close-coupling interface to quantum chemistry packages for the treatment of ionization problems, J. Chem. Theory Comput. **13**, 499 (2017).

[414] M. Klinker, C. Marante, L. Argenti, J. González-Vázquez, and F. Martín, Electron correlation in the ionization continuum of molecules: Photoionization of N_2 in the vicinity of the hopfield series of autoionizing states, J. Phys. Chem. Lett. **9**, 756 (2018).

[415] M. Klinker, C. Marante, L. Argenti, J. González-Vázquez, and F. Martín, Partial cross sections and interfering resonances in photoionization of molecular nitrogen, Phys. Rev. A **98**, 033413 (2018).

[416] S. Marggi Poullain, M. Klinker, J. González-Vázquez, and F. Martín, Resonant photoionization of O_2 up to the fourth ionization threshold, Phys. Chem. Chem. Phys. **21**, 16497 (2019).

[417] V. J. Borràs, J. González-Vázquez, L. Argenti, and F. Martín, Molecular-frame photoelectron angular distributions of CO in the vicinity of Feshbach resonances: An XCHEM approach, J. Chem. Theory Comput. **17**, 6330 (2021).

[418] V. J. Borràs, J. González-Vázquez, L. Argenti, and F. Martín, Attosecond photoionization delays in the vicinity of molecular feshbach resonances, Sci. Adv. **9**, eade3855 (2023).

[419] M. Ruberti, P. Decleva, and V. Averbukh, Full *ab initio* many-electron simulation of attosecond molecular pump–probe spectroscopy, J. Chem. Theory Comput. **14**, 4991 (2018).

[420] M. Ruberti, Restricted correlation space B-spline ADC approach to molecular ionization: Theory and applications to total photoionization cross-sections, J. Chem. Theory Comput. **15**, 3635 (2019).

[421] M. Ruberti, Onset of ionic coherence and ultrafast charge dynamics in attosecond molecular ionisation, Phys. Chem. Chem. Phys. **21**, 17584 (2019).

[422] M. Ruberti, P. Decleva, and V. Averbukh, Multi-channel dynamics in high harmonic generation of aligned CO_2: *Ab initio* analysis with time-dependent B-spline algebraic diagrammatic construction, Phys. Chem. Chem. Phys. **20**, 8311 (2018).

[423] M. Ruberti, Quantum electronic coherences by attosecond transient absorption spectroscopy: *Ab initio* B-spline RCS-ADC study, Faraday Discuss. **228**, 286 (2021).

[424] M. Ruberti, S. Patchkovskii, and V. Averbukh, Quantum coherence in molecular photoionization, Phys. Chem. Chem. Phys. **24**, 19673 (2022).

[425] G. Bandarage and R. R. Lucchese, Multiconfiguration multichannel Schwinger study of the C(1*s*) photoionization of CO including shake-up satellites, Phys. Rev. A **47**, 1989 (1993).

[426] R. E. Stratmann and R. R. Lucchese, A graphical unitary group approach to study multiplet specific multichannel electron correlation effects in the photoionization of O_2, J. Chem. Phys. **102**, 8493 (1995).

[427] R. R. Lucchese, J. Söderström, T. Tanaka, M. Hoshino, M. Kitajima *et al.*, Vibrationally resolved partial cross sections and asymmetry parameters for nitrogen *K*-shell photoionization of the N_2O molecule, Phys. Rev. A **76**, 012506 (2007).

[428] C. Jin, A.-T. Le, S.-F. Zhao, R. R. Lucchese, and C. D. Lin, Theoretical study of photoelectron angular distributions in single-photon ionization of aligned N_2 and CO_2, Phys. Rev. A **81**, 033421 (2010).

[429] J. M. Randazzo, C. Marante, S. Chattopadhyay, B. I. Schneider, J. Olsen, and L. Argenti, ASTRA: Transition-density-matrix approach to molecular ionization, Phys. Rev. Res. **5**, 043115 (2023).

[430] J. Olsen, LUCIA, a general CI code written by J. Olsen, University of Aarhus with contributions from H. Larsen and M. Fülscher (2000).

[431] J. R. Rouxel and S. Mukamel, Molecular chirality and its monitoring by ultrafast x-ray pulses, Chem. Rev. **122**, 16802 (2022).

[432] D. Baykusheva, D. Zindel, V. Svoboda, E. Bommeli, M. Ochsner, A. Tehlar, and H. Jakob Wörner, Real-time probing of chirality during a chemical reaction, Proc. Natl. Acad. Sci. USA **116**, 23923 (2019).

[433] V. Svoboda, N. B. Ram, D. Baykusheva, D. Zindel, M. D. Waters *et al.*, Femtosecond photoelectron circular dichroism of chemical reactions, Sci. Adv. **8**, eabq2811 (2022).

[434] R. Mincigrucci, J. Rouxel, B. Rossi, E. Principi, C. Bottari *et al.*, Element-and enantiomer-selective visualization of molecular motion in real-time, Nat. Commun. **14**, 386 (2023).

[435] D. C. Ashley and E. Jakubikova, Ray-Dutt and Bailar twists in Fe(II)-Tris (2,2′-bipyridine): Spin states, sterics, and Fe-N bond strengths, Inorg. Chem. **57**, 5585 (2018).

[436] L. Alagna, T. Prosperi, S. Turchini, J. Goulon, A. Rogalev, C. Goulon-Ginet, C. R. Natoli, R. D. Peacock, and B. Stewart *et al.*, x-ray natural circular dichroism, Phys. Rev. Lett. **80**, 4799 (1998).

[437] J. Goulon, C. Goulon-Ginet, A. Rogalev, G. Benayoun, C. Brouder *et al.*, x-ray natural circular dichroism and chiral-EXAFS in gyrotropic crystals, J. Synchrotron Radiat. **7**, 182 (2000).

[438] S. Turchini, N. Zema, S. Zennaro, L. Alagna, B. Stewart *et al.*, Core electron transitions as a probe for molecular chirality: Natural circular dichroism at the carbon k-edge of methyloxirane, J. Am. Chem. Soc. **126**, 4532 (2004).

[439] J. R. Rouxel, Y. Zhang, and S. Mukamel, x-ray Raman optical activity of chiral molecules, Chem. Sci. **10**, 898 (2019).

[440] T. D. Crawford, M. C. Tam, and M. L. Abrams, The current state of *ab initio* calculations of optical rotation and elec-

tronic circular dichroism spectra, J. Phys. Chem. A **111**, 12057 (2007).
[441] J. Jusélius, D. Sundholm, and J. Gauss, Calculation of current densities using gauge-including atomic orbitals, J. Chem. Phys. **121**, 3952 (2004).
[442] A. Jiemchooroj, U. Ekström, and P. Norman, Near-edge x-ray absorption and natural circular dichroism spectra of l-alanine: A theoretical study based on the complex polarization propagator approach, J. Chem. Phys. **127**, 165104 (2007).
[443] V. Y. Chernyak, P. Saurabh, and S. Mukamel, Non-linear non-local molecular electrodynamics with nano-optical fields, J. Chem. Phys. **143**, 164107 (2015).
[444] D. P. Craig and T. Thirunamachandran, *Molecular Quantum Electrodynamics: An Introduction to Radiation-Molecule Interactions* (Courier Corporation, North Chelmsford, MA, 1998).
[445] S. Mukamel, *Principles of Nonlinear Optical Spectroscopy*, Oxford Series in Optical and Imaging Sciences (Oxford University Press, Oxford, UK, 1995).
[446] K. A. Forbes, D. Green, and G. A. Jones, Relevance of longitudinal fields of paraxial optical vortices, J. Opt. **23**, 075401 (2021).
[447] J. R. Rouxel, B. Rösner, D. Karpov, C. Bacellar, G. F. Mancini, F. Zinna, D. Kinschel, O. Cannelli, M. Oppermann, C. Svetina *et al.*, Hard x-ray helical dichroism of disordered molecular media, Nat. Photon. **16**, 570 (2022).
[448] X. Jiang, Y. Nam, J. R. Rouxel, H. Yong, and S. Mukamel, Time-resolved enantiomer-exchange probed by using the orbital angular momentum of x-ray light, Chem. Sci. **14**, 11067 (2023).
[449] R. M. Parrish and T. J. Martínez, *Ab initio* computation of rotationally-averaged pump–probe x-ray and electron diffraction signals, J. Chem. Theory Comput. **15**, 1523 (2019).
[450] V. M. Freixas, J. R. Rouxel, Y. Nam, S. Tretiak, N. Govind, and S. Mukamel, x-ray and optical circular dichroism as local and global ultrafast chiral probes of [12] helicene racemization, J. Am. Chem. Soc. **145**, 21012 (2023).
[451] N. Ji, V. Ostroverkhov, M. Belkin, Y.-J. Shiu, and Y.-R. Shen, Toward chiral sum-frequency spectroscopy, J. Am. Chem. Soc. **128**, 8845 (2006).
[452] M. Terazima, A transient grating detection method of circular dichroism, Mol. Phys. **88**, 1223 (1996).
[453] U. Hergenhahn, E. E. Rennie, O. Kugeler, S. Marburger, T. Lischke *et al.*, Photoelectron circular dichroism in core level ionization of randomly oriented pure enantiomers of the chiral molecule camphor, J. Chem. Phys. **120**, 4553 (2004).
[454] L. Nahon, G. A. Garcia, C. J. Harding, E. Mikajlo, and I. Powis, Determination of chiral asymmetries in the valence photoionization of camphor enantiomers by photoelectron imaging using tunable circularly polarized light, J. Chem. Phys. **125**, 114309 (2006).
[455] I. Powis, C. J. Harding, G. A. Garcia, and L. Nahon, A valence photoelectron imaging investigation of chiral asymmetry in the photoionization of fenchone and camphor, ChemPhysChem **9**, 475 (2008).
[456] G. Alberti, S. Turchini, G. Contini, N. Zema, T. Prosperi *et al.*, Dichroism in core-excited and core-ionized methyloxirane, Phys. Scr. **78**, 058120 (2008).
[457] D. Catone, M. Stener, P. Decleva, G. Contini, N. Zema, T. Prosperi, V. Feyer, K. C. Prince, and S. Turchini, Resonant circular dichroism of chiral metal-organic complex, Phys. Rev. Lett. **108**, 083001 (2012).
[458] M. Pitzer, G. Kastirke, M. Kunitski, T. Jahnke, T. Bauer *et al.*, Absolute configuration from different multifragmentation pathways in light-induced Coulomb explosion imaging, ChemPhysChem **17**, 2465 (2016).
[459] M. Pitzer, G. Kastirke, P. Burzynski, M. Weller, D. Metz *et al.*, Stereochemical configuration and selective excitation of the chiral molecule halothane, J. Phys. B: At. Mol. Opt. Phys. **49**, 234001 (2016).
[460] G. Nalin, K. Fehre, F. Trinter, N. M. Novikovskiy, N. Anders *et al.*, Photoelectron circular dichroism of o 1s-photoelectrons of uniaxially oriented trifluoromethyloxirane: Energy dependence and sensitivity to molecular configuration, Phys. Chem. Chem. Phys. **23**, 17248 (2021).
[461] K. Fehre, F. Trinter, N. M. Novikovskiy, S. Grundmann, D. Tsitsonis *et al.*, Influence of the emission site on the photoelectron circular dichroism in trifluoromethyloxirane, Phys. Chem. Chem. Phys. **24**, 13597 (2022).
[462] K. Fehre, G. Nalin, N. M. Novikovskiy, S. Grundmann, G. Kastirke *et al.*, A new route for enantio-sensitive structure determination by photoelectron scattering on molecules in the gas phase, Phys. Chem. Chem. Phys. **24**, 26458 (2022).
[463] G. Nalin, N. M. Novikovskiy, K. Fehre, N. Anders, D. Trabert *et al.*, Molecular-frame differential photoelectron circular dichroism of o 1s-photoelectrons of trifluoromethyloxirane, Phys. Rev. Res. **5**, 013021 (2023).
[464] H. Fukuzawa, R. R. Lucchese, X.-J. Liu, K. Sakai, H. Iwayama *et al.*, Probing molecular bond-length using molecular-frame photoelectron angular distributions, J. Chem. Phys. **150**, 174306 (2019).
[465] H. Fukuzawa, S. Yamada, Y. Sakakibara, T. Tachibana, Y. Ito *et al.*, Probing gaseous molecular structure by molecular-frame photoelectron angular distributions, J. Chem. Phys. **151**, 104302 (2019).
[466] R. L. Dubs, S. N. Dixit, and V. McKoy, Circular dichroism in photoelectron angular distributions from oriented linear molecules, Phys. Rev. Lett. **54**, 1249 (1985).
[467] T. Jahnke, T. Weber, A. L. Landers, A. Knapp, S. Schössler *et al.*, Circular dichroism in *K*-shell ionization from fixed-in-space CO and N_2 molecules, Phys. Rev. Lett. **88**, 073002 (2002).
[468] A. Pier, K. Fehre, S. Grundmann, I. Vela-Perez, N. Strenger *et al.*, Chiral photoelectron angular distributions from ionization of achiral atomic and molecular species, Phys. Rev. Res. **2**, 033209 (2020).
[469] P. V. Demekhin, A. Ehresmann, and V. L. Sukhorukov, Single center method: A computational tool for ionization and electronic excitation studies of molecules, J. Chem. Phys. **134**, 024113 (2011).
[470] S. A. Galitskiy, A. N. Artemyev, K. Jänkälä, B. M. Lagutin, and P. V. Demekhin, Hartree-fock calculation of the differential photoionization cross sections of small li clusters, J. Chem. Phys. **142**, 034306 (2015).
[471] N. M. Novikovskiy, A. N. Artemyev, D. V. Rezvan, B. M. Lagutin, and P. V. Demekhin, Multichannel single center method, J. Phys. B: At. Mol. Opt. Phys. **55**, 175001 (2022).